5-2011

An Investigation of Atmospheric Turbulence Probes with Ground Test Comparisons of Probe Head Designs and Evaluation of Suitability to Instrumented Aircraft

Charles F Lams
clams@utk.edu

To the Graduate Council:

I am submitting herewith a thesis written by Charles F Lams entitled "An Investigation of Atmospheric Turbulence Probes with Ground Test Comparisons of Probe Head Designs and Evaluation of Suitability to Instrumented Aircraft." I have examined the final electronic copy of this thesis for form and content and recommend that it be accepted in partial fulfillment of the requirements for the degree of Master of Science, with a major in Aviation Systems.

Stephen Corda, Major Professor

We have read this thesis and recommend its acceptance:

Peter Solies, John Muratore

Accepted for the Council:
Carolyn R. Hodges

Vice Provost and Dean of the Graduate School

(Original signatures are on file with official student records.)

An Investigation of Atmospheric Turbulence Probes with Ground Test Comparisons of Probe Head Designs and Evaluation of Suitability to Instrumented Aircraft

A Thesis Presented for

the Master of Science

Degree

The University of Tennessee, Knoxville

Charles F. Lams

May, 2011

ACKNOWLEDGMENTS

I would like to thank the members of the University of Tennessee Space Institute Aviation Systems Department for all their help with completing this thesis. Specifically, my major advisor, Professor Stephen Corda for his guidance and advice and Professor John Muratore for his extensive hours of work on the software programs used and general advice. I would also like to thank Mr. Joe Young and Mr. William Moonan for their assistance with the bench testing set up and Mr. Harry Whitver for help with designing and creating the hemispherical sensing heads used in testing.

ABSTRACT

A comparison of methods to determine the flow angle components of atmospheric velocity vectors is presented. The atmospheric turbulence probes used to measure behavior of the atmosphere use different methods to obtain this information and there is some confusion as to which method is best. Although the methods are all based upon potential flow theory, the details about how the atmospheric and flight parameters are measured makes a difference to the design of an atmospheric turbulence probe and carrier research aircraft. This paper presents the mathematical theory behind five methods of obtaining atmospheric flow angle measurements from a moving aircraft. One of these methods, the Flush Air Data Sensing system developed by NASA has not previously been used in this particular application before but is found to be as accurate as more commonly used methods that utilize a hemispherical sensing head. In fact, none of the methods presented show any statistical improvement in measuring flow angles. It is therefore suggested that the best method the one that considers the probe and aircraft as a whole system rather than preferring one method over another.

TABLE OF CONTENTS

Chapter 1: Introduction to Atmospheric Turbulence Probes 1

1.1 Atmospheric Turbulence Probes Overview 1

1.2 Goals of the Present Research 5

1.3 Uses of an Atmospheric Turbulence Probe 5

1.4 The Relationship Between Atmospheric Velocity Components 8

1.5 Development of Flow Velocity Measurement 11

1.6 Development of Probe Velocity Measurement 16

1.7 Development of Atmospheric Motion Velocity Measurement 18

Chapter 2: Measurement Theory 19

2.1 Overview 19

2.2 True Airspeed Measurement 22

2.3 Flow Angle Measurement 23

2.4 High Resolution Model 27

2.5 Low Resolution Model 32

2.6 NCAR Model 36

2.7 Ekman Model 39

2.8 Dynamic Pressure and Static Pressure Measurement 44

2.9 Flush Airdata Sensing 47

Chapter 3: Bench Test of Probe Heads 50

3.1 Bench Test Overview 50

3.2 Equipment 50

3.3 Pressure Transducer Reference Calibration 55

3.4 Probe Head Test 56

Chapter 4: Results and Discussion 58

4.1 Calculated vs. Measured Pressures 58

4.2 Variability of FADS Port Combinations 70

4.3 Comparison of R^2 Values 72

Chapter 5: Conclusions 77

List of References 81

Appendix A: Details for Calculations of Velocity Components 84

Appendix B: Detail of Bench Test Results 108

Vita 162

LIST OF FIGURES

Figure 1. A BAT probe mounted on a LongEZ aircraft [1]. 2

Figure 2. The interior of a BAT probe [2]. 3

Figure 3. Flush Air Data Sensing system [23]. 14

Figure 4. Hemispherical probe head with cruciform arrangement of pressure port locations. 20

Figure 5. Hemispherical probe head with FADS arrangement of pressure port locations. 21

Figure 6. Side view of hemispherical sensing head with cone angles shown. 49

Figure 7. Bench test set up, showing probe head, wind generator and PXI device. 51

Figure 8. Interior of wind generator, showing settling chamber and fan. 53

Figure 9. Close up of a probe head and connected pressure lines, mounted on tripod. 54

Figure 10. Calculated Angle of Attack vs. Measured Angle of Attack, 45° Head. 60

Figure 11. Calculated Angle of Sideslip vs. Measured Angle of Sideslip, 45° Head. 62

Figure 12. Calculated Angle of Attack vs. Measured Angle of Attack, 41.8° Head. 64

Figure 13. Calculated Angle of Sideslip vs. Measured Angle of Sideslip, 41.8° Head. 65

Figure 14. Calculated Angle of Attack vs. Measured Angle of Attack, FADS Head. 67

Figure 15. Calculated angle of sideslip vs. measured angle of sideslip, FADS head. 69

Figure 16. Calculated angle of attack vs. measured angle of attack, FADS head, all ‘triples.’ 71

NOMENCLATURE

BAT	Best Air Turbulence
D	unit vector normalizing factor
FADS	flush airdata sensing
FPM	FADS pressure model
gps	global positioning system
k	pressure port number
n	number of ports
N	unit vector
NASA	National Aeronautics and Space Administration
NCAR	National Center for Atmospheric Research
NOAA	National Oceanographic and Atmospheric Administration
p	pressure
p_∞	free-stream static pressure
p_0	stagnation point pressure
p_k	pressure at port k
p_s	static pressure

p_t	total pressure
q	dynamic pressure
q_c	impact pressure
q_∞	free-stream dynamic pressure
R	ideal gas constant
T	temperature
U	airspeed
V	velocity
α	angle of attack
α_e	effective, or local, angle of attack
β	angle of sideslip
β_e	effective, or local, angle of sideslip
Γ	pressure difference, eg. $\Gamma_{ij} = p_i - p_j$
$\delta\alpha$	angle of attack flow correction angle
$\delta\beta$	angle of sideslip flow correction angle
ε	shape and compressibility parameter
θ	local flow incidence angle

λ	cone angle of a pressure port
ρ	density
ϕ	clock angle of a pressure port

CHAPTER 1: INTRODUCTION TO ATMOSPHERIC TURBULENCE PROBES

1.1 Atmospheric Turbulence Probes Overview

Atmospheric turbulence probes are sensor packages that are designed to extract the individual components of velocity of the atmosphere through which the probe is travelling. An atmospheric turbulence probe commonly uses an amalgamation of an air data probe, an inertial measurement system, a global positioning system and software and hardware to link these three major parts together to achieve this end. Figure 1 shows an example of a successful atmospheric turbulence probe, called the 'Best Air Turbulence' (BAT) probe, mounted on the nose of a LongEZ aircraft [1]. Figure 2 is a graphic showing the interior of a BAT probe and the hardware used [2]. Atmospheric turbulence probes may be self contained instrumentation and data processing packages that are 'generic' and capable of mounting on any suitable research aircraft or they may be specific to a particular probe-airframe combination. Applications to balloons, helicopters, unmanned aerial vehicles and sea based vessels are also possible.

With a wide array of platforms that can carry a turbulence probe, the specific set up of one particular airframe-probe combination may vary widely from that of another. There are several in-flight and ground tests which should be performed in order to ascertain that the data from one particular set up is both accurate and interchangeable with similar testing using a slightly different set up. Wind tunnel and in-flight calibrations of the turbulence measurement system should be performed. As an example, the in-flight static pressure position error correction test is particularly significant to achieving results which are accurate. This test measures the error in static pressure at the measurement location chosen for the turbulence

Figure 1. A BAT probe mounted on a LongEZ aircraft [1].

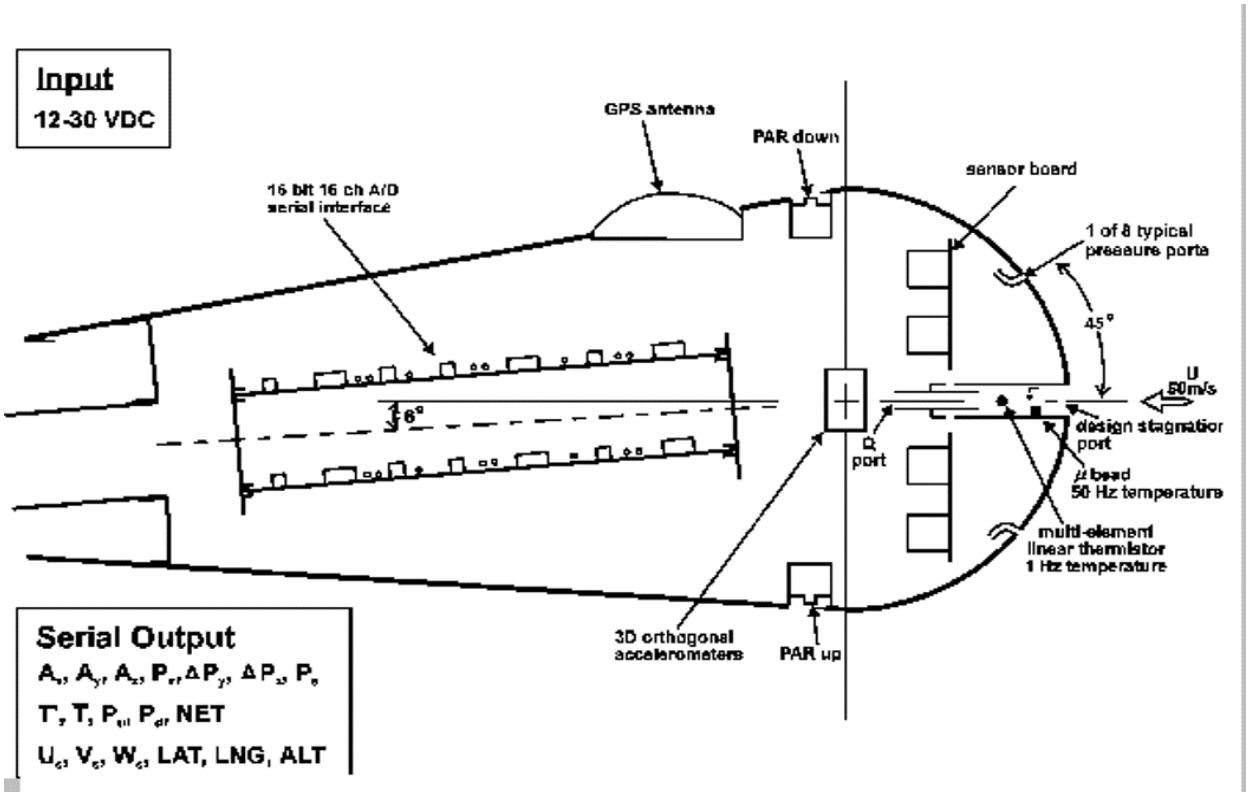

Figure 2. The interior of a BAT probe [2].

probe. The measured static pressure is affected by the changing flow field around the aircraft body in flight. By performing an in-flight calibration of the static pressure measurement this static pressure position error may be calculated out of the final static pressure measurement. Similarly, the probe itself must be tested in a wind tunnel to determine any measurement errors caused by design or manufacturing problems.

With a varied array of uses for the data from an atmospheric turbulence probe, it is vital that a turbulence measurement probe be capable of accurately and consistently producing information on the atmosphere through which it is travelling. To achieve this end the probe and research platform must be examined as an integrated system. Even a generic turbulence measurement probe requires calibration of sensors to probe location on the aircraft and flight characteristics of the airframe. Some aircraft are capable of providing information on the airflow relative to the probe, such as static pressures, dynamic pressures, and temperature. Information on the probe movement may be available from systems on the airframe such as GPS, magnetic heading or true airspeed. Other airframe-probe combinations may work best with a probe that is capable of performing all the necessary measurements within the probe unit.

The mathematical models used to extract the velocity components from the atmosphere are all based upon the same potential flow theory, as described below, but there are some significant differences in application. The airframe-probe combination may work better with some methods than with others and other factors such as cost and availability of components will affect the method chosen for each application. Comparisons between the different measurement techniques and their applicability to various airframe and probe combinations are a major focus of this thesis.

1.2 Goals of the Present Research

The ultimate goal of the present research is to provide a useful reference guide for designing an atmospheric turbulence probe. To achieve this end, current methods for determining flow angles are discussed, comparing their strengths and weaknesses. Methods developed for acquiring air data information from a hemispherical sensing head have been developed by NOAA, NCAR and NASA. There is some confusion regarding which of these methods is most appropriate for use, and even if one method is indeed most appropriate. By defining the methods clearly and applying them in bench testing of hemispherical probe heads, the methods can be compared side by side in a manner that is currently not available.

The use of a flush air data sensing system for measurement of the flow velocity is examined. The effectiveness as an air data source and the ability to be incorporated into an airframe are compared with the traditional hemispherical sensing head. By investigating the FADS system and its potential incorporation into an atmospheric turbulence probe, an alternative to the hemispherical sensing head is provided that may be more appropriate for use on certain airframes. By consolidating information on the different methods used, an optimal methodology may be selected to match the probe and airframe combination. It is hoped that this information will prove valuable for future designs of atmospheric turbulence probe and carrier aircraft combinations.

1.3 Uses of an Atmospheric Turbulence Probe

When mounted on an airplane, the atmospheric turbulence probe can utilize the mobility of the airplane to report the behavior of atmospheric motions over large areas and time scales. Bunker

describes using an aircraft to determine turbulent components of the atmosphere, "Its greatest advantage lies in its ability to obtain measurements in regions completely inaccessible or accessible only at great cost or time expenditure [3]." As an isolated sensor package, the probe can provide valuable insights into atmospheric behavior in the planetary boundary layer, in clouds, around mountains, or anywhere else of interest in the atmosphere. When combined with other sensors on a suitably equipped airplane, the turbulence probe forms an integral part of atmospheric studies. Specific applications of turbulence probes include determination of carbon sinks and sources, enabling eddy covariance measurements of heat and chemical flux in the planetary boundary layer and studies of air movement responses to orographic forcing.

Determination of carbon sinks and sources is an important factor in determining how the planetary climate is responding to anthropogenic effects. Carbon sinks are areas that display a net absorption of carbon from the atmosphere. Carbon sources, conversely, are areas that display a net release of carbon into the atmosphere. In order to accurately build a picture of whether an area is a net sink or a net source requires knowledge of the flux of carbon into and out of the planetary surface and the atmosphere. As most of this transport occurs at the boundary layer between the atmosphere and the planetary surface, the planetary boundary layer (PBL), the atmospheric turbulence probe is well suited to this type of study, especially when mounted on an airplane that can study large areas of heterogeneous terrain. According to Schimel et al., in order to accurately build a picture of the distribution of carbon sinks and sources, "spatially extensive observations that are temporally repeatable – either inventories or a combination of inventory and eddy covariance data – are required [4]".

Eddy covariance is a method of determining flux, either of temperature or trace gasses, in the planetary boundary layer. By using high frequency data on the behavior of air motion in the

planetary boundary layer, the eddy covariance method can provide a statistical calculation of the fluxes of heat, moisture and trace chemicals in the boundary layer. The PBL is the lowest part of the atmosphere and as such is the interface between the surface of the planet and the surrounding atmosphere. Atmospheric behavior in the PBL is directly influenced by contact with the planetary surface as flow near the surface encounters obstacles that reduce wind speed and introduce random vertical and horizontal velocity components at right angles to the main direction of flow. This turbulence causes vertical mixing throughout the boundary layer and flow velocity, temperature, moisture and chemical concentrations display rapid fluctuations. Crawford and Dobosy (1990), explain the usefulness of an aircraft that is appropriately equipped, "The chemical make-up of our atmosphere and the resulting global environment are largely controlled by trace gas air-surface exchange … The only direct method for air-surface exchange measurement is eddy-covariance … Mobile Flux Platforms (MFPs) instrumented for eddy-covariance are, in principle, a more efficient tool for investigation of air-surface exchange over diverse surface conditions [1]." On an airplane equipped with temperature, humidity and trace gas concentration sensors, the atmospheric turbulence probe becomes an integral part of a MFP capable of eddy-covariance measurement.

The study of air movement responses to orographic forcing also require data on atmospheric behavior to the level of the individual velocity components, such as in validation of mountain wave behavior models and three dimensional flow prediction [5]. Climate modeling is a further field in which the data provided by an atmospheric turbulence probe is useful. Large scale climate models run by supercomputers such as Oak Ridge's Jaguar and Japan's Earth Simulator commonly use vertical and horizontal wind components to model transport of atmospheric tracers [6]. The general assumptions made in large scale climate models come from

data on atmospheric behavior over different surface types. These assumptions may be tested using equipment such as the atmospheric turbulence probe.

1.4 The Relationship Between Atmospheric Velocity Components

Initial studies of atmospheric velocity components were restricted to measurement of airplane response to a turbulent air mass. The turbulent air mass causes the aircraft to be exposed to rapid changes in angle of attack and speed of the oncoming airflow. The airplane response is rapid changes in the lift and therefore vertical acceleration. By recording the vertical accelerations and changes in airspeed, variations in airplane angle of attack can be computed. Once the variations in angle of attack are computed, the variations in gust velocity may then be determined [7]. The relationship between lift and angle of attack varies for each plane depending on factors such as wing and airfoil shape. To achieve accurate gust velocity results, the relationship between the angle of attack and the coefficient of lift for the research aircraft used must be known accurately.

In 1955, Bunker flew a U.S. Navy PBY-6A airplane equipped with a gyroscope, a vertical accelerometer and an anemometer to measure the vertical and horizontal turbulent components of the wind over the ocean. Using this equipment and data on the relationship between the lift coefficient and the angle of attack for his measurement airplane, Bunker estimated accuracies of ±2 cm/sec for the horizontal wind velocity components and ±1 cm/sec for the vertical wind velocity components [3]. Early methods were therefore proven able to determine vertical and horizontal velocity components of the wind to a high level of accuracy. These methods, however, had limiting data collection parameters. Without an instrument capable of measuring ground speed independently, uncertainties introduced by the response of

the aircraft to gusts limited the data collection time period. In addition, there were several conditions which had to be met to allow the method used by Bunker to be used successfully. These were: (i) the airplane is a rigid body, (ii) the attitude of the airplane does not change, (iii) a steady flow has been established over the airfoils, (iv) the airplane flight is level, rectilinear and properly trimmed and (v) the gust is sharp-fronted and symmetrical across the span of the wing [3]. The measurement of vertical velocity components was limited to gusts large enough to affect the whole plane, and the requirement for the airplane to be a rigid body limited the size of gusts measured to a minimum of 18 meters radius [3]. Bunker used a computational method to eliminate phugoid motion by subtracting values averaged over a quarter period of the phugoid oscillation from instantaneous values of turbulent components. This method limited the measurement of gusts to a maximum of 350 meters radius [3]. A straight and level flight run and extensive post processing of the data were also required.

The modern atmospheric turbulence probe is designed to provide valuable data about the atmosphere through which it is travelling by sensing the individual velocity vector components of the probe movement and the individual velocity vector components of the air flowing onto the probe. A vector addition of the vector components is then performed to determine the individual components of velocity of the atmosphere. The vector addition is shown in equation 1.

$$\vec{V}_{flow} + \vec{V}_{probe} = \vec{V}_{atmosphere} \tag{1}$$

In equation 1, V_{flow} is the velocity vector of the airflow onto the probe head, V_{probe} is the velocity vector of the probe itself, and $V_{atmosphere}$ is the velocity vector of the atmosphere that the probe is travelling through. Equation 1 illustrates how the atmospheric velocity vector is calculated from the opposing probe and flow velocity vectors. The addition of velocity vectors does not imply that the magnitudes of the two quantities are added together, but rather that the vectors are combined to form a new vector. In this particular case the velocity quantities are subtracted from each other due to opposite direction components of the two vectors. Due to the airspeed of the aircraft carrying the probe, the measured probe velocity vector (relative to the Earth) and the measured airflow velocity vector (relative to the probe) both have much larger values than the calculated atmospheric velocity vector. It is therefore very important to achieve a high level of accuracy in the probe and flow vectors to arrive at an atmospheric velocity vector that is useful. Beswick defines the necessary resolution of velocity components to be 0.5 to 1.0 m/s for meteorological research [8]. Lenschow, however, requires a greater resolution for atmospheric turbulence measurements: "The available evidence indicates, however, that at heights of 30 m above the earth's surface a wavelength of 5 m and a velocity component resolution of 1 or 2 cm/sec is adequate for most measurements of turbulent energy and turbulent fluxes [9]."

A vector consists of a direction and a magnitude. In order to calculate the probe and flow vectors we therefore need to know the direction and magnitude of the probe motion and the direction and magnitude of the flow motion. The methods to measure each of the vectors in equation 1 have improved as instrumentation and computing technology has improved. The measurement development of the vectors in equation 1 will be traced independently for clarity.

1.5 Development of Flow Velocity Measurement

The use of a boom mounted wind measurement vane allowed the directional component of velocity to be measured directly as shown by Telford and Warner in 1962 [10]. The boom mounted wind vane also allowed the horizontal component of wind velocity to be determined due to the addition of the angle of sideslip data from the wind vanes. The effectiveness of the wind vanes was investigated by Lenschow in 1971 by determining baseline resolutions of velocity components required of the vanes to be 1 or 2 centimeters per second [9]. Two different designs of wind vane were investigated by Lenschow, one with a free swiveling vane design and one with a constrained vane design. The constrained vane measured forces of oncoming air upon the fixed vane using potentiometers and the free vane measured the angles of the flow directly. Lenschow concluded that both methods achieved the necessary velocity component resolution but that each had separate advantages and disadvantages associated with their use. The free vane measured the angles directly and was not sensitive to accelerations encountered in flight, but suffered from bearing friction due to its mounting and therefore had a slower response time. The constrained vane, conversely, did not suffer from bearing friction and had a faster response time, but did register the effects of in flight acceleration and required more calculations to obtain the flow angles due to not measuring the angles directly [9].

In 1973 Armistead and Webb performed a series of flight tests with a hemispherical flow direction sensor, similar to that shown in figure 1, designed to replace wind vanes as a method of measuring angle of attack and angle of sideslip. The hemispherical flow direction sensor consisted of a ¾ inch diameter aluminum hemisphere with a total of five pressure orifices. One pressure port was centrally located and the other four were placed 45° back from the center port on orthogonal planes [11]. Wind tunnel tests of the hemispherical flow direction sensor showed

it to perform well by measuring the pressure differences across the sensor head and using potential flow theory to convert the pressure differences into flow angles. The sensor was mounted on the nose of an F-104 research aircraft also equipped with traditional vanes for the measurement of angles of attack and angles of sideslip. By co-locating the hemispherical flow direction sensor with the angle of attack and angle of sideslip vanes, a quantitative comparison between the two methods was obtained. Flight tests of the hemispherical flow sensor showed an uncertainty in angle of attack of ± 0.35° or less over a Mach number range of 0.5 to 1.8 and over an angle of attack range of 0° to 13° [11]. An additional advantage of the hemispherical flow sensor is the ability to compute dynamic pressure and static pressure independently from the airplane carrying the probe. In a comparison between Mach number calculations using a pitot-static probe and the five pressure orifices of a hemispherical flow direction sensor, however, Armistead and Webb showed the hemispherical flow direction sensor to have a position error two orders of magnitude greater than that of the pitot-static probe over the test ranges [11].

Further refinement of the hemispherical pressure sensing head used to sense flow angles is described by Wyngaard (1988), Crawford and Dobosy (1990, 1991), Wood et al. (1996), and Garman et al. (2006). Wyngaard lays out positioning criteria for mounting a pressure sensing probe on an aircraft. By placing the hemispherical sensing head in a location that is symmetrical around both the horizontal and vertical axes, cross dependence between the horizontal and vertical flux measurements is minimized [12]. Crawford and Dobosy designed a nine hole, "Best Aircraft Turbulence", probe, shown in figure 1, with a hemispherical pressure sensing head by adding four off axis static pressure ports to facilitate measurement of true airspeed. Following Wyngaard's criteria, the probe was mounted on the nose of a pusher airplane (with the propeller at the back of the airplane). Crawford and Dobosy reported angle of attack and angle of sideslip

accuracies of 0.3°, dynamic pressure error of below 1%, and estimated error in relative wind velocity of ±0.25 m/s [1]. Wood et al. reported an angle of attack and an angle of sideslip measurement accuracy of better than 0.25°, based on flight and ground based calibration data [13]. Garman et al. performed a series of in flight calibrations on an upgraded BAT probe and achieved a 1σ measurement precision of approximately 0.02° for an angle of attack of 5° [14]. In all cases, the accuracy of measurements decreased as the airspeed increased and the angle of attack increased above 8°. Therefore, the hemispherical pressure sensing head was shown to be most successful when measuring at low airspeeds of around 50 m/s in straight and level flight, favoring light aircraft in calm conditions.

As the hemispherical head was being refined, a Flush Air Data Sensing (FADS) system was being designed by NASA for use in high angle of attack flight research and atmospheric re-entry vehicles such as the X-33 and the Space Shuttle, to solve the problem of external sensors being destroyed by the friction heat of atmospheric reentry [15]. The FADS system measures pressure differences across the nose of the airplane in the same manner as the hemispherical head but with the pressure ports embedded flush with the hull of the airplane instead of in an external probe, as shown in figure 3. Cobleigh explains, "The FADS concept relies on a mathematical model that relates measured forebody surface pressures to the airdata state [16]." Cobleigh et al. (1999) tested the applicability of the FADS system to a variety of forebody shapes and found that the methodology is universally applicable to blunt-nosed airplane configurations [16].

In 1981, Larson and Siemers flight tested an eighteen hole FADS system installed on a KC-135A airplane and reported measurement uncertainties of ±0.005 in Mach number, ±0.5° in angle of attack, and ±0.75° in angle of sideslip [17]. The angle of attack range over which the FADS system was tested was larger than that of the hemispherical head probes, from -2° to 16°.

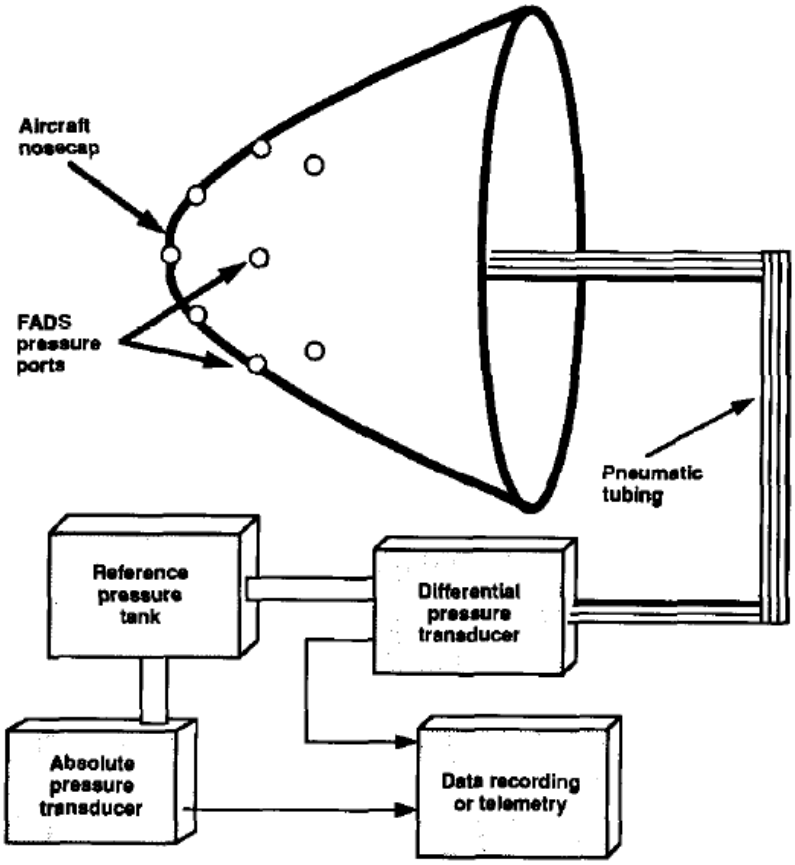

Figure 3. Flush Air Data Sensing system [23].

A series of tests on a prototype orbital reentry vehicle called the X-33 was performed by Whitmore et al. in 1998 that featured a six hole FADS system. Accuracies of ±0.5° absolute accuracy in angle of attack and angle of sideslip and of ±15 lb/ft^2 of dynamic pressure were determined as the minimums required of the system for orbital reentry and were met or exceeded in testing at airspeeds of less than Mach 4.0 [18]. The angle of attack and angle of sideslip accuracy actually increased with Mach number in the subsonic regime, in contrast to the hemispherical probe which decreased in accuracy as the airspeed increased. Angle of attack error ranged from 0.30° at low subsonic speeds to 0.23° approaching the transonic regime. Angle of sideslip accuracy ranged from 0.45° at low subsonic speeds to 0.20° approaching the transonic regime. The angle of attack range for testing was -10° to 25°, the angle of sideslip range for testing was -10° to 16° [18], again demonstrating a larger range than that of the hemispherical probe testing. Testing by Cobleigh et al. in 1999 showed that the shape of the forebody contributed to the successful angle of attack range over which the FADS system was able to achieve the desired accuracies for orbital reentry. Spherical shapes performed best over a large angle of attack range, up to 30° angle of attack. As the forebody shapes become less spherical, the angle of attack range that is measureable decreases to around 10° [16].

The FADS system therefore has demonstrated a superior ability to resolve flow angles over larger airspeed and angle of attack ranges than that of the hemispherical flow sensing head. The accuracies of both systems appear to be almost identical, with sensor location considerations becoming very important when considering the aircraft and sensor system combined. The drawback of the FADS system is that it is not a “strap down” system capable of being easily installed and moved to and from different aircraft and the calculations used to determine flow vectors are nonlinear in nature. Both systems require careful calibration when mounted on an

aircraft, however. The hemispherical probe is a portable system and therefore may be moved from one research aircraft to another, but the calibrations of the system, particularly the calibrations for static pressure position error for each new probe-airframe combination that must be obtained to achieve meaningful data from the probe, and the consideration of individual design constraints of the host airplane in order to achieve an optimal placement location narrow the complexity gap between the two systems. The applicability of the FADS system to a wide variety of blunt forebody shapes may make it a more attractive, albeit permanent, system to use, depending on the aircraft used. Only one calibration is required for the static pressure position error for each FADS installation. The nonlinear calculations used in the FADS system are well within the computation power of modern computer systems.

1.6 Development of Probe Velocity Measurement

The development of the probe velocity measurement has advanced mostly along the lines of miniaturization and sensor accuracy. The addition of accurate GPS systems has also contributed enormously to overall system accuracy. Early systems such as used by Bunker in 1954 and Telford and Warner in 1962 employed an anemometer, a vertical accelerometer and a gyroscope mounted inside the aircraft to determine total airspeed, vertical accelerations and attitude. The gyroscopes used were not of sufficient quality to provide accurate information over time periods longer than 20 to 30 seconds of flight time [3], [10]. Without modern microprocessors the motion information was only available through post processing of photographic trace data by hand. In 1968, Axford introduced the use of a high quality inertial navigation platform with instruments capable of measurement for 5 to 10 minutes of flight time [19], a significant

improvement over the previous systems. This system had the disadvantage of being very large, however, and expensive. Large systems are by necessity placed some distance away from the point of airflow vector measurement, decreasing the measurement accuracy due to different rates of pitch, roll and yaw between the point of origin and the point of measurement [19]. By assuming the aircraft to be a rigid body, these rates of rotation may be considered transformations and therefore allow additional correction factors to compensate in the calculation of the atmospheric velocity vector.

All early systems suffered from the effects of additional sources of error introduced into the measurement of aircraft behavior. Telford and Warner state that it is "necessary to determine both aircraft altitude changes and acceleration to a high precision, while this can be done, the determination of acceleration is usually complicated by structural vibrations in the aircraft imposing relatively high frequency oscillations on the recorded accelerometer trace [10]." The use of a modern electronic recording system allows the structural vibrations to be filtered out of the accelerometer data. Errors in aircraft altitude changes may be reduced by completing a proper static pressure position error calibration flight test of the aircraft to ensure that the altitude changes reported are accurate. A further source of error that Telford and Warner encountered was the effect of aircraft inclination from level flight causing the accelerometers to read inaccurately. The effect caused large errors when the inclination approached values of 20°, but smaller errors when the inclination was at 1 or 2 degrees [10].

Crawford and Dobosy designed the Best Air Turbulence (BAT) probe with small accelerometers capable of being mounted at the same location as the hemispherical flow sensing head. The BAT probe also utilizes small GPS antennas to determine the angular motion of the probe head directly without the need for a correction factor due to physical separation of sensor

for the flow and probe velocities. Modern inertial measurement units can also be used to achieve the angular rates of probe motion and are small enough to be placed next to the flow sensing location. With modern technology the cost and size issues of a dedicated inertial navigation system are avoided. By integrating a GPS system into the measurement system, problems with gyroscopic drift can be minimized by the stable reference system that a GPS provides.

1.7 Development of Atmospheric Motion Velocity Measurement

The accuracy of the atmospheric motion velocity is directly dependent upon the accuracy of the flow and probe velocities measurement. The length of time over which measurements may be taken has also improved enormously. Axford, for example was able to resolve vertical motions of around 2.5 m/s but only for three minutes at a time due to gyroscopic drift in the inertial platform [19]. The usefulness of the aircraft as a research platform was limited by this short measuring time. Advances in the accuracies described in previous systems gave Crawford and Dobosy a vertical vector component accuracy of 0.25 m/s over a measurement range that is only limited by the endurance of the aircraft carrying the probe [20].

The use of modern computers has simplified the application of potential flow theory to determine the flow velocities and the final calculation of atmospheric motion velocities. Depending on the method used, the acquisition of all required data either comes directly from the turbulence measurement system or some combination of data from aircraft systems and from the probe. Comparisons between the different measurement techniques and their applicability to various airframe and probe combinations are a major focus of this thesis.

CHAPTER 2: MEASUREMENT THEORY

2.1 Overview

The goal of the present turbulence measurement is to obtain the individual components of the airflow velocity through which the aircraft is flying. The turbulence measurement probe achieves this by obtaining data on the true airspeed of the incident airflow, the incident angle of the airflow upon the probe sensing head, and data on the true airspeed and orientation of the probe head itself. There are several different methods of obtaining this information from the turbulence measurement probe, all of which are based upon potential flow theory. In this chapter, five of these methods are presented and explained terms of the measured parameters specific to each method. These methods are: the Rosemount Engineering High Resolution method, the Rosemount Engineering Low Resolution method, the NCAR method, the Ekman method for the BAT probe, and the method used by NASA for the FADS system. Each method uses a different set of calculations to determine the angle of attack and angle of sideslip of the flow incident upon the measurement system. All methods are based on potential flow around a sphere; all differences are all due to the methods of obtaining air data and the sources of air data available for a particular application. The choice of terms to denote the High Resolution and Low Resolution methods was a decision made by the Rosemount Engineering Corporation that is not exactly clear. It appears to relate to the High Resolution method having a better accuracy when using a sensitivity coefficient to determine flow angles.

A hemispherical probe head with pressure transducers mounted in a cruciform layout, as in figure 4, is used to determine the direction and magnitude of the incident flow upon the head by measuring pressure differences across the probe head. Using a FADS layout, as in figure 5,

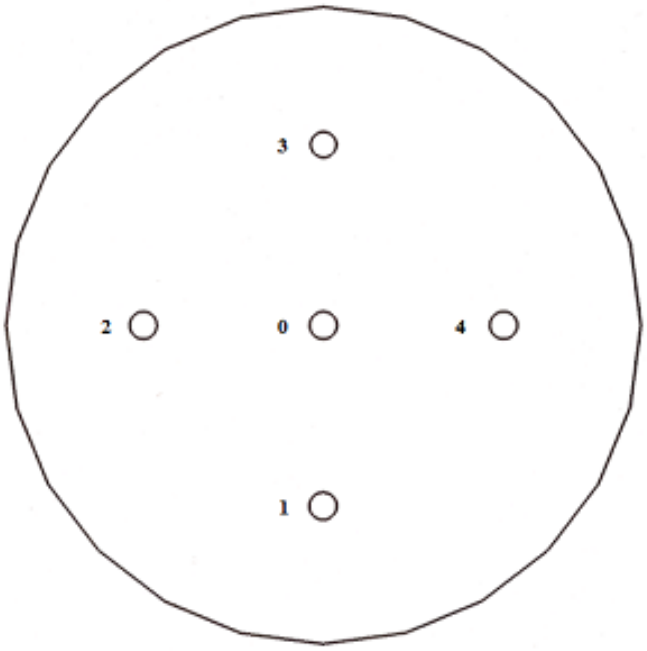

Figure 4. Hemispherical probe head with cruciform arrangement of pressure port locations.

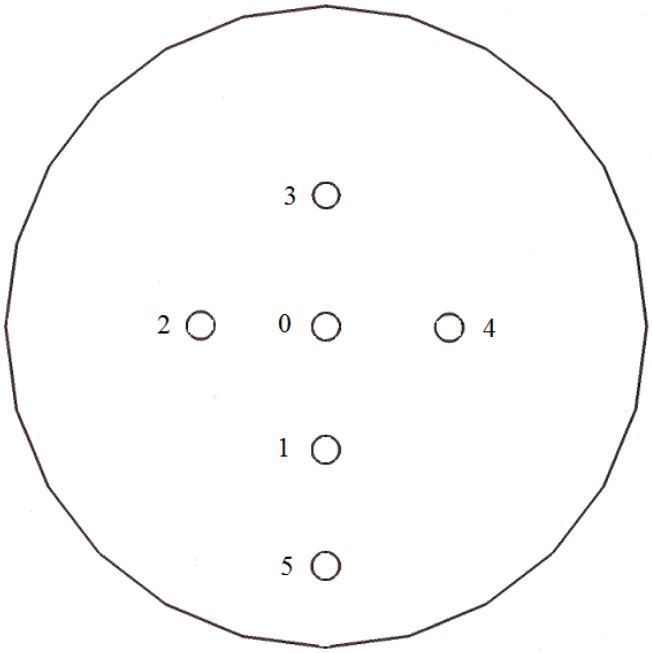

Figure 5. Hemispherical probe head with FADS arrangement of pressure port locations.

additional pressure sensors are used and may be embedded directly into an aircraft nose cone that only needs to approximate a hemisphere. Supporting instrumentation includes a GPS, an IMU and temperature sensors that are used in determination of both incident airflow true airspeed and probe true airspeed and orientation.

The governing equation is a vector addition of the incident airflow upon the sensor head, V_{flow}, and the probe movement through the airflow, V_{probe}, as shown in Equation 1 previously. The magnitude of both the incident airflow vector and the sensor vector are comparatively large, and the vectors are in opposing directions, so the resulting airflow vector is comparatively small. Therefore, the incident airflow vector and the sensor airflow vector must be measured with a high degree of accuracy in order to obtain a meaningful airflow vector. The level of accuracy available is determined by the sensing equipment and the data processing method.

2.2 True Airspeed Measurement

The magnitude component of the airflow vector is determined by the true airspeed. Information from the pressure transducers and the temperature sensor contribute towards the true airspeed measurement. Equation 2 shows the formula for true airspeed, using the ratio of specific heats $\gamma = c_p/c_v$ and the gas constant R, as a function of the free stream static pressure p_0, the total (stagnation) pressure p_1, and the free stream static temperature T_0.

$$V_{true} = \sqrt{\left(\frac{2\gamma R T_0}{\gamma - 1}\right)\left[\left(\frac{p_1}{p_0}\right)^{\frac{\gamma - 1}{\gamma}} - 1\right]} \tag{2}$$

A simpler method for determination of true airspeed under subsonic compressible flow conditions is to use the speed of sound at sea level a_{std}, and the standard atmospheric temperature at sea level T_{std}, as constants. Using these two constants then allows the determination of true airspeed as a function of impact pressure q_c, static pressure p_0, and static air temperature T_0, as shown in Equation 3.

$$V_{true} = a_{std} \sqrt{\frac{5T_0}{T_{std}} \left[\left(\frac{q_c}{p_0} + 1 \right)^{\frac{2}{7}} - 1 \right]} \tag{3}$$

2.3 Flow Angle Measurement

The direction components of the airflow velocity are determined as the angle of attack and angle of sideslip of the incident flow on the hemispherical pressure sensing head. The design of the turbulence measurement system governs which parameters can be measured directly and which are subsequently calculated. Table 1 summarizes the differences between the methods. As can be seen from Table 1, the high Resolution, Low Resolution, NCAR, and Ekman models only differ in the measurement of one parameter each, but this parameter changes the way in which the flow angles, and later the dynamic and static pressures, are determined.

All the models are based upon the assumption of potential flow across the sensing head. Since the flow encountered by an aircraft is irrotational this assumption is valid. The potential flow equation for pressure distribution over a sphere that describes the pressure at a chosen point on the sphere is given by Equation 4.

Table 1: Comparison of Methods for Determination of Flow Angles

Method	Measured Parameters	Constants	Calculated Parameters
Rosemount High Resolution	$p_0, p_1, p_2, p_3, p_4.$	θ, ϕ	$\delta_k p, q, p_s, \alpha, \beta$
Rosemount Low Resolution	$p_0, p_1, p_2, p_3, p_4, q$	θ, ϕ	p_s, α, β
NCAR	$p_0, p_1, p_2, p_3, p_4, p_s.$	θ, ϕ	q, α, β
Ekman	$p_0, p_1, p_2, p_3, p_4, p_r.$	θ, ϕ, ϕ_r	$\delta p_y, \delta p_z, \delta p_x, q, p_s$

$$p(n) = p_s + \frac{q}{4}\left[9\left(\vec{N}\cdot\vec{n}\right)^2 - 5\right] \tag{4}$$

Equation 4 describes the relationship between the pressure at a chosen point on a sphere p_n, to the static pressure p_s, the impact pressure q_c, a unit direction vector normal to the stagnation point of the sphere N, and a normal direction vector at the chosen point on a sphere n. In terms of the unit direction vectors for the probe coordinate system, designated i, j, and k, the unit vector N is given by Equation 5.

$$N = \frac{1}{D}i - \frac{\tan\beta}{D}j - \frac{\tan\alpha}{D}k \tag{5}$$

Where α and β are the angle of attack and angle of sideslip, respectively. The D term is a normalizing factor to create the unit vector and is defined by Equation 6.

$$D = \sqrt{1 + \tan^2\alpha + \tan^2\beta} \tag{6}$$

Solving for the three unknowns of dynamic pressure, angle of attack, and angle of sideslip requires three equations relating the unknown quantities to each other. The pressure differences across the hemispherical sensor head can be used to accomplish this.

Pressure differences between each of the four outer pressure ports and the center port can be derived. The generic form of the pressure differences follows the form of Equation 7.

$$\delta_k p = p_0 - p_k \; ; k = 1,2,3,4 \tag{7}$$

Where p is pressure, p_0 is static pressure and k is an identifier for a pressure port location. The locations of the pressure ports are shown in Figures 4 and 5. Using Equation 4, the generic form of Equation 7 can be expanded to include the unknowns required.

$$\delta_k p = \frac{9}{4} q \left[\left(\overrightarrow{N} \cdot \vec{n}_0 \right)^2 - \left(\overrightarrow{N} \cdot \vec{n}_k \right)^2 \right] \tag{8}$$

Equation 8 can then be used to calculate the specific pressure differences between the outer ports and the center port.

$$\delta_1 p = \frac{9}{4} q \left[\left(\frac{1}{D} \right)^2 - \left(\frac{1}{D} \cos\phi + \frac{\tan\beta}{D} \sin\phi \right)^2 \right] \tag{9a}$$

$$\delta_2 p = \frac{9}{4} q \left[\left(\frac{1}{D} \right)^2 - \left(\frac{1}{D} \cos\theta + \frac{\tan\alpha}{D} \sin\theta \right)^2 \right] \tag{9b}$$

$$\delta_3 p = \frac{9}{4} q \left[\left(\frac{1}{D} \right)^2 - \left(\frac{1}{D} \cos\phi - \frac{\tan\beta}{D} \sin\phi \right)^2 \right] \tag{9c}$$

$$\delta_4 p = \frac{9}{4} q \left[\left(\frac{1}{D} \right)^2 - \left(\frac{1}{D} \cos\theta - \frac{\tan\alpha}{D} \sin\theta \right)^2 \right] \tag{9d}$$

Equations 9 can then be used to relate the pressure differences between ports to the known locations of the ports, denoted by the clock and cone angles of individual ports, ϕ and θ respectively, the dynamic pressure q, and the angle of attack α and angle of sideslip β of the incident flow.

2.4 High Resolution Model

The High Resolution model uses parameters measured solely at the sensing head to determine the angle of attack and angle of sideslip. This method can be used to obtain either estimated or exact values for both the angle of attack and angle of sideslip solutions. Estimated values relate the calculated angle of attack and angle of sideslip to the measured pressures by utilizing a

sensitivity coefficient obtained by using the exact method. The sensitivity coefficient is determined by the location of the pressure ports on the hemispherical sensing head. The estimated method has the advantage of fewer calculation steps to obtain a flow angle. The estimated solutions are shown in Equations 10.

$$\alpha = \frac{p_2 - p_4}{K_1\left[(p_0 - p_2) + \frac{p_2 - p_4}{2}\right]} = \frac{2}{K_1}\left[\frac{\delta_4 p - \delta_2 p}{\delta_4 p + \delta_2 p}\right] \tag{10a}$$

$$\beta = \frac{p_1 - p_3}{L_1\left[(p_0 - p_1) + \frac{p_1 - p_3}{2}\right]} = \frac{2}{L_1}\left[\frac{\delta_3 p - \delta_1 p}{\delta_3 p + \delta_1 p}\right] \tag{10b}$$

Both the left and right sides of Equations 10 represent a different method of obtaining the pressures, either using absolute pressure measurement or differential pressure measurement, but the two equations are equal. The K_1 and the L_1 terms are sensitivity coefficients that are dependent upon the locations of the measurement ports. The values for the sensitivity coefficients are calculated using the equations for exact solutions.

The exact solutions to the angle of attack and angle of sideslip are obtained by first inserting Equations 9 into Equations 10, as shown in Equations 11.

$$\frac{\delta_4 p - \delta_2 p}{\delta_4 p + \delta_2 p} = \frac{\frac{1}{D}\frac{\tan\alpha}{D}\sin 2\theta}{\left(\left(\frac{1}{D}\right)^2 - \left(\frac{\tan\alpha}{D}\right)^2\right)\sin^2\theta} = \left[\frac{2\tan\alpha}{1-\tan^2\alpha}\right]\frac{1}{\tan\theta} = \frac{\tan 2\alpha}{\tan\theta} \tag{11a}$$

$$\frac{\delta_3 P - \delta_1 p}{\delta_3 p + \delta_1 p} = \frac{\frac{1}{D}\frac{\tan\beta}{D}\sin 2\phi}{\left(\left(\frac{1}{D}\right)^2 - \left(\frac{\tan\beta}{D}\right)^2\right)\sin^2\phi} = \left[\frac{2\tan\beta}{1-\tan^2\beta}\right]\frac{1}{\tan\phi} = \frac{\tan 2\beta}{\tan\phi} \tag{11b}$$

Equations 11 express the measured pressures across the sensor head to the locations of the pressure ports and the angle of attack and angle of sideslip of the incident airflow. To obtain an equation directly relating the angle of attack and angle of sideslip to the measured parameters, it is useful to define secondary quantities F_α and F_β, as given by Equations 12.

$$F_\alpha = \frac{\tan\theta}{2}\left[\frac{\delta_4 p - \delta_2 p}{\delta_4 p + \delta_2 p}\right] \tag{12a}$$

$$F_\beta = \frac{\tan\phi}{2}\left[\frac{\delta_3 p - \delta_1 p}{\delta_3 p + \delta_1 p}\right] \tag{12b}$$

Equations 12 are obtained by rearranging the terms in Equations 11. All of the parameters used in Equations 12 are measured directly by the atmospheric turbulence measurement system. Substitution of the secondary quantities F_α and F_β, into Equations 11 allows the angle of attack

and angle of sideslip to be written in quadratic form, as given in Equations 13a and 13b, respectively.

$$\left(1 - \tan^2 \alpha\right) F_\alpha = \tan\alpha \tag{13a}$$

$$\left(1 - \tan^2 \beta\right) F_\beta = \tan\beta \tag{13b}$$

Equations 13 can be solved explicitly for the flow angles, using the small angle approximation $\tan x \cong x$. This provides first order estimates of the exact solutions for angle of attack and angle of sideslip, as shown in Equations 14a and 14b, respectively.

$$\alpha \cong \tan\alpha = \frac{2 F_\alpha}{\left(1 + \sqrt{1 + 4 F_\alpha^2}\right)} \tag{14a}$$

$$\beta \cong \tan\beta = \frac{2 F_\beta}{\left(1 + \sqrt{1 + 4 F_\beta^2}\right)} \tag{14b}$$

Once the exact solutions have been determined in terms of measured parameters only, the sensitivity coefficients used in the estimated calculations may be determined by comparing the estimated values to the first order approximation. The equation for the sensitivity coefficients is shown in Equations 15.

$$K_1 = \left(\frac{\pi}{45 \tan\theta} \right) \text{deg}^{-1} \tag{15a}$$

$$L_1 = \left(\frac{\pi}{45 \tan\phi} \right) \text{deg}^{-1} \tag{15b}$$

It can be seen from Equations 15 that for the High Resolution model, the sensitivity coefficients are inversely proportional to the angle of measurement port separation. Reference to Leise and Masters shows the 'optimal' port location angle for pressure measurement to be at 41.81° separation, corresponding to a sensitivity coefficient of 0.0780535 deg^{-1}. The significance of this location is discussed under the section for the Ekman model. Leise and Masters also list the Rosemount Engineering Corporation recommended sensitivity coefficient as 0.079 deg^{-1}, which corresponds to a port separation angle of 41.5°. The Rosemount Engineering Corporation lists the useable range of the High Resolution model to be ± 45° at Mach numbers less than 0.5.

2.5 Low Resolution Model

The Low Resolution model is designed to be used when a separate source of dynamic pressure is available. Measured pressures, either differential or absolute, across the sensor head are combined with dynamic pressure to obtain flow angle of attack and angle of sideslip. The estimated form of flow angle measurement is shown in Equations 16.

$$\alpha = \frac{p_2 - p_4}{K_2 q_c} = \frac{\delta_4 p - \delta_2 p}{K_2 q_c} \tag{16a}$$

$$\beta = \frac{p_1 - p_3}{L_2 q_c} = \frac{\delta_3 p - \delta_1 p}{L_2 q_c} \tag{16b}$$

The sensitivity coefficients K_2 and L_2 used here are different from those used in the high resolution model. The values for the sensitivity coefficients are calculated using the equations for exact solutions.

The exact solutions to the angle of attack and angle of sideslip are obtained by first inserting Equations 9 into Equations 16, as shown in Equations 17.

$$\frac{p_2 - p_4}{q} = \frac{9}{2}\left(\frac{1}{D}\right)\frac{\tan\alpha}{D}\sin 2\theta = \frac{\frac{9}{2}\tan\alpha \sin 2\theta}{D^2} \tag{17a}$$

$$\frac{p_1 - p_3}{q} = \frac{9}{2}\left(\frac{1}{D}\right)\frac{\tan\beta}{D}\sin 2\phi = \frac{\frac{9}{2}\tan\beta \sin 2\phi}{D^2} \tag{17b}$$

Equations 17 express the measured pressures across the sensor head to the locations of the pressure ports, the sensed dynamic pressure, and the angle of attack and angle of sideslip of the incident airflow. To obtain an equation directly relating the angle of attack and angle of sideslip to the measured parameters, it is useful to define secondary quantities G_α and G_β, as given by Equations 18.

$$G_\alpha = \frac{2}{9\sin 2\theta}\left[\frac{p_2 - p_4}{q}\right] \tag{18a}$$

$$G_\beta = \frac{2}{9\sin 2\phi}\left[\frac{p_1 - p_3}{q}\right] \tag{18b}$$

Equations 18 are obtained by rearranging the terms in Equations 17. The parameters used in Equations 18 are measured directly by the atmospheric turbulence measurement system and a separate source of dynamic pressure. Substitution of the secondary quantity into Equations 17 allows the angle of attack and angle of sideslip to be written in quadratic form, as given in Equations 19a and 19b, respectively.

$$\tan\alpha = G_\alpha \left(1 + \tan^2\beta + \tan^2\alpha\right) \tag{19a}$$

$$\tan\beta = G_\beta \left(1 + \tan^2\beta + \tan^2\alpha\right) \tag{19b}$$

Equations 19 can be solved explicitly for the flow angles, using the small angle approximation $\tan x \cong x$. In the Low Resolution model, the solutions for angle of attack and angle of sideslip are coupled, as can be seen in Equations 19. To reduce the cross dependence of the two solutions, it is possible to take quotients of the two equations, resulting in $G_a \tan\beta = G_\beta \tan\alpha$, and the closed form solutions to the low resolution model are shown in Equations 20.

$$\alpha \cong \tan\alpha = \frac{2\,G_\alpha}{1 + \sqrt{1 - 4\left(G_\alpha^2 + G_\beta^2\right)}} \tag{20a}$$

$$\beta \cong \tan\beta = \frac{2\,G_\beta}{1 + \sqrt{1 - 4\left(G_\alpha^2 + G_\beta^2\right)}} \tag{20b}$$

Equations 20 are still weakly coupled with the $G_\alpha^2 + G_\beta^2$ term common to both angle of attack and angle of sideslip equations. Since both of these terms are calculated from measured parameters this does not pose any significant problem to calculating the flow angles, however.

Once the exact solutions have been determined in terms of measured parameters only, the sensitivity coefficients used in the estimated calculations may be determined by comparing the estimated values to the first order approximation. The equation for the sensitivity coefficients is shown in Equations 21.

$$K_2 = \left(\frac{\pi \sin 2\theta}{40}\right) \text{deg}^{-1} \tag{21a}$$

$$L_2 = \left(\frac{\pi \sin 2\phi}{40}\right) \text{deg}^{-1} \tag{21b}$$

It can be seen from Equations 21 that for the Low Resolution model, the sensitivity coefficients are proportional to the angle of measurement port separation. The sensitivity coefficients for the Low Resolution model are equal to those of the High Resolution model at a port separation angle of 41.81°, the 'optimal' angle from Leise and Masters. Leise and Masters also list the Rosemount recommended sensitivity coefficient as 0.088 deg^{-1}, which does not appear to have a theoretical basis. Reference to Leise and Masters shows the Rosemount useable range of the Low Resolution model to be ± 12° at Mach numbers less than 0.5.

2.6 NCAR Model

The National Center for Atmospheric Research model is a hybrid between the high resolution and the low resolution models. The dynamic pressure used in the Low Resolution model is replaced with the pressure difference between the center port pressure and static pressure reported from a separate source ($p_0 - p_s$). The estimated form of flow angle measurement is shown in Equations 22.

$$\alpha = \frac{p_2 - p_4}{K_3(p_0 - p_s)} = \frac{\delta_4 p - \delta_2 p}{K_3(p_0 - p_s)} \tag{22a}$$

$$\beta = \frac{p_1 - p_3}{L_3(p_0 - p_s)} = \frac{\delta_3 p - \delta_1 p}{L_3(p_0 - p_s)} \tag{22b}$$

Ideally, the quantity ($p_0 - p_s$) should be measured directly with a differential pressure transducer. Depending on the design of the turbulence probe it may be impossible to directly measure static pressure however, and this may invalidate the approach for some designs. The sensitivity coefficients K_3 and L_3 used here agree with those used in the calculations for the Low Resolution model.

Using the pressure difference Equations 9, the exact solutions for angle of attack and angle of sideslip are obtained, however, an additional equation must be used for the pressure difference ($p_0 - p_s$). The use of Equation 8 allows Equation 23 to be determined.

$$p_0 - p_s = q\left[\frac{1 - \frac{5}{4}\left(\tan^2\beta + \tan^2\alpha\right)}{D^2}\right] \tag{23}$$

Once Equation 23 has been established, the substitution of Equations 9 and 23 into equations 22 can be accomplished, resulting in Equations 24.

$$\frac{p_2 - p_4}{p_0 - p_s} = \frac{\frac{9}{2}\tan\alpha \sin 2\theta}{q\left[1 - \frac{5}{4}\left(\tan^2\beta + \tan^2\alpha\right)\right]} \tag{24a}$$

$$\frac{p_1 - p_3}{p_0 - p_s} = \frac{\frac{9}{2}\tan\beta \sin 2\phi}{q\left[1 - \frac{5}{4}\left(\tan^2\beta + \tan^2\alpha\right)\right]} \tag{24b}$$

Equations 24 express the measured pressures across the sensor head to the locations of the pressure ports, the pressure difference between the static pressure and the center port pressure, and the angle of attack and angle of sideslip of the incident airflow. To obtain an equation directly relating the angle of attack and angle of sideslip to the measured parameters, it is useful to define secondary quantities H_α and H_β, as given by Equations 25.

$$H_{\alpha} = \frac{2}{9\sin 2\theta}\left[\frac{p_2 - p_4}{p_0 - p_s}\right] \tag{25a}$$

$$H_{\beta} = \frac{2}{9\sin 2\phi}\left[\frac{p_1 - p_3}{p_0 - p_s}\right] \tag{25b}$$

Equations 25 are obtained by rearranging the terms in Equations 24. The parameters used in Equations 18 are measured directly by the atmospheric turbulence measurement system and a separate source of static pressure. Substitution of the secondary quantity into Equations 24 allows the angle of attack and angle of sideslip to be written in quadratic form, as given in Equations 26a and 26b, respectively.

$$\tan\alpha = H_{\alpha}\left[1 - \frac{5}{4}\left(\tan^2\alpha + \tan^2\beta\right)\right] \tag{26a}$$

$$\tan\beta = H_{\beta}\left[1 - \frac{5}{4}\left(\tan^2\alpha + \tan^2\beta\right)\right] \tag{26b}$$

Equations 19 can be solved explicitly for the flow angles, using the small angle approximation $\tan x \cong x$. In the NCAR model, the solutions for angle of attack and angle of sideslip are coupled, as can be seen in Equations 26. To reduce the cross dependence of the two solutions, it

is possible to take quotients of the two equations, resulting in $H_a \tan\beta = H_\beta \tan\alpha$, and the closed form solutions to the NCAR model are shown in Equations 27.

$$\alpha \cong \tan\alpha = \frac{2 H_\alpha}{\left[1 + \sqrt{1 + 5\left(H_\alpha^2 + H_\beta^2\right)}\right]} \tag{27a}$$

$$\beta \cong \tan\beta = \frac{2 H_\beta}{\left[1 + \sqrt{1 + 5\left(H_\alpha^2 + H_\beta^2\right)}\right]} \tag{27b}$$

Equations 20 are still weakly coupled with the $H_\alpha^2 + H_\beta^2$ term common to both angle of attack and angle of sideslip equations. Since both of these terms are calculated from measured parameters this does not pose any significant problem to calculating the flow angles, however.

2.7 Ekman Model

None of the above three methods for determination of angle of attack, dynamic pressure and static pressure are ideal for use with the design of a nine hole probe, such as the Crawford and Dobosy BAT probe. The main difference between the BAT probe design and that of the standard five hole probe is the addition of four reference pressure ports, p_r, that are used to estimate the static pressure. The relationship between the reference pressure ports and static

pressure measurement is illustrated by converting the potential flow equation from vector quantities to trigonometric form using the identity $N \cdot n = \cos\gamma$, where γ is the location of the stagnation point of the incident flow. The resulting potential flow equation is then shown in Equation 28.

$$p(n) = p_s + q\left(1 - \frac{9}{4}\sin^2\gamma\right) \tag{28}$$

From Equation 28 it can be seen that, if the reference pressure ports are placed at a 41.81° angle from the center of the probe head, the $\left(1 - \frac{9}{4}\sin^2\gamma\right)$ term reduces to zero and therefore the pressure reported by the reference ports will be theoretically equal to the static pressure. The relationship between static pressure and reference pressure is only equal when the incident flow angle of attack and angle of sideslip is zero. An average of the four reference pressure ports is therefore made to eliminate any bias introduced by the incident flow angle. The advantage of this is that more of the required parameters can be measured directly, instead of being estimated, and all the measurements are accomplished by the probe itself, with no outside sources of information required.

The Ekman model differs from the previous three models because none of the previous models match the configuration of the Crawford and Dobosy BAT probe, in which the measured pressures are defined in Equations 29.

$$\delta p_y = p_1 - p_3 \tag{29a}$$

$$\delta p_z = p_2 - p_4 \tag{29b}$$

$$\delta p_x = p_0 - p_r \tag{29c}$$

$$p_r = \frac{p_{r_1} + p_{r_2} + p_{r_3} + p_{r_4}}{4} \tag{29d}$$

The pressure differences measured are therefore the difference between left and right ports, δp_y, the difference between bottom and top ports, δp_z, and the difference between center port and the averaged values for the reference ports, δp_x.

The Ekman model is similar to the NCAR model, differing in the calculation of static pressure. A slightly different form is used to relate the static pressures to the reference pressures than that described in equation 31, but the results are the same. Equations 4 and 5 are then used to relate the pressure differences across the sensor head to the flow angles of attack and sideslip in Equations 30a and 30b, respectively.

$$\delta p_z = 9\, q\, \frac{\sin\theta \cos\theta}{D^2} \tan\alpha \tag{30a}$$

$$\delta p_y = 9\, q\, \frac{\sin\phi \cos\phi}{D^2} \tan\beta \tag{30b}$$

To compute δp_x, an equation must first be derived for the reference pressure, p_r. When the reference ports are at an angle ϕ_r from the center port, p_r is shown in Equation 31.

$$p_r = p_s + \frac{q}{4}\left[9\, \frac{\cos^2\phi_r + 0.5\left(\tan^2\alpha + \tan^2\beta\right)\sin^2\phi_r}{D^2} - 5\right] \tag{31}$$

Equation 32 then shows the appropriate form for the pressure difference δp_x.

$$\delta p_x = p_0 - p_r = \frac{9q}{8\, D^2} \sin^2\phi_r \left(3 - D^2\right) \tag{32}$$

There are now a closed set of equations that relate the flow angles α and β and the dynamic pressure q. The system of equations can be solved by defining the ratios shown in Equations 33.

$$H_z = \frac{\sin^2\phi_r}{8 \sin\theta \cos\theta}\ \frac{\delta p_z}{\delta p_x} \tag{33a}$$

$$H_y = \frac{\sin^2 \phi_r}{8 \sin\phi \cos\phi} \frac{\delta p_y}{\delta p_x} \tag{33b}$$

Using the ratios defined in Equations 33 and the small angle approximation, the flow angles can then be obtained directly from the measured values as shown in Equations 34.

$$\alpha \cong \tan\alpha = \frac{4 H_z}{1 + \sqrt{1 + 8\left(H_y^2 + H_z^2\right)}} \tag{34a}$$

$$\beta \cong \tan\beta = \frac{4 H_y}{1 + \sqrt{1 + 8\left(H_y^2 + H_z^2\right)}} \tag{34b}$$

The Ekman method allows the nine holes design of the Crawford and Dobosy BAT probe to be fully utilized and does not require any additional information to obtain the incident flow data.

It should be noted that wind tunnel testing on the Crawford and Dobosy BAT probe indicated that locating the reference ports at $\phi_r = 41.81°$ did not allow an accurate estimation of static pressure to be made. This does not support the mathematical model of static pressure estimation. The ports were subsequently moved back to 45°, which returned a closer agreement between p_r and p_s. This causes some problems in the application of Equations 31 through 34

because the ϕ_r value is used as a constant. As Ekman explains, "In the past, the original angles have been used but this may not be the best approach. The issue is difficult to resolve, because the movement of ϕ_r from 41.81° to 45° was done to counter viscosity effects which are totally ignored in the derivations…"

2.8 Dynamic Pressure and Static Pressure Measurement

Estimation of dynamic pressure for the Ekman model is accomplished by solving Equation 32 for *q*, and requires that the flow angles have been calculated, as shown in Equation 35.

$$q = \frac{8}{9}\frac{\delta p_x}{\sin^2\phi_r}\frac{1+\tan^2\alpha+\tan^2\beta}{2-\tan^2\alpha-\tan^2\beta} \tag{35}$$

The use of a separate pressure measurement system for reference pressure in the Crawford and Dobosy BAT probe allows the static pressure to be estimated using Equation 31, once the flow angles and the dynamic pressure have been calculated. The resulting equation for exact static pressure is shown in Equation 36.

$$p_s = p_r - \frac{q}{4}\left[9\frac{\cos^2\phi_r + 0.5\left(\tan^2\alpha+\tan^2\beta\right)\sin^2\phi_r}{D^2} - 5\right] \tag{36}$$

Estimation of dynamic pressure using the NCAR method is accomplished by solving Equation 23 for q in a manner similar to the Ekman method, and requires that the flow angles have been calculated, as demonstrated in Equation 37.

$$q = (p_0 - p_s)\left[1 + \frac{9\left(\tan^2\alpha + \tan^2\beta\right)}{4 - 5\left(\tan^2\alpha + \tan^2\beta\right)}\right] \tag{37}$$

The NCAR model obtains static pressure from a separate source so this quantity is not calculated with the NCAR model. A check of the system integrity may be performed by calculating static pressure using Equation 23 and comparing the result to that obtained by the static pressure sensor used in the model if desired.

With the Low Resolution model, dynamic pressure is obtained from a separate source and therefore does not need to be calculated. Static pressure is estimated from the potential flow model and measured pressures. Using the center port pressure and the potential flow Equation 4, an expression for the static pressure estimation is given by Equation 38.

$$p_s = p_0 - \frac{q\left[1 + \frac{5}{4}\left(\tan^2\alpha + \tan^2\beta\right)\right]}{D^2} \tag{38}$$

The High Resolution model obtains dynamic pressure by averaging the differential pressures between the four outer pressure ports and the center port, denoted $<\delta p>$, as shown by Equation 39.

$$<\delta p> = \frac{\delta_1 p + \delta_2 p + \delta_3 p + \delta_4 p}{4} \tag{39}$$

Then expanding Equation 39 by inserting Equations 9 gives Equation 40.

$$<\delta p> = \frac{9}{8} q \left[\left(\left(\frac{1}{D} \right)^2 - \left(\frac{\tan\beta}{D} \right)^2 \right) \sin^2 \phi + \left(\left(\frac{1}{D} \right)^2 - \left(\frac{\tan\alpha}{D} \right)^2 \right) \sin^2 \theta \right] \tag{40}$$

Equation 40 can be solved for q once the flow angle of attack and angle of sideslip are known, as shown in Equation 41.

$$q = \frac{4 <\delta p>}{9 \sin^2 \theta} \left[1 + \frac{3 \left(\tan^2 \alpha + \tan^2 \beta \right)}{2 - \left(\tan^2 \alpha + \tan^2 \beta \right)} \right] \tag{41}$$

Determination of static pressure with the High Resolution model follows the same procedure as for the Low Resolution model, as shown in Equation 38.

2.9 Flush Airdata Sensing

The following description of the FADS model is adapted from Whitmore *et al*, 1998. The Flush Airdata Sensing system uses the same potential flow theory as its basis as the previous methods, but is also combined with a modified Newtonian flow model. The Newtonian flow model is for use in acquiring data at hypersonic speeds, and therefore is not applicable to atmospheric turbulence research. A slightly different form of the potential flow solution that used previously is given in Equation 42.

$$p_i = q_c\left[\cos^2\left(\theta_i\right) + \varepsilon \sin^2\left(\theta_i\right)\right] + P_\infty \tag{42}$$

The ε term relates to a calibration parameter that was used to blend the potential flow and Newtonian flow solutions together. It does not therefore come into play in atmospheric turbulence research. The subscript i is used here to denote a particular port. As the ports are considered as a triple, the port designations within the triple are i, j, and k. The θ_i term refers to the incidence angle between the surface normal at the i'th port and the velocity vector. This incidence angle is related to the local, or effective, angle of attack, α_e, and angle of sideslip, β_e as shown in Equation 43.

$$\begin{aligned}\cos\left(\theta_i\right) = &\cos\left(\alpha_e\right)\cos\left(\beta_e\right)\cos\left(\lambda_i\right) \\ &+ \sin\left(\beta_e\right)\sin\left(\phi_i\right)\sin\left(\lambda_i\right) \\ &+ \sin\left(\alpha_e\right)\cos\left(\beta_e\right)\cos\left(\phi_i\right)\sin\left(\lambda_i\right)\end{aligned} \tag{43}$$

Equation 43 introduces two new measurement terms, the cone angle, λ, and the clock angle, ϕ. The cone angle is the angle between the normal to the surface and the longitudinal axis of the sensing head. This angle can be seen in the side view of the hemispherical head in figure 6. The clock angle is the angle formed by moving clockwise around the axis of symmetry while looking aft down the sensing head, and starting at the bottom of the probe head. Therefore position 1 in figure 5 is 0°, position 2 is 90°, position 3 is 180°, and position 4 is 270°. Position 0 and 5 are also 0°.

From Equations 42 and 43, it is therefore possible to determine the velocity vector of the probe head from the pressures at known locations, defined in terms of their clock and cone angles, on the surface of a hemispherical sensing head. This method does require that the local angles of attack and local angles of sideslip be related by calibrations to the true free stream angles. The strength of the FADS method, however, is that with these calibrations, a hemispherical sensing head is not required to determine the velocity vector. Any blunt nose of an aircraft that approximates a hemispherical head can be used if an accurate calibration is achieved.

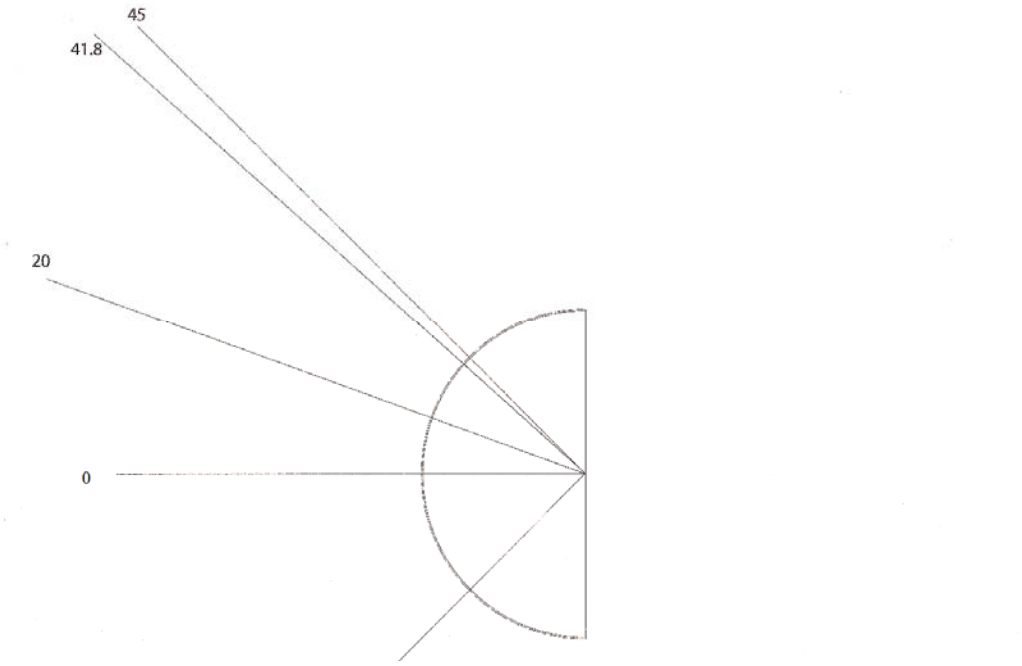

Figure 6. Side view of hemispherical sensing head with cone angles shown.

CHAPTER 3: BENCH TEST OF PROBE HEADS

3.1 Bench Test Overview

In order to evaluate the different methods of calculating air data described in Chapter 2, a series of bench tests was performed on three different hemispherical heads. Each hemispherical head had different pressure port layouts: a 45° head, a 41.8° head and a FADS port arrangement. The port arrangements are shown in figures 4 through 6. As can be seen from the figures, all heads have a cruciform arrangement of pressure reporting holes. Two hemispherical heads have four outer ports located 45° and 41.8° back from a center port on the vertical and horizontal meridians. The FADS layout incorporates four pressure ports located 20° from the center port and an additional pressure port located 45° from the center port on the vertical meridian. All model hemispherical heads were made of three inch diameter polystyrene spheres cut in half. The objective was to obtain pressure data from the three different heads at varying angles of attack and sideslip. This data would then allow comparison between the different methods of air data calculation.

3.2 Equipment

The equipment used in bench testing the probe heads was a wind generating device, three representative models of probe heads instrumented with miniature Kulite pressure transducers, a digital level, a National Instruments PXI data collection device, and a desktop computer running LabView data collection software [21]. The entire test set up is shown in figure 7, except the desktop computer.

Figure 7. Bench test set up, showing probe head, wind generator and PXI device.

The wind generator was constructed of cardboard boxes and a three speed box fan. The wind generator was an open loop design with a fan to push air down to the testing section. It incorporated a settling chamber with a cardboard grid to straighten the airflow and a contraction section to increase flow velocity. Figure 8 shows an interior view of the wind generator showing the settling chamber and fan. Only the maximum speed setting of the fan produced enough airflow to be useful in testing. The probe heads were placed inside the testing section, mounted atop a camera tripod, allowing both pitch and yaw positioning of the probe.

A close up of a probe head is shown in figure 9. All three heads consisted of two and a half inch PVC pipe with a three inch diameter polystyrene hemisphere on one end. The hemispherical sections of the probe head had port locations designed to replicate the three probe designs. One had a 45° separation between center and outer ports, one a 41.8° separation, and one a FADS port arrangement, with four ports located 20° off the center and one 45° port. A side view of the port degree locations are shown in figure 6. The 45° and 41.8° probe heads feature a cruciform layout of four ports around a center port, as shown in figure 4. The FADS design additionally incorporates an additional port lower down on the vertical meridian of the probe head, as shown in figure 5.

Each of the ports was connected to a miniature pressure transducer via flexible tubing. The pressure transducers used were Kulite model XT-140. Specification sheets for this transducer are supplied in the appendices. The transducers were capable of measuring 0 to 15 psi absolute pressure values. Transducer output is a voltage change as the pressure over a miniature silicon diaphragm changes. This voltage change data was sent to a National Instruments PXI data collection device which in turn was connected to a desktop computer

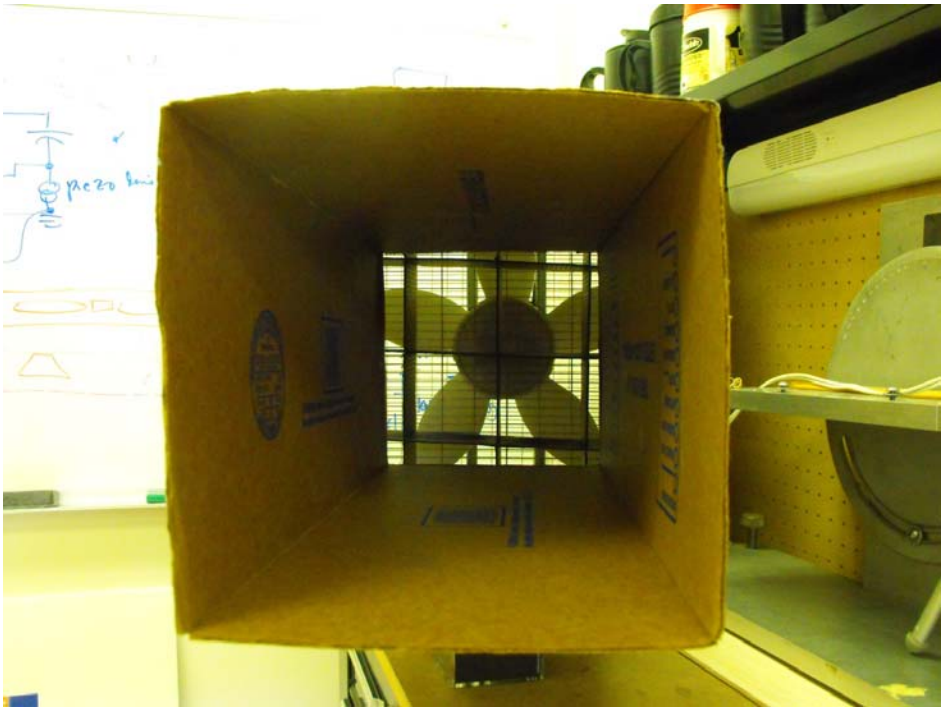

Figure 8. Interior of wind generator, showing settling chamber and fan.

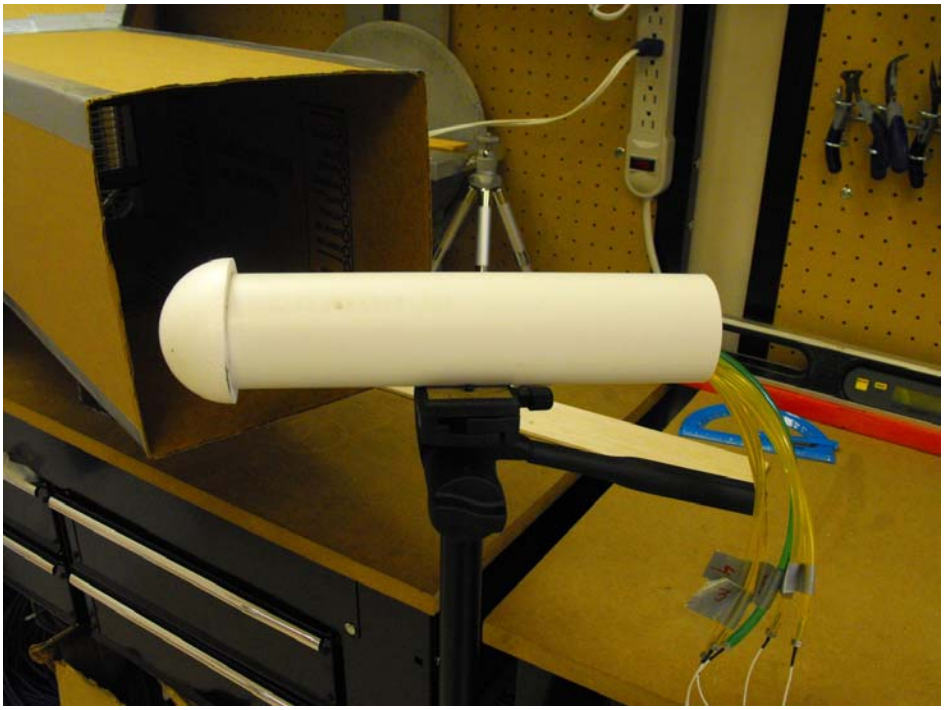

Figure 9. Close up of a probe head and connected pressure lines, mounted on tripod.

running LabView software. The pressure transducers were calibrated in the lab against a Digital Pressure Sensing (DPS) reference transducer, as described below.

Voltage changes and the associated calibrated pressure differences from the pressure transducers were displayed on a LabView display using custom designed software by Professor John Muratore of the UTSI Aviation Systems Department. In addition to converting voltages to pressures for all the transducers and simultaneously displaying all pressures on one graph, the custom designed LabView software enabled recording and exporting of the data for use in a Microsoft Excel spreadsheet for post processing. To facilitate post processing, two additional manipulations of the data were built into LabView software program. First, a zeroing feature was implemented to display pressure difference values from an operator determined point. Second, the software included a counter to display a user defined mark point in the exported data. The zeroing mechanism was necessary to mitigate instrument errors exacerbated by collecting data at the extremes of the pressure transducers measurement resolutions. The second mechanism facilitated the accurate integration of hand and computer recorded data.

3.3 Pressure Transducer Reference Calibration

The calibration test of the Kulite pressure transducers was conducted in the UTSI Aviation Systems Program Flight Systems Laboratory. The Kulite pressure transducers were connected to the National Instruments PXI device and their output was recorded by the LabView software.

The calibration procedure was as follows.

1. Connect static pressure line from DPS to pressure transducer.

2. Select absolute pounds per square inch (psia) values on DPS readout.

3. Obtain local static pressure from the DPS and transducer and record both.

4. Activate DPS vacuum pump to obtain a pressure drop on both the DPS display and the transducer.

5. By using the DPS valve control, allow the DPS and transducer to reach a steady pressure value and record.

6. Repeat steps 4 and 5 down to 7 psia.

7. Test each transducer as above.

3.4 Probe Head Test

Testing took place in the UTSI Aviation Systems Program Flight Systems Laboratory. A wind generator was used to provide air flow over the hemispherical probe heads. Specific airspeeds were not available with this device. It was assumed that the airflow inside the test section was uniform, although this was not verified. Angle of attack was measured using a digital level placed along the length of the probe body. This device had a zeroing capability, allowing it to determine an arbitrary level plane and an angle of deviation from this plane. Angle of sideslip was determined by measuring the angle of deflection against a scale at the bottom of the wind tunnel. All angles were recorded by hand. Measurement accuracies for measurement of angle of attack and angle of sideslip are not available. In the following chapter, therefore, the positions of the probe are listed as measured values as opposed to exact values. Three hemispherical probes with different pressure port layouts were used. One probe had a 45° port separation; one had a

41.8° port separation; one had a FADS port arrangement. All three probes were rotated independently through a range of approximately ±30° angle of attack and angle of sideslip.

The probe head test procedure was as follows.

1. Position probe in wind generator at zero degrees angle of attack and sideslip.

2. Turn on wind tunnel and data acquisition software.

3. Allow system to acquire pressure data from the pressure transducers, and then use the software zeroing of the data to obtain pressure difference values.

4. Rotate probe through a ±30° range of angle of attack and angle of sideslip in approximately 5° intervals.

5. Activate counter in data to mark the point when probe is at desired test angle.

During the testing, the pressure transducer output graph would periodically display an excessive amount of drift from the transducers in a seemingly random manner. If this occurred, the test data was thrown out and the test was restarted. The cause of this excessive drift could not be determined.

CHAPTER 4: RESULTS AND DISCUSSION

4.1 Calculated vs. Measured Pressures

A more detailed set of figures showing the individual results for calculated vs. measured angles, and percent errors for all methods tested, is shown in Appendix B: Details of Bench Test Results. This section also displays the individual R^2 values that are summarized later in this section. A quick look through Appendix B will show that many of the methods display an overall inverse relationship between calculated and measured flow angles. The values of the data points appear to be unaffected, but have the opposite sign from what is expected. It is unknown why exactly this occurs, but it may be caused by the method used to compensate for measuring only a small fraction of the pressure transducers measurement range. In order to do this, a pressure difference was recorded and used in calculations. For the purposes of comparison and clarity, all flow angles have been assumed to follow an overall direct relationship between calculated and measured values. The original values are presented in Appendix B.

It should be noted that for all the results in this section, the goal of the bench testing was to compare the techniques used to determine if one particular method displayed an advantage to its use over another. Therefore the absolute pressure values themselves are not as critical as the comparison of methods used to obtain the values. There are many sources of error that occur in this testing and are discussed in Chapter 5. These error sources alter the accuracy of the calculated vs. measured pressures, but since the methods are all exposed to the error sources equally a valid comparison of the methods used may still be made.

The first plot of calculated pressures vs. measured pressures, shown in figure 10, is the 45° probe head rotated through ±30° of angle of attack. An ideal one to one linear relationship between the calculated and measured angles of attack has been overlaid on the graph to provide a visual of how the test values approximate an exact relationship. The test values over the ±10° measured angle of attack approximate an exact one to one relationship. Outside this band, however, the calculated angles of attack demonstrate a flattening and even a reversal from a direct relationship to an inverse one at measured angles of attack greater than -20°. High Resolution and FADS methods are in exact agreement with each other.

The overall highest calculated value is achieved with the FADS method and is 26° angle of attack and corresponds to a measured value of -21.5° measured angle of attack. The overall lowest calculated value is -26° angle of attack, is achieved by the High Resolution method, and corresponds to a measured angle of attack of -21.5°. These maximum and minimum values are mirror images of each other, and this holds true for all the High Resolution and FADS results in this graph. The maximum High Resolution calculated angle of attack is shared among three points at 19.4° as the results level out and the measured angle of attack approaches its maximum of 28°. The minimum High Resolution angle of attack is the overall minimum reported above. The maximum NCAR calculated angle of attack is 15.5°, corresponding to the measured angle of attack maximum of 28°. The minimum NCAR calculated angle of attack is 19°, corresponding to a measured angle of attack of -21.5°. The maximum Ekman calculated angle of attack is 22.4°, corresponding to a measured angle of attack of -21.5°. The minimum Ekman calculated angle of attack is -25.5°, corresponding to a measured angle of attack of 28°. The maximum FADS calculated angle of attack is the overall maximum reported above. The minimum FADS calculated angle of attack shared among three points at -19.4° as the results level out and the

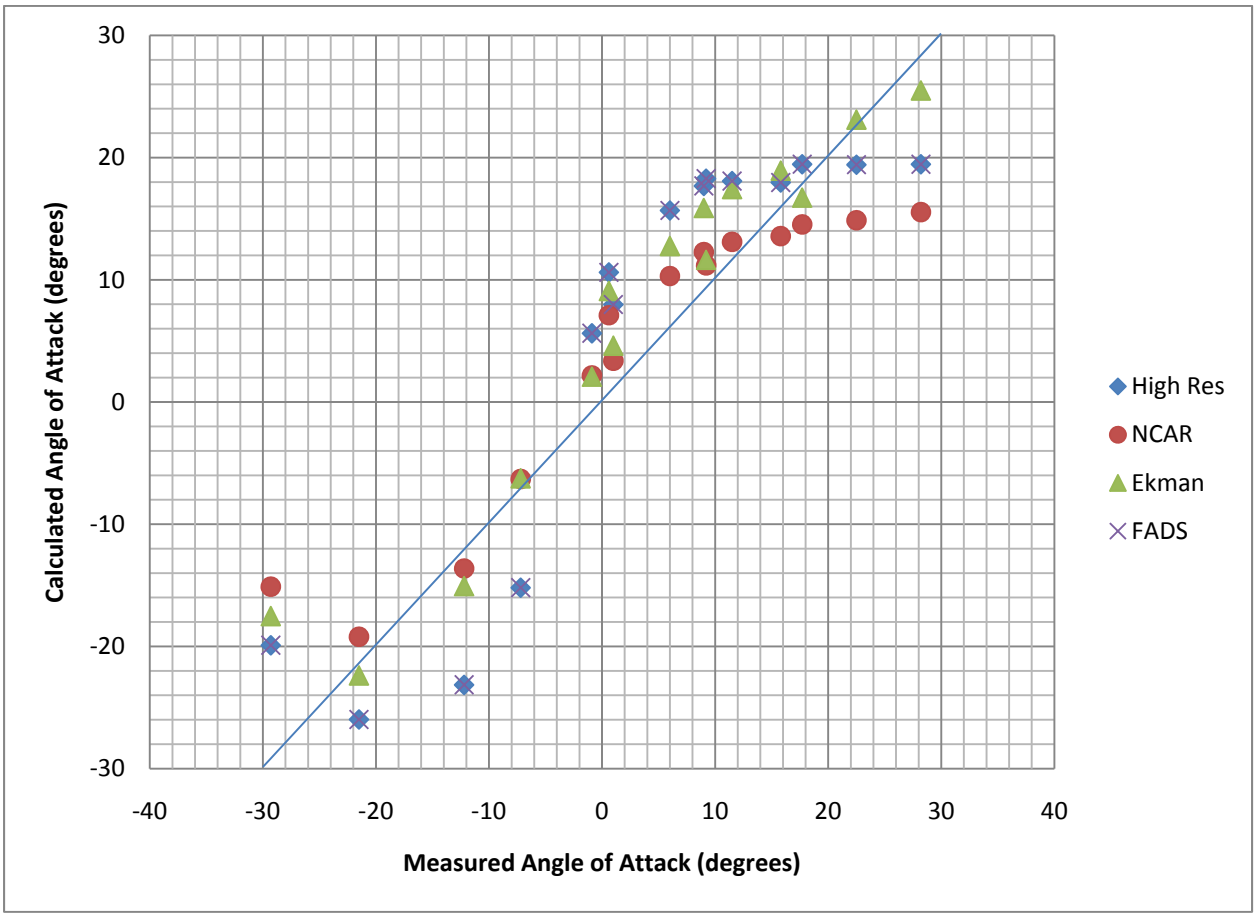

Figure 10. Calculated Angle of Attack vs. Measured Angle of Attack, 45° Head.

measured angle of attack approaches its maximum of 28°. As previously mentioned, this is the inverse of the maximum High Resolution method data points.

Figure 11 shows the results for the 45° probe rotated through ±30° angle of sideslip. This test was performed in two parts, first the positive values of measured angle of sideslip and secondly the negative values of measured angle of sideslip. This may explain the offset between the positive and negative calculated angles of sideslip. As in figure 10, an ideal one to one relationship line has been overlaid on the graph. Overall, the calculated and measured angles of sideslip display a similar slope to the ideal line throughout the ±30° measurement range. Over the ±10° measured angle of sideslip range, the Ekman, High Resolution and FADS methods show a close approximation of a one to one relationship. Outside of this ±10° measurement range, the slope of the previous methods flattens out. High Resolution and FADS methods are again in exact agreement with each other.

The overall maximum calculated angle of sideslip is an Ekman data point of 43.2°, found at a measured angle of sideslip of 0°. The overall minimum calculated angle of sideslip is a NCAR data point of -37.3°, corresponding to a measured angle of sideslip of 5°. The maximum High Resolution and FADS calculated angle of sideslip is 26.7°, at a measured angle of sideslip of 0°. The minimum High Resolution and FADS calculated angle of sideslip is -26.8°, corresponding to a measured angle of sideslip of 0°. The maximum NCAR calculated angle of sideslip is 29.8° at 0° measured. The minimum NCAR calculated angle of attack is the previously mentioned overall minimum. The Ekman maximum calculated angle of sideslip is the previously mentioned overall maximum. The Ekman minimum calculated angle of attack is -32.5°, corresponding to a measured angle of 0°.

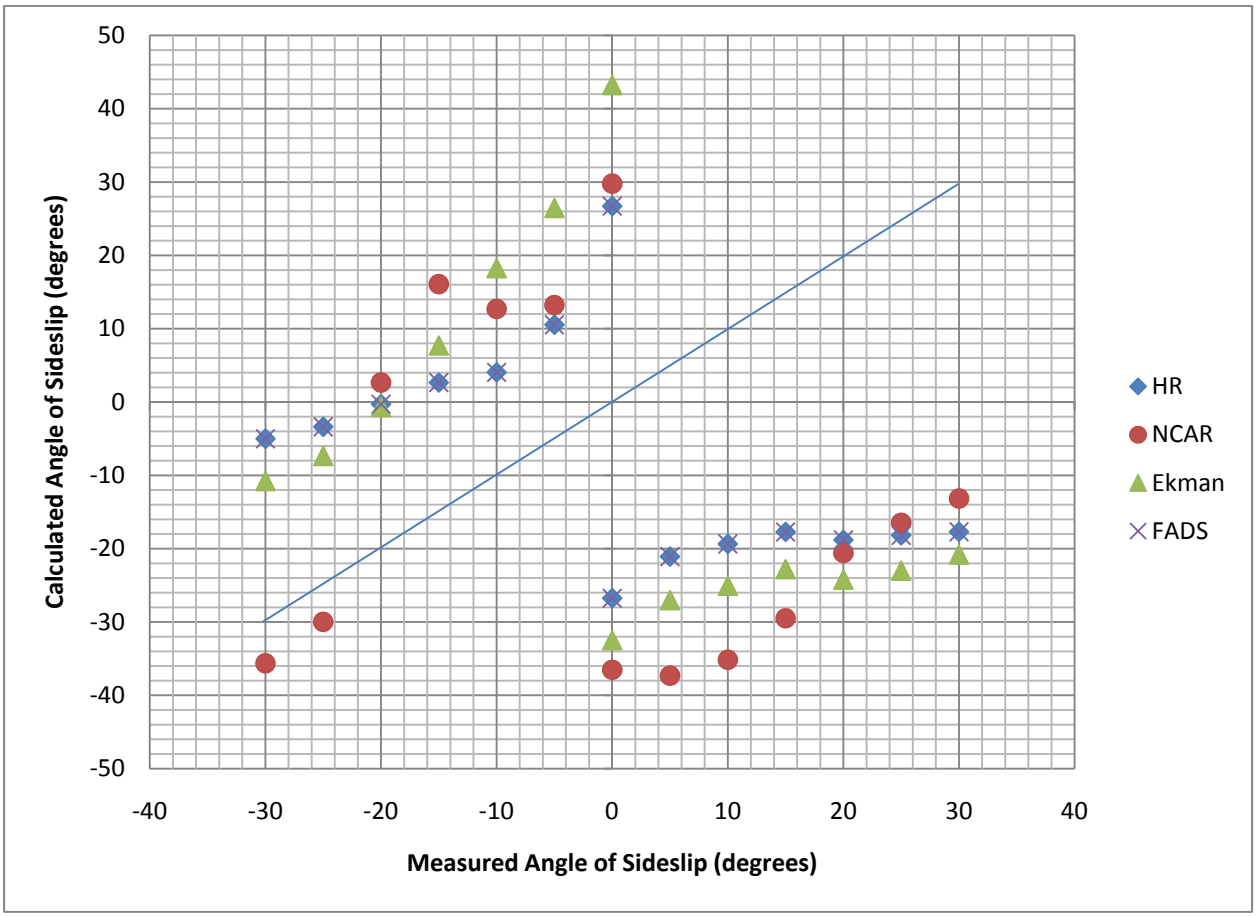

Figure 11. Calculated Angle of Sideslip vs. Measured Angle of Sideslip, 45° Head.

Figure 12 is a plot of the data obtained from the 41.8° probe rotated through approximately ±40° angle of attack. This test was performed in two parts, first the positive values of measured angle of sideslip and secondly the negative values of measured angle of sideslip. This may explain the offset between the positive and negative calculated angles of sideslip. As in figure 10, an ideal one to one relationship line has been overlaid on the graph. The positive measured angles of attack do not display an accurate relationship with the calculated values over the 0 to 15 degree range, but after this the points follow a similar slope. For the negative values of measured angle of attack, the calculated values display a good approximation of a direct relationship for the 0 to -10 degree range. Outside this range, the values of all methods flatten out. High Resolution and FADS methods are again in exact agreement with each other.

The overall maximum calculated angle of attack is obtained with the FADS and High Resolution methods at 25.5°, corresponding to a measured angle of attack of 40.6°. The overall minimum calculated angle of attack is also obtained with the FADS and High Resolution methods of -36.7°, corresponding to a measured angle of attack of 9.7°. The maximum NCAR calculated angle of attack is 18.4°, found at a measured angle of attack of 0.5°. The minimum NCAR calculated angle of attack is -21.6°, corresponding to a measured angle of attack of 5.2°. The maximum Ekman calculated angle of attack is 17.1°, at a measured angle of attack of 0.5°. The minimum Ekman calculated angle of attack is -19.5°, found at a measured angle of attack of 5.2°.

Figure 13 is a plot of the data obtained from the 41.8° probe rotated through ±30° angle of sideslip. This test was performed in two parts, first the positive values of measured angle of sideslip and secondly the negative values of measured angle of sideslip. As in figure 10, an ideal

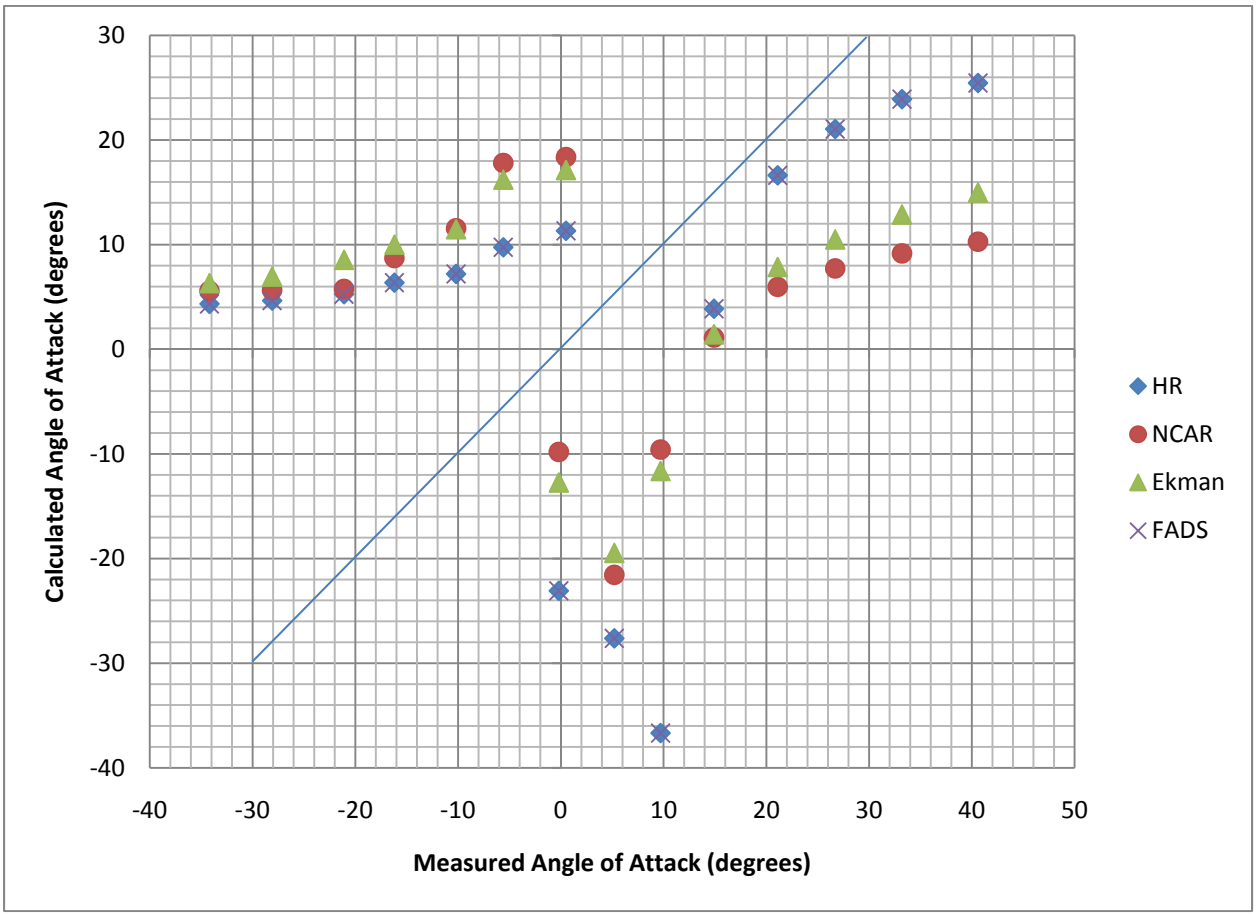

Figure 12. Calculated Angle of Attack vs. Measured Angle of Attack, 41.8° Head.

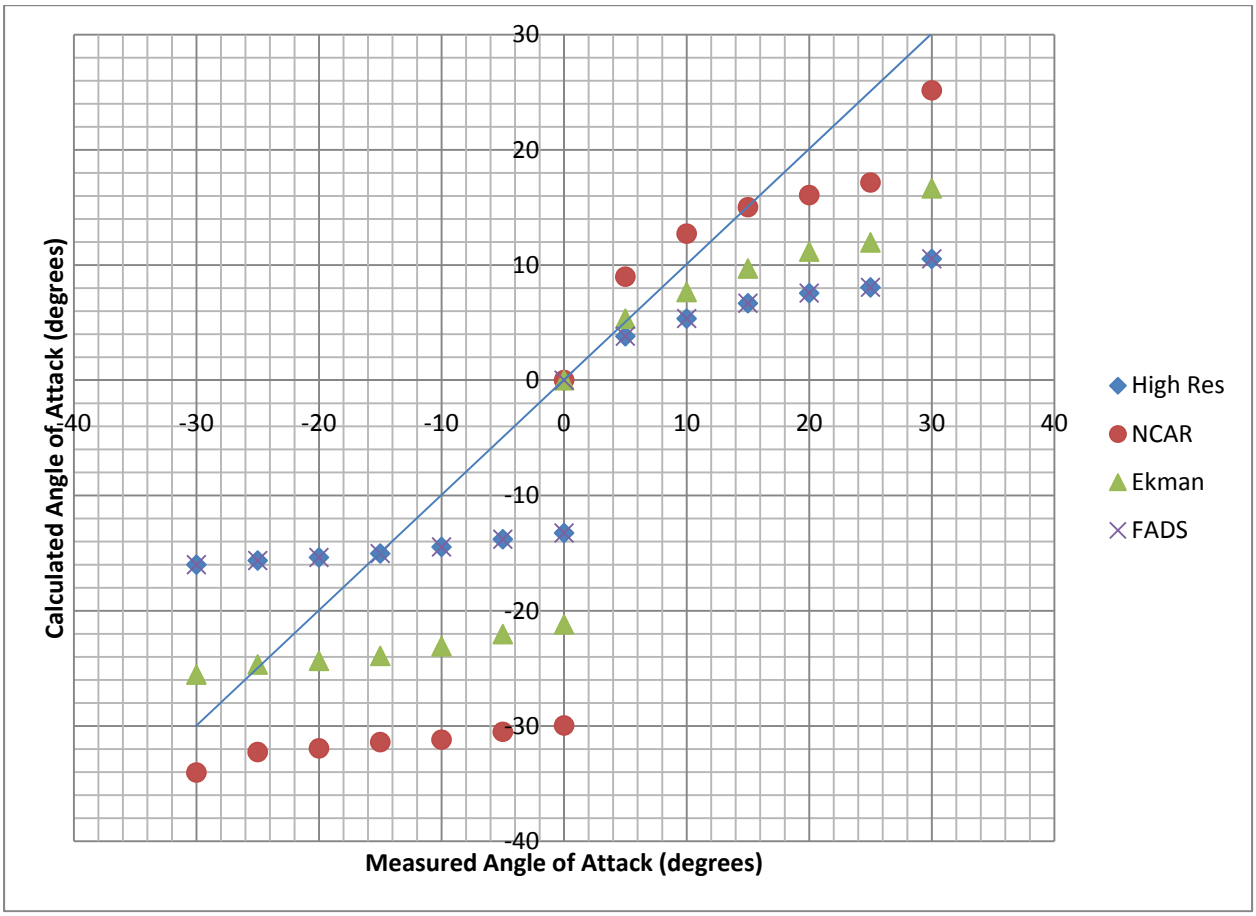

Figure 13. Calculated Angle of Sideslip vs. Measured Angle of Sideslip, 41.8° Head.

one to one relationship line has been overlaid on the graph. The High Resolution and FADS data display an exact relationship between data points. Somewhat unusually for this series of tests, the data all pass through the origin point. The positive calculated angles of sideslip show a strong agreement with the measured angle of sideslip up to 10°, after which the points begin to flatten out, as has been seen previously. Negative angles of sideslip display a very flat curve with an almost constant offset between the values throughout the range of measured angle of sideslip. This has not been observed previously in this investigation. The overall trend for all data follows a direct relationship between calculated and measured angles of sideslip.

The overall calculated maximum of 25.2° is achieved with the NCAR method at the measured angle of sideslip of 30°. The overall minimum calculated angle of sideslip is also a NCAR point of -34.0° at a measured angle of sideslip of -30°. The maximum Ekman calculated angle of sideslip is 16.7° at 30° measured angle of sideslip. The minimum Ekman calculated angle of sideslip is -25.5° at -30° measured angle of sideslip. The maximum FADS and High Resolution calculated angle of sideslip is 10.5° at a 30° measured angle of sideslip. The minimum FADS and High Resolution calculated angle of sideslip is -16.0° at a -30° measured angle of sideslip.

Figure 14 is the plot of measured angle of attack vs. calculated angle of attack for the FADS probe head. This test was performed in two parts, first the positive values of measured angle of attack and secondly the negative values of measured angle of attack. An ideal one to one relationship curve between the two variables cannot be included for the positive measured angle of attack data, as can be seen. At all data points, the calculated angle of attack is negative. For the negative measured angles of attack, the Ekman method shows a good agreement between the ideal line and the obtained data points. NCAR, High Resolution and FADS data all display a

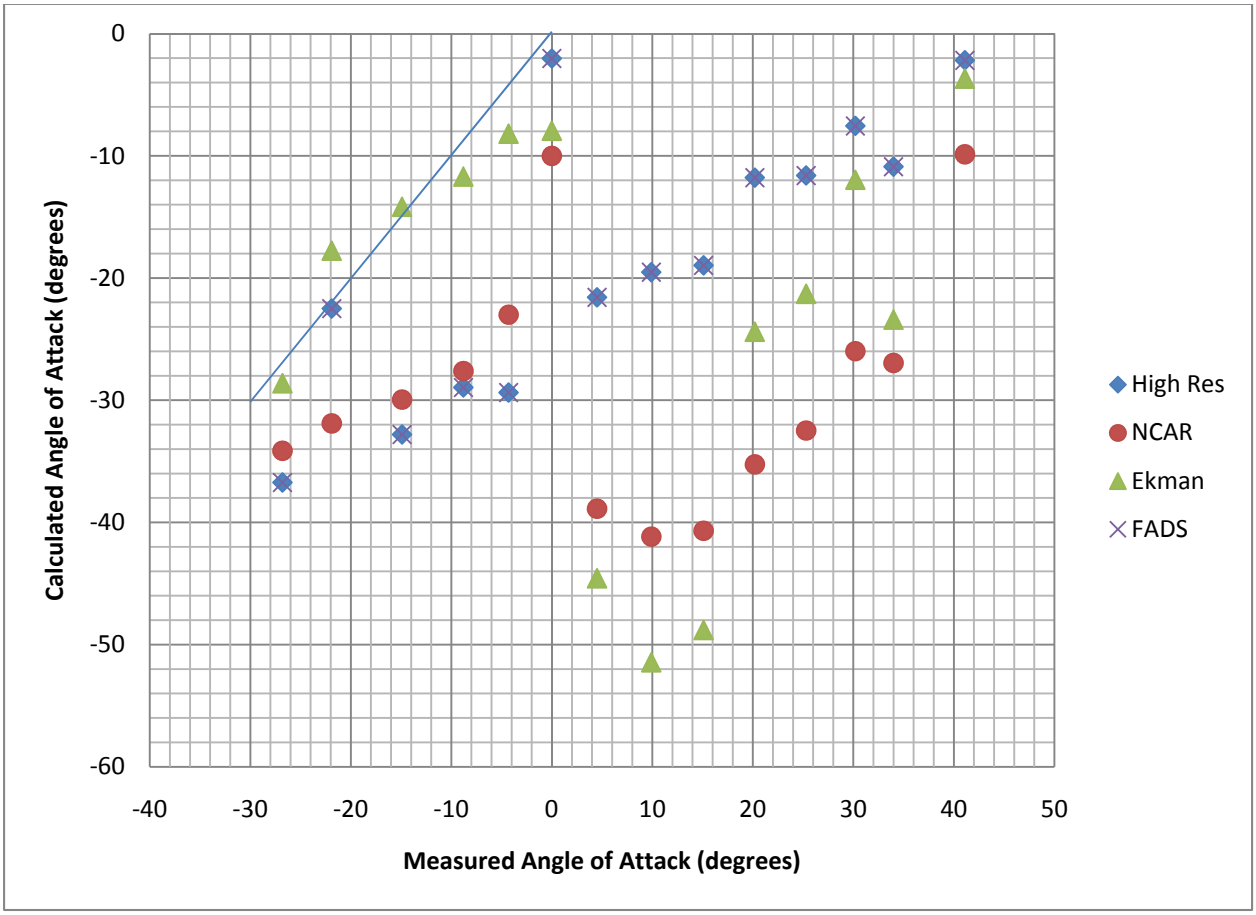

Figure 14. Calculated Angle of Attack vs. Measured Angle of Attack, FADS Head.

large offset and a shallow slope compared to the one to one relationship curve. For the positive angles of attack, all data points display an overall direct relationship between measured and calculated variables, but there is a lot of scatter in the data. FADS and High Resolution data are again in exact agreement with each other.

The overall maximum calculated angle of attack is an FADS and High Resolution data point of -2.2°, found at 41.1° measured angle of attack. The overall minimum angle of attack is an Ekman data point of -51.4° and corresponds to a measured angle of attack of 9.9°. The FADS and High Resolution maximum calculated angle of attack is the overall maximum. The FADS and High Resolution minimum calculated angle of attack is -36.7°, at a measured angle of attack of -26.8°. The NCAR maximum calculated angle of attack is -10.0° and corresponds to a measured angle of attack of 0°. The NCAR minimum calculated angle of attack is -41.2° and is found at a measured angle of attack of 9.9°. The Ekman maximum calculated angle of attack is -3.7° at a measured angle of attack of 41.1°. The Ekman minimum calculated angle of attack is the overall minimum value.

Figure 15 is the plot of measured angle of sideslip vs. calculated angle of sideslip for the FADS probe head. This test was performed in two parts, first the positive values of measured angle of sideslip and secondly the negative values of measured angle of sideslip. As in figure 10, an ideal one to one relationship line has been overlaid on the graph. For the positive measured angles of sideslip, there is good agreement between the measured and calculated variables, especially over the 0 to 10 degree range. For negative measured angles of sideslip there is an almost constant calculated value and no agreement with the ideal one to one relationship. The High Resolution and FADS methods agree exactly in this data set.

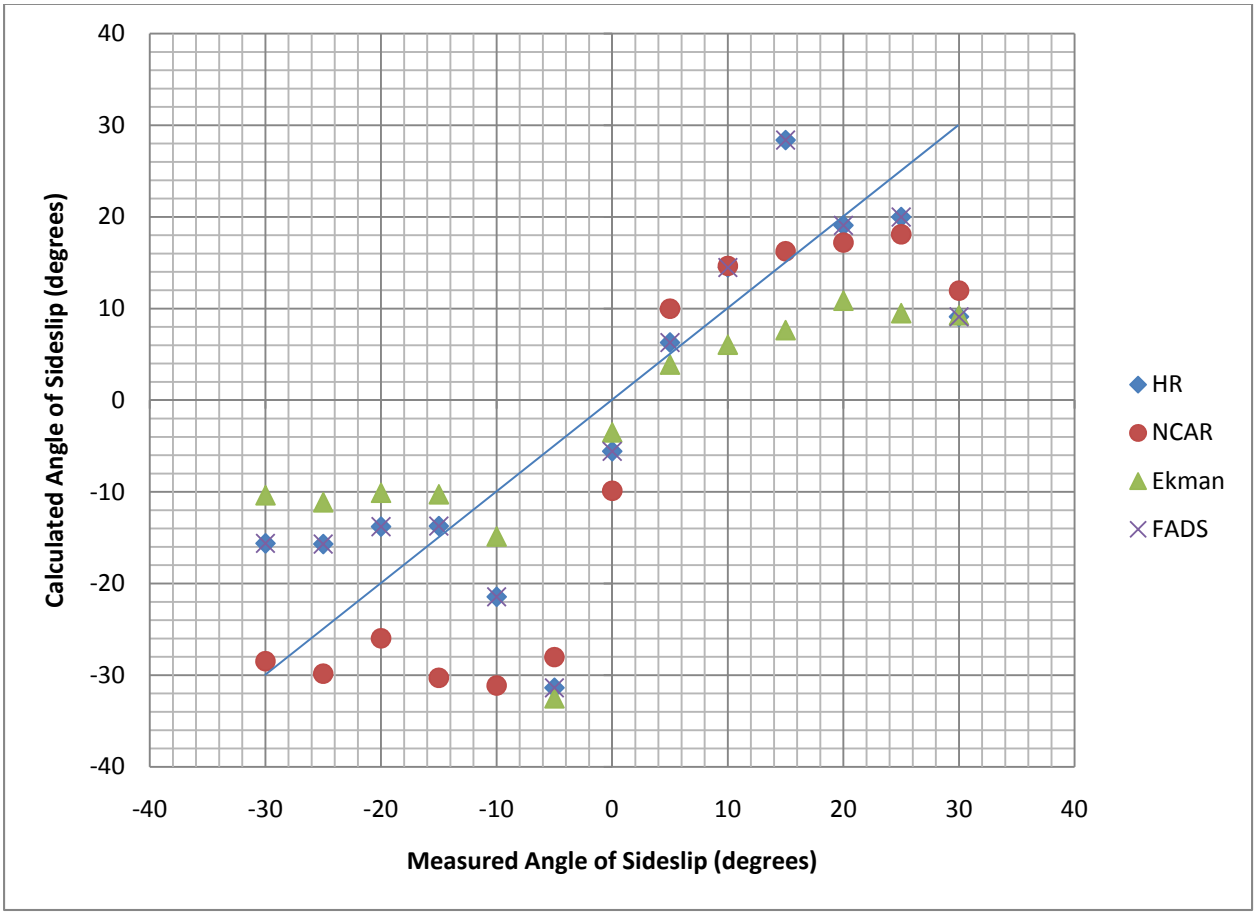

Figure 15. Calculated angle of sideslip vs. measured angle of sideslip, FADS head.

The overall maximum calculated angle of sideslip is 28.4°, achieved using the FADS and High Resolution methods at a measured sideslip angle of 15°. The overall minimum calculated angle of sideslip is -32.5°, achieved using the Ekman method at a measured angle of sideslip of -5°. The minimum calculated High Resolution and FADS angle of sideslip is -31.4°, occurring at a measured value of -5°. The maximum calculated Ekman angle of sideslip is 10.9° at a measured value of 20°. The maximum NCAR calculated angle of sideslip is 18.1°, occurring at 25° measured angle of sideslip. The minimum NCAR calculated angle of sideslip is -31.1°, at a measured angle of sideslip of -10°.

4.2 Variability of FADS Port Combinations

Figure 16 shows the result of using different FADS port 'triples' combinations to calculate the angle of attack. All port combinations are in close agreement until after the 15° measured angle of attack point. At measured angles of attack values of -0.2°, 4.5°, 9.9°, 15.1°, and 20.2°, the variation in calculated angles of attack are 1.9°, 4.0°, 2.0°, 3.3°, and 15.4°, respectively. Therefore, the average variation in calculated angles of attack between the four combinations of pressure ports is 2.8°, up to measured angles of attack of 15.4°. After this 15.4° measured angle of attack point, the variation in calculated angle of attack increases rapidly with measured angle of attack. From this data, the FADS method appears to be effective until approximately 15° angle of attack. The negative measured angles of attack data in figure 16 also display an offset that increases as magnitude of angle of attack increases, but with no obvious agreement between the port combinations. Three of the port combinations display some agreement over the range of

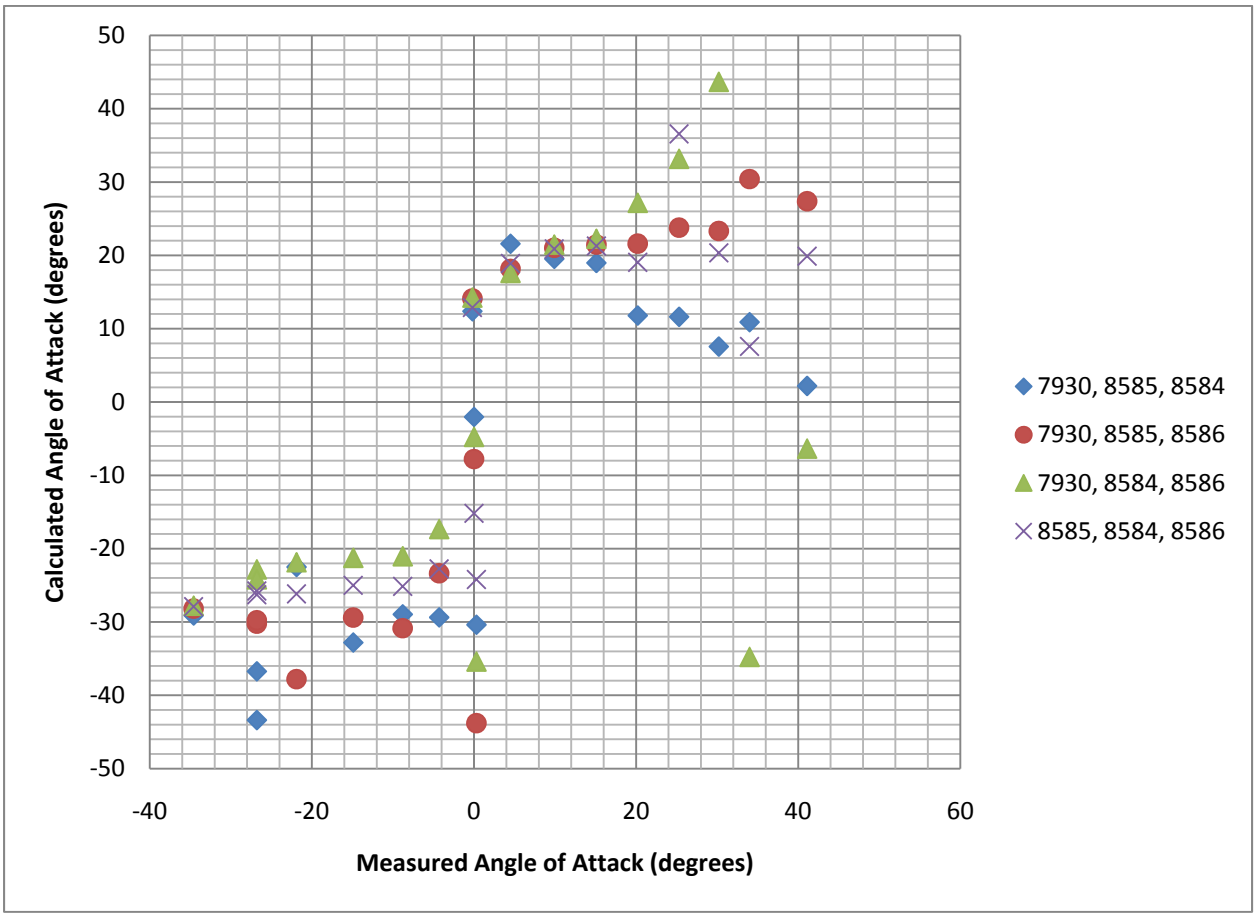

Figure 16. Calculated angle of attack vs. measured angle of attack, FADS head, all ‘triples.’

-4.3° to -34.6° measured angle of attack. Within this range, the variation between configurations ranges from 1.2° to 15.9° calculated angle of attack.

4.3 Comparison of R^2 Values

Table 2 shows the R^2 values for all tests on all three probes and using all four methods. R^2 values can be used to test for strength of relationship between two variables. As the R^2 value approaches 1.0, the two variables exhibit a strong correlation between each other. In other words, as one variable changes, so does the other. A strong correlation between the measured and calculated variables would indicate that the method tested is sensitive to changes in angles of attack and sideslip, even if the accuracy of the calculated variable is low. Graphs showing the R^2 values for each measured angle vs. calculated angle data set are found in Appendix B.

In the 45° probe head pitch test, the Ekman method gave the highest R^2 value of 0.9288, which shows a strong correlation between the calculated and measured angle of attack. All methods in this test had a relatively high R^2 value, with the High Resolution and FADS methods having the lowest R^2 of 0.8140. In the positive measured angle of sideslip tests on the 45° probe, the highest R^2 value was 0.8151 and was achieved using the Ekman method. The lowest R^2 value for the positive angle of sideslip test on this probe was 0.4395, using the NCAR method. For the negative angle of sideslip test on the 45° probe, the correlation between calculated and measured angle of attack was very high for all methods but NCAR. Highest R^2 was 0.9667 for the Ekman method to a low of 0.5211 for the NCAR method.

Table 2: R^2 Values, Averages and Standard Deviations

Method	45° α	45° β (+)	45° β (-)	41.8° α (+)	41.8° α (-)	41.8° β (+)	41.8° β (-)	FADS α (+)	FADS α (-)	FADS β (+)	FADS β (-)	Method Average	Method Std. Deviation
High Resolution	0.8140	0.7207	0.9533	0.8150	0.9010	0.9275	0.9742	0.9053	0.5107	0.2020	0.0937	0.7107	0.3083
NCAR	0.8871	0.4395	0.5211	0.7592	0.8509	0.8951	0.9181	0.8963	0.5482	0.7912	0.7466	0.7503	0.1706
Ekman	0.9288	0.8151	0.9667	0.8611	0.9194	0.9423	0.9731	0.8283	0.8071	0.0708	0.8066	0.8108	0.2538
FADS	0.8140	0.7207	0.9533	0.8150	0.9010	0.9275	0.9742	0.9053	0.5107	0.2020	0.0937	0.7107	0.3083
Test Average	0.8610	0.6740	0.8486	0.8126	0.8931	0.9231	0.9599	0.8838	0.5942	0.3165	0.4352	0.7456	0.2602
Test Std. Deviation	0.0568	0.1625	0.2184	0.0417	0.0294	0.0199	0.0279	0.0372	0.1430	0.3224	0.3950	0.0473	

For the positive measured angle of attack test on the 41.8° probe, the Ekman method again had the highest R^2 value, 0.8611 in this case. The NCAR method again had the lowest correlation, with an R^2 value of 0.7592. For the negative measured angle of attack on the 41.8° probe all methods displayed a strong degree of correlation. The calculated and measured angle of attack R^2 range was 0.9194 to 0.8509, for Ekman and NCAR methods, respectively. There was very little spread in the R^2 results for the positive measured angle of sideslip for the 41.8° probe head: 0.9423 to 0.8951 for Ekman and NCAR methods, respectively. The negative measured angle of sideslip tests also even closer agreement between R^2 values. The minimum R^2 value was 0.9181 for the NCAR method to 0.9742 for the High Resolution and FADS methods.

The positive measured angle of attack test with the FADS probe R^2 values ranged from 0.9053 for High Resolution and FADS methods to 0.8283 for the Ekman method. The negative measured angle of attack test with the FADS probe R^2 results ranged from 0.8071 for the Ekman method to 0.5107 for the High Resolution and FADS methods. The positive measured angle of sideslip tests on the FADS probe show the greatest variation in R^2 values, from 0.7912 for the NCAR method to 0.0708 for the Ekman method. This is the only time the NCAR method has the highest R^2 value. The negative measured angle of sideslip tests on the FADS probe head also show a wide range of results, from 0.8066 for the Ekman method to 0.0937 for the High Resolution and FADS methods.

The summary statistics in Table 2 show the Ekman method to have the highest overall mean R^2 value of 0.8108. The Ekman method had the highest R^2 value on eight of the eleven test runs. The highest overall R^2 value was 0.9742 using the High Resolution and FADS methods. The test run with the highest average R^2 value was the negative angle of sideslip test of the 41.8° probe, with an R^2 of 0.9599. The lowest standard deviation among the runs was

0.1706 for the NCAR method. The lowest standard deviation among the test runs was 0.0199 for the 41.8° probe head positive angle of sideslip test.

A single factor analysis of variance test can provide information as to whether there is a significant difference between three or more groups of data. The null hypothesis in this test is that all methods have the same average strength of correlation between calculated and measured values. Differences in mean R^2 values between methods are therefore a result of normal variation and not a significantly stronger correlation of one particular method.

Table 3 shows the results of a one way, single factor ANOVA test on the mean R^2 values of the four different methods. The P-value of 79% states the probability of random sampling causing the average values to display the range observed in the testing. A P-value of greater than 5% is not considered significant. Furthermore, the F value of 0.3475, which is a ratio of the between group to within group variation, is well below the critical threshold of 2.8387. The null hypothesis is not rejected by the ANOVA test and therefore there is no particular method which can be determined to be most sensitive to changes in pitch or yaw from these tests.

Table 3: ANOVA Results

Anova: Single Factor

SUMMARY

Groups	*Count*	*Sum*	*Average*	*Variance*
HR	11.0000	7.8174	0.7107	0.0950
NCAR	11.0000	8.2533	0.7503	0.0291
Ekman	11.0000	8.9193	0.8108	0.0644
FADS	11.0000	7.8174	0.7107	0.0950

ANOVA

Source of Variation	*SS*	*df*	*MS*	*F*	*P-value*	*F crit*
Between Groups	0.0739	3.0000	0.0246	0.3475	0.7912	2.8387
Within Groups	2.8361	40.0000	0.0709			
Total	2.9100	43.0000				

CHAPTER 5: CONCLUSIONS

The vector equation used to determine the atmospheric velocity vectors is an addition of flow vector and probe vector, as shown in Equation 1. As there was no in flight testing performed, the probe vector segment of Equation 1 is therefore zero. Due to limitations in the homemade wind generator built to replicate the flow vector, the airspeed of the flow was not measureable, and subsequently the flow vector magnitude component was not available. What has been tested is the direction component of the flow vector, with each of the methods described in Chapter 2 used, with the exception of the Rosemount Engineering Low Resolution method. The Low Resolution method was not tested due to its requirement of direct measurement of a separate static pressure source. The other factor that has been investigated is the measured angular range over which the calculated values are in agreement.

According to Beswick [8], the accuracy required of the velocity vector is 0.5 to 1.0 m/s for meteorological research. Lenschow [9] has stricter requirements of 1 or 2 cm/s resolution for the velocity components. In order to achieve this level of resolution, the accuracy in flow angle measurement needs to be of the same order of magnitude. Therefore, an angular accuracy of between 0.1 to 1.0 degrees would be required. Armistead and Webb [11] reported an uncertainty in angle of attack of ±0.35° over and angle of attack range of 0° to 13°. Crawford and Dobosy [22] reported angle of attack and angle of sideslip accuracies of 0.3°. Wood *et al* [13] achieved a similar accuracy of 0.25° for angle of attack and angle of sideslip. Using an eighteen hole FADS system, Larson and Siemers [17] reported an angle of attack accuracy of ±0.5° over a range of 18° and an angle of sideslip accuracy of ±0.75°. Using the six holes FADS system that the probe used in this investigation is based on, Whitmore *et al* [18] achieved and angle of attack accuracy of

±0.30° and an angle of sideslip accuracy of ±0.45° over an angle of attack range of -20° to 45° and an angle of sideslip range of ±20°. Unlike the other methods, Whitmore *et al* [18] report an increase in accuracy as speeds increase. Approaching the transonic region, the angle of attack accuracy increased to ±0.23° and the angle of sideslip accuracy increased to ±0.20°. All these methods achieve the accuracy requirements of both Beswick and Lenschow and therefore could be used for measurement of atmospheric turbulence. However, none of the results obtained through the current investigation's bench testing were accurate enough to be used for atmospheric turbulence measurement.

Overall, the best method with the strongest correlation between measured and calculated flow angles was the Ekman method, with a mean R^2 value of 0.8108 and a standard deviation of ±0.2538. The NCAR method had the next strongest statistical correlation with a mean R^2 of 0.7503 and a standard deviation of ±0.1706. The FADS and High Resolution methods had the weakest correlations between measured and calculated flow angles with mean R^2 values of 0.7107 and standard deviation of ±0.3803. Although the Ekman method performed best overall, none of the methods used achieved what would be a high level of correlation between the measured and flow angles. The relatively high standard deviations of all methods mean that it is impossible to say that any of the probe heads tested best on average. The ANOVA test results confirm that there is no statistically significant difference between the methods.

The lack of difference between the methods is an important conclusion, however. Perhaps more interesting is the exact agreement between the FADS and the High Resolution methods. Both the FADS and the High Resolution methods are the only methods that determine flow angles by exclusively using the pressures obtained from the flow head, or nosecone in the case of FADS. All the other methods either directly measure static pressure or estimate a value for it. The static

pressure value is then used in determining the flow angle calculation. As the FADS and High Resolution methods are based upon the same potential flow theory it is perhaps not surprising that they therefore obtain the same results, even if the mathematics used to obtain those results are executed differently. The similarity between methods may be viewed as a cross validation of the two methods. Previous tests have confirmed that the accuracies necessary for atmospheric turbulence measurement are obtainable with a hemispherical flow head sensor. Therefore, choice of the flow angle measurement method used in a particular application should not be determined by one method being perceived as inherently better than another, but rather by using the most convenient method for a particular probe-airframe system.

There were several major potential sources of error in the bench testing of the probe heads. The accuracy of both the measured and the calculated angles may be altered by errors, and the precision of both the measured and the calculated angles may be altered by errors. The accuracy of the variables demonstrates the closeness of the variable to the true value. The precision of the variable demonstrates the ability to reproduce the variable with the same result when tested under the same conditions.

The most easily identifiable source of error is the uncalibrated wind generator used to provide uniform air flow over the probe heads. If the flow of air inside the generator is not uniform and straight, then the local angle of pitch and yaw formed between the probe head and the flow field would not accurately depict the measured angle of attack or measured angle of sideslip. Furthermore, a turbulent flow within the generator tunnel may cause the flow field to change over time. This error may cause the precision of the measured angle of attack and measured angle of sideslip to be affected. It is possible that the error attributed to the wind generator may be measurement noise in the system. In addition to the wind generator induced

errors, the hand measured method of recording the angle of inclination of the probe head, in both pitch and yaw directions may cause the accuracy and precision of the measurement variables to suffer.

As a result of these uncertainties in the measurements it is impossible to determine if one method offers an advantage over another. This conclusion agrees with the statistical analysis, but for a different reason. If the errors in measurement are causing the measurement values to be incorrect then the statistical analysis of the results may also be incorrect, even if all methods were tested under the same conditions. Further, more rigorous testing may solve this problem.

There are several improvements to the bench test set up which should be implemented if future tests of this nature are conducted. Primarily, the wind generator should be more like a wind tunnel, with tests such as placement of pressure transducers at different locations in the tunnel to determine if the flow is truly uniform across the test section performed before testing on the probe heads is undertaken. Secondly, the velocity of wind generated should be measureable to allow calculation of flow velocity components. Third, the method of measuring the inclination of the probe head should be improved and a level of accuracy in this measurement determined. Additionally, the pressure transducers used should be of a much smaller measurement range that is more applicable to the testing performed.

List of References

1 Crawford, Timothy L. and McMillen, Robert T. *Development of a "Generic" Mobile Flux Platform with Demonstration on a Small Airplane*. NOAA Technical Memorandum ERL ARL-184, National Oceanic and Atmospheric Administration, Silver Springs, Maryland, 1990.

2 Hacker, J.M. and Crawford, T.L. The BAT-probe: The ultimate tool to measure turbulence from any kind of aircraft (or sailplane). *Journal of Technical Soaring*, 23 (1999), 43-46.

3 Bunker, Andrew F. Turbulence and Shearing Sresses Measured Over the North Atlantic Ocean by an Airplane-Acceleration Technique. *Journal of Meteorology*, 12 (October 1955), 445-455.

4 Schimel, D.S. et al. Recent Patterns and Mechanisms of Carbon Exchange by Terrestrial Ecosystems. *Nature*, 414 (November 2001), 169-172.

5 Doyle, James D. Aircraft Measurements and Numerical Simulations of Mountain Waves Over the Central Alps: A Pre-MAP Test Case. *Quarterly Journal of the Royal Meteorological Society*, 128 (2002), 2175-2184.

6 Maksyutov, Shamil. NIES/FRCGC Global Atmospheric Tracer Transport Model: Description, Validation, and Surface Sources and Sinks Inversion. *Journal of the Earth Simulator*, 9 (March 2008), 3-18.

7 Brown, E. N., Friehe, C. A., and Lenschow, D. H. The Use of Pressure Fluctuations on the Nose of an Aircraft for Measuring Air Motion. *Journal of Climate and Applied Meteorology*, 22 (1983), 171-180.

8 Beswick, K. M. Application of the Aventech AIMMS20AQ Airborne Probe for Turbulence Measurements During te Convective Storm Initiation Project. *Atmospheric Chemistry and Physics Discussions*, 7 (2007), 3519-3555.

9 Lenschow, D. H. Vanes for Sensing Incidence Angles of the Air from an Aircraft. *Journal of Applied Meteorology* (December 1971), 1339-1343.

10 Telford, J. W. and Warner, J. On the Measurement from an Aircraft of Buoyancy and Vertical Air Velocity in Cloud. *Journal of the Atmospheric Sciences* (September 1962), 415-423.

11 Armistead, K. H. and Webb, L. D. *Flight Calibration Tests of a Nose-Boom-Mounted Fixed Hemispherical Flow-Direction Sensor*. 1973.

12 Wyngaard, J.C. The Effects of Probe-Induced Flow Distortion on Atmospheric Turbulence Measurements. *Journal of Applied Meteorology*, 20 (1981), 784-794.

13 Wood, R. Analysis of an Air Motion System on a Light Aircraft for Boundary Layer Research.

Journal of Atmospheric and Oceanic Technology, 14 (1997).

14 Garman, K. E. An Airbourne and Wind Tunnel Evaluation of a Wind Turbulence Measurement System for Aircraft-Based Flux Measurements. *Journal of Atmospheric and Oceanic Technology*, 23 (2006), 1696-1708.

15 Whitmore, Stephen A. *Development of a Pneumatic High-Angle-of-Attack Flush Airdata Sensing (HI-FADS) System*. NASA, 1991.

16 Cobleigh, Brent R. *Flush Airdata Sensing (FADS) System Calibration Procedures and Results for Blunt Forebodies*. NASA, 1999.

17 Larson, Terry J. and Siemers, Paul M. *Subsonic Tests of a All-Flush-Pressure-Orifice Air Data System*. NASA, 1981.

18 Whitmore, Stephen A. *Design and Calibration of the X-33 Flush Airdata Sensing (FADS) System*. NASA, 1998.

19 Axford, D. N. On the Accuracy of Wind Measurements Using an Inertial Platform in an Aircraft, and an Example of a Measurement of the Vertical Mesostructure of the Atmosphere. *Journal of Applied Meteorology*, 7 (August 1968), 645-666.

20 Crawford, Timothy J. and Dobosy, Ronald J. A Sensitive Fast-Response Probe to Measure Turulence and Heat Flux from Any Airplane. *Boundary-Layer Meteorology*, 59 (1992), 257-278.

21 *LabView 8.2*. National Instruments. 2005.

22 Crawford, Timothy L. and Dobosy, Ronald J. A Sensitive Fast-Response Probe to Measure Turulence and Heat Flux from Any Airplane. *Boundary-Layer Meteorology*, 59 (1992), 257-278.

23 Edward A. Haering, Jr. *Airdata Measurement and Calibration*. NASA Dryden Flight Research Center, Edwards, California, 1995.

APPENDIX A: DETAILS FOR CALCULATIONS OF VELOCITY COMPONENTS

Pressure differentials across the sensor head

Using $p(n) = p_s + \frac{q}{4}\left[9(N \cdot n)^2 - 5\right]$, the differential pressures work out to be:

$$\delta_k p = \frac{9}{4} q \left[\left(N \cdot n_0 \right)^2 - \left(N \cdot n_k \right)^2 \right] \tag{A.1}$$

Making it possible to compute the following:

$$\delta_1 p = \frac{9}{4} q \left[A^2 - \left(A\cos\phi + B\sin\phi \right)^2 \right] \tag{A.2}$$

$$\delta_2 p = \frac{9}{4} q \left[A^2 - (A\cos\theta + C\sin\theta)^2 \right] \tag{A.3}$$

$$\delta_3 p = \frac{9}{4} q \left[A^2 - \left(A\cos\phi - B\sin\phi \right)^2 \right] \tag{A.4}$$

$$\delta_4 p = \frac{9}{4} q \left[A^2 - (A\cos\theta - C\sin\theta)^2 \right] \tag{A.5}$$

These equations are derived using the identities:

$$N = A\,i + B\,j + C\,k$$

$$A = \frac{1}{D}\ ,\ B = \frac{\tan\beta}{D}\ ,\ C = \frac{\tan\alpha}{D}\ ,\ D = \sqrt{1 + \tan^2\beta + \tan^2\alpha}$$

$$i = n_0\ ,\ j = K_j\,(n_1 - n_3)\ ,\ k = K_k\,(n_2 - n_4)$$

$$K_j = \frac{1}{2\sin\phi}\ ,\ K_k = \frac{1}{2\sin\theta}$$

$$N \cdot n_0 = A \tag{A.6}$$

The scalar properties of vectors follow the rules of:

$$a\,(u \cdot v) = a\,|u|\,|v|\,\cos\theta = |au|\,|v|\,\cos\theta = (au) \cdot v$$

$$(a\,u + b\,v) \cdot w = (a\,u) \cdot w + (b\,v) \cdot w \tag{A.7}$$

Where a and b are scalars. Therefore:

$$\delta_1 p = \frac{9}{4}\,q\left[\left(N \cdot n_0\right)^2 - \left(N \cdot n_1\right)^2\right] \tag{A.8}$$

$$\delta_1 p = \frac{9}{4}\,q\left[A^2 - \left(N \cdot n_1\right)^2\right] \tag{A.9}$$

$$N \cdot n_1 = \left(A\,i + B\,j + C\,k\right) \cdot n_1 \tag{A.10}$$

$$N \cdot n_1 = A\left(i \cdot n_1\right) + B\left(j \cdot n_1\right) \tag{A.11}$$

$$N \cdot n_1 = A\left(n_0 \cdot n_1\right) + B\left(j \cdot n_1\right) \tag{A.12}$$

$$N \cdot n_1 = A\cos\phi + B\left(j \cdot n_1\right) \tag{A.13}$$

$$N \cdot n_1 = A\cos\phi + \left[\left(Bj\right) \cdot n_1\right] \tag{A.14}$$

$$N \cdot n_1 = A\cos\phi + \left[BK_j\left(n_1 - n_3\right) \cdot n_1\right] \tag{A.15}$$

$$N \cdot n_1 = A\cos\phi + \left(BK_j n_1 - BK_j n_3\right) \cdot n_1 \tag{A.16}$$

$$N \cdot n_1 = A\cos\phi + \left(BK_j n_1\right) \cdot n_1 - \left(BK_j n_3\right) \cdot n_1 \tag{A.17}$$

$$N \cdot n_1 = A\cos\phi + BK_j(1) - BK_j\left(n_3 \cdot n_1\right) \tag{A.18}$$

$$N \cdot n_1 = A\cos\phi + BK_j\left(1 - n_3 \cdot n_1\right) \tag{A.19}$$

$$N \cdot n_1 = A\cos\phi + BK_j\left(1 - n_1 \cdot n_3\right) \tag{A.20}$$

$$N \cdot n_1 = A\cos\phi + BK_j\left(2\sin^2\phi\right) \tag{A.21}$$

$$N \cdot n_1 = A\cos\phi + B\frac{2\sin^2\phi}{2\sin\phi} \tag{A.22}$$

$$N \cdot n_1 = A\cos\phi + B\sin\phi \tag{A.23}$$

Substituting into the original pressure difference equation:

$$\delta_1 p = \frac{9}{4} q \left[A^2 - \left(A\cos\phi + B\sin\phi \right)^2 \right] \tag{A.24}$$

Substitution of the A, B, C and D terms from expressions A.6 results in the final form in equations 8.

The derivation of

$$\delta_2 p = \frac{9}{4} q \left[A^2 - (A\cos\theta + C\sin\theta)^2 \right] \tag{A.25}$$

is performed in the same manner, with C substituted for B and θ for ϕ.

The derivation of $\delta_3 p$ is performed slightly differently, as shown:

$$\delta_3 p = \frac{9}{4} q \left[\left(N \cdot n_0 \right)^2 - \left(N \cdot n_3 \right)^2 \right] \tag{A.26}$$

$$N \cdot n_3 = \left(A\,i + B\,j + C\,k \right) \cdot n_3 \tag{A.27}$$

$$N \cdot n_3 = A\left(i \cdot n_3 \right) + B\left(j \cdot n_3 \right) \tag{A.28}$$

$$N \cdot n_3 = A\left(n_0 \cdot n_3 \right) + B\left(j \cdot n_3 \right) \tag{A.29}$$

$$N \cdot n_3 = A\cos\phi + B\left(j \cdot n_3 \right) \tag{A.30}$$

$$N \cdot n_3 = A\cos\phi + \left[\left(Bj\right) \cdot n_3\right] \tag{A.31}$$

$$N \cdot n_3 = A\cos\phi + BK_j\left(n_1 - n_3\right) \cdot n_3 \tag{A.32}$$

$$N \cdot n_3 = A\cos\phi + \left(BK_j\, n_1 - BK_j\, n_3\right) \cdot n_3 \tag{A.33}$$

$$N \cdot n_3 = A\cos\phi + BK_j\, n_1 \cdot n_3 - BK_j\, n_3 \cdot n_3 \tag{A.34}$$

$$N \cdot n_3 = A\cos\phi + BK_j\, n_1 \cdot n_3 - BK_j\,(1) \tag{A.35}$$

$$N \cdot n_3 = A\cos\phi + BK_j\left(n_1 \cdot n_3 - 1\right) \tag{A.36}$$

$$N \cdot n_3 = A\cos\phi + BK_j\,(-1)\left(1 - n_1 \cdot n_3\right) \tag{A.37}$$

$$N \cdot n_3 = A\cos\phi - BK_j\left(2\sin^2\phi\right) \tag{A.38}$$

$$N \cdot n_3 = A\cos\phi - B\frac{2\sin^2\phi}{2\sin\phi} \tag{A.39}$$

$$N \cdot n_3 = A\cos\phi - B\sin\phi \tag{A.40}$$

$$\delta_3 p = \frac{9}{4} q\left[(A)^2 - \left(A\cos\phi - B\sin\phi\right)^2\right] \tag{A.41}$$

Substitution of the A, B, C and D terms from expressions A.6 results in the final form in equations 8.

Derivation of

$$\delta_4 p = \frac{9}{4} q \left[A^2 - (A\cos\theta - C\sin\theta)^2 \right] \tag{A.42}$$

is performed in the same manner, with C substituted for B and θ for ϕ.

The high resolution, low resolution, NCAR and Ekman methods all use the pressure differences across the hemispherical head in the computation of flow angles and subsequently dynamic and static pressures. The sums and differences of the four $\delta_k p$ terms are shown here. The sums and differences required by the three methods simplify to:

$$\delta_4 p + \delta_2 p = \frac{9}{2} q \left(A^2 - C^2 \right) \sin^2\theta \tag{A.43}$$

$$\delta_4 p - \delta_2 p = \frac{9}{2} q AC \sin 2\theta \tag{A.44}$$

$$\delta_3 p + \delta_1 p = \frac{9}{2} q \left(A^2 - B^2 \right) \sin^2\phi \tag{A.45}$$

$$\delta_3 p - \delta_1 p = \frac{9}{2} q AC \sin 2\phi \tag{A.46}$$

The basic use of these equations is to relate the differential pressures to the flow angle parameters implicit in A, B and C.

A worked example:

$$\delta_4 p + \delta_2 p = \frac{9}{4} q \left[A^2 - (A\cos\theta - C\sin\theta)^2 \right] + \frac{9}{4} q \left[A^2 - (A\cos\theta + C\sin\theta)^2 \right] \tag{A.47}$$

$$\begin{aligned} \delta_4 p + \delta_2 p = {} & \frac{9}{4} q \left[A^2 - (A\cos\theta - C\sin\theta)(A\cos\theta - C\sin\theta) \right] \\ & + \frac{9}{4} q \left[A^2 - (A\cos\theta + C\sin\theta)(A\cos\theta + C\sin\theta) \right] \end{aligned} \tag{A.48}$$

$$\begin{aligned} \delta_4 p + \delta_2 p = {} & \frac{9}{4} q \left(A^2 - A^2\cos^2\theta + 2AC\cos\theta\sin\theta - C^2\sin^2\theta \right) \\ & + \frac{9}{4} q \left(A^2 - A^2\cos^2\theta - 2AC\cos\theta\sin\theta - C^2\sin^2\theta \right) \end{aligned} \tag{A.49}$$

$$\delta_4 p + \delta_2 p = \frac{9}{4} q \left(A^2 - A^2\cos^2\theta - C^2\sin^2\theta + A^2 - A^2\cos^2\theta - C^2\sin^2\theta \right) \tag{A.50}$$

$$\delta_4 p + \delta_2 p = \frac{9}{2} q \left(A^2 - A^2\cos^2\theta - C^2\sin^2\theta \right) \tag{A.51}$$

Using the trigonometric identity $\cos^2 u = 1 - \sin^2 u$, the equation expands to:

$$\delta_4 p + \delta_2 p = \frac{9}{2} q \left[A^2 - A^2\left(1 - \sin^2\theta\right) - C^2\sin^2\theta \right] \tag{A.52}$$

$$\delta_4 p + \delta_2 p = \frac{9}{2} q \left(A^2\sin^2\theta - C^2\sin^2\theta \right) \tag{A.53}$$

$$\delta_4 p + \delta_2 p = \frac{9}{2} q \left(A^2 - C^2 \right)\sin^2\theta \tag{A.54}$$

Derivation of

$$\delta_4 p - \delta_2 p = \frac{9}{2} q\, AC \sin 2\theta \tag{A.55}$$

$$\delta_4 p - \delta_2 p = \frac{9}{4} q \left[A^2 - (A\cos\theta - C\sin\theta)^2 \right] - \frac{9}{4} q \left[A^2 - (A\cos\theta + C\sin\theta)^2 \right] \tag{A.56}$$

$$\begin{aligned} \delta_4 p - \delta_2 p = {} & \frac{9}{4} q \left[A^2 - (A\cos\theta - C\sin\theta)(A\cos\theta - C\sin\theta) \right] \\ & - \frac{9}{4} q \left[A^2 - (A\cos\theta + C\sin\theta)(A\cos\theta + C\sin\theta) \right] \end{aligned} \tag{A.57}$$

$$\begin{aligned} \delta_4 p - \delta_2 p = {} & \frac{9}{4} q \left(A^2 - A^2\cos^2\theta - 2AC\sin\theta\cos\theta + C^2\sin^2\theta \right) \\ & - \frac{9}{4} q \left(A^2 - A^2\cos^2\theta + 2AC\sin\theta\cos\theta + C^2\sin^2\theta \right) \end{aligned} \tag{A.58}$$

$$\delta_4 p - \delta_2 p = \frac{9}{4} q\,(2AC\sin\theta\cos\theta) + \frac{9}{4} q\,(2AC\sin\theta\cos\theta) \tag{A.59}$$

$$\delta_4 p - \delta_2 p = \frac{9}{2} q\, AC\,(\sin\theta\cos\theta + \sin\theta\cos\theta) \tag{A.60}$$

$$\delta_4 p - \delta_2 p = \frac{9}{2} q\, AC\,(2\sin\theta\cos\theta) \tag{A.61}$$

Using trigonometric identity $2\sin u \cos u = \sin 2u$, the final result is:

$$\delta_4 p - \delta_2 p = \frac{9}{2} q\, AC \sin 2\theta \tag{A.62}$$

Derivations of:

$$\delta_3 p + \delta_1 p = \frac{9}{2} q \left(A^2 - B^2 \right) \sin^2 \phi \tag{A.63}$$

and

$$\delta_3 p - \delta_1 p = \frac{9}{2} q AC \sin 2\phi \tag{A.64}$$

are performed in the same manner, with C substituted for B and θ for ϕ.

Exact solution of the High Resolution Method

The High Resolution model is the easiest to solve, compute the quotients of the measured parameters and see what happens:

$$\frac{\delta_4 p - \delta_2 p}{\delta_4 p + \delta_2 p} = \frac{AC \sin 2\theta}{\left(A^2 - C^2\right)\sin^2\theta} = \left[\frac{2\tan\alpha}{1-\tan^2\alpha}\right]\frac{1}{\tan\theta} = \frac{\tan 2\alpha}{\tan\theta} \tag{A.65}$$

$$\frac{\delta_3 P - \delta_1 p}{\delta_3 p + \delta_1 p} = \frac{AB \sin 2\phi}{\left(A^2 - B^2\right)\sin^2\phi} = \left[\frac{2\tan\beta}{1-\tan^2\beta}\right]\frac{1}{\tan\phi} = \frac{\tan 2\beta}{\tan\phi} \tag{A.66}$$

Explained step by step:

$$\frac{\delta_4 p - \delta_2 p}{\delta_4 p + \delta_2 p} = \frac{\left(\frac{9}{2}\right)(q)\, AC \sin 2\theta}{\left(\frac{9}{2}\right)(q)\left(A^2 - C^2\right)\sin^2\theta} = \frac{AC \sin 2\theta}{\left(A^2 - C^2\right)\sin^2\theta} \tag{A.67}$$

Using the trig identity $\sin 2u = 2\sin u \cos u$:

$$\frac{\delta_4 p - \delta_2 p}{\delta_4 p + \delta_2 p} = \frac{AC\,(2)\sin\theta\cos\theta}{\left(A^2 - C^2\right)\sin^2\theta} \tag{A.68}$$

$$\frac{\delta_4 p - \delta_2 p}{\delta_4 p + \delta_2 p} = \frac{2AC\cos\theta}{\left(A^2 - C^2\right)\sin\theta} \tag{A.69}$$

$$\frac{\delta_4 p - \delta_2 p}{\delta_4 p + \delta_2 p} = \frac{2AC}{\left(A^2 - C^2\right)\tan\theta} \tag{A.70}$$

$$\frac{\delta_4 p - \delta_2 p}{\delta_4 p + \delta_2 p} = \frac{2\left(\frac{1}{D}\right)\frac{\tan\alpha}{D}}{\left[\left(\frac{1}{D^2}\right) - \frac{\tan^2\alpha}{D^2}\right]\tan\theta} \tag{A.71}$$

$$\frac{\delta_4 p - \delta_2 p}{\delta_4 p + \delta_2 p} = \frac{\frac{2\tan\alpha}{D^2}}{\frac{1-\tan^2\alpha}{D^2}(\tan\theta)} \tag{A.72}$$

$$\frac{\delta_4 p - \delta_2 p}{\delta_4 p + \delta_2 p} = \frac{2\tan\alpha}{\left(1-\tan^2\alpha\right)(\tan\theta)} \tag{A.73}$$

Using the trig identity $\frac{2\tan u}{1-\tan^2 u} = \tan 2u$:

$$\frac{\delta_4 p - \delta_2 p}{\delta_4 p + \delta_2 p} = \frac{\tan 2\alpha}{\tan\theta} \tag{A.74}$$

It is possible to solve for tan2α and tan2β; however, to obtain an equation directly relating pressure differences to flow angles, intermediate terms are developed in terms of tanα and tanβ. First we define F_α and F_β:

$$F_\alpha = \frac{\tan\theta}{2}\left[\frac{\delta_4 p - \delta_2 p}{\delta_4 p + \delta_2 p}\right] \tag{A.75}$$

$$F_\beta = \frac{\tan\phi}{2}\left[\frac{\delta_3 p - \delta_1 p}{\delta_3 p + \delta_1 p}\right] \tag{A.76}$$

The F_α and F_β terms can be calculated directly from measured parameters. Substitution then yields quadratic equations in tanα and tanβ:

$$\left(1-\tan^2\alpha\right)F_\alpha = \tan\alpha \tag{A.77}$$

$$\left(1-\tan^2\beta\right)F_\beta = \tan\beta \tag{A.78}$$

F_α and F_β are first order estimates of the exact solutions:

$$\tan\alpha = \frac{2F_\alpha}{\left(1+\sqrt{1+4F_\alpha^2}\right)}$$

(A.79)

$$\tan\beta = \frac{2F_\beta}{\left(1+\sqrt{1+4F_\beta^2}\right)} \tag{A.80}$$

Shown step by step:

$$\frac{\delta_4 p - \delta_2 p}{\delta_4 p + \delta_2 p} = \frac{\tan 2\alpha}{\tan\theta} \tag{A.81}$$

$$\left[\frac{\delta_4 p - \delta_2 p}{\delta_4 p + \delta_2 p}\right](\tan\theta) = \tan 2\alpha \tag{A.82}$$

Using the trig identity $\tan 2u = \frac{2\tan u}{1-\tan^2 u}$:

$$\left[\frac{\delta_4 p - \delta_2 p}{\delta_4 p + \delta_2 p}\right](\tan\theta) = \frac{2\tan\alpha}{1-\tan^2\alpha} \tag{A.83}$$

$$\left[\frac{\delta_4 p - \delta_2 p}{\delta_4 p + \delta_2 p}\right]\frac{\tan\theta}{2} = \frac{\tan\alpha}{1-\tan^2\alpha} \tag{A.84}$$

$$F_\alpha = \frac{\tan\theta}{2}\left[\frac{\delta_4 p - \delta_2 p}{\delta_4 p + \delta_2 p}\right] \tag{A.85}$$

$$F_\alpha = \frac{\tan\alpha}{1-\tan^2\alpha}$$

(A.86)

$$\left(1-\tan^2\alpha\right)F_\alpha = \tan\alpha \tag{A.87}$$

$$F_\alpha - F_\alpha\left(\tan^2\alpha\right) = \tan\alpha$$

(A.88)

$$F_\alpha \tan^2\alpha + \tan\alpha - F_\alpha = 0 \tag{A.89}$$

Exact solution to Low Resolution Model

Taking the pressure differences across the head and a separate source of dynamic pressure allows the incident flow angles and the static pressure to be estimated:

$$\delta_4 p + \delta_2 p = \frac{9}{2} q \left(A^2 - C^2 \right) \sin^2 \theta \tag{A.90}$$

$$\delta_4 p - \delta_2 p = \frac{9}{2} q AC \sin 2\theta \tag{A.91}$$

$$\delta_3 p + \delta_1 p = \frac{9}{2} q \left(A^2 - B^2 \right) \sin^2 \phi \tag{A.92}$$

$$\delta_3 p - \delta_1 p = \frac{9}{2} q AC \sin 2\phi \tag{A.93}$$

Inserting equations 90 through 93 into the low resolution model gives an equation for angle of attack:

$$\alpha = \frac{p_2 - p_4}{K_2 q_c} = \frac{\delta_4 p - \delta_2 p}{K_2 q_c} \tag{A.94}$$

$$\frac{p_2 - p_4}{q} = \frac{9}{2} AC \sin 2\theta \tag{A.95}$$

$$\frac{p_2 - p_4}{q} = \frac{9}{2} \frac{1}{D} \frac{\tan\alpha}{D} \sin 2\theta \tag{A.96}$$

$$\frac{p_2 - p_4}{q} = \frac{\frac{9}{2}\tan\alpha \sin 2\theta}{D^2} \tag{A.97}$$

$$\frac{p_2 - p_4}{q} = \frac{\frac{9}{2}\tan\alpha \sin 2\theta}{1 - \tan^2\beta + \tan^2\alpha} \tag{A.98}$$

The equation for angle of sideslip follows the same method to give:

$$\frac{p_1 - p_3}{q} = \frac{\frac{9}{2}\tan\beta \sin 2\phi}{1 - \tan^2\beta + \tan^2\alpha} \tag{A.99}$$

In order to solve directly for the flow angles, secondary quantities are again used. Defining secondary quantities G_α and G_β gives:

$$G_\alpha = \frac{2}{9\sin 2\theta}\left[\frac{p_2 - p_4}{q}\right] \tag{A.100}$$

$$G_\beta = \frac{2}{9\sin 2\phi}\left[\frac{p_1 - p_3}{q}\right] \tag{A.101}$$

Shown step by step:

$$\frac{p_2 - p_4}{q} = \frac{\frac{9}{2}\tan\alpha\sin 2\theta}{1 - \tan^2\beta + \tan^2\alpha} \tag{A.102}$$

$$\left[\frac{p_2 - p_4}{q}\right]\frac{2}{9\sin 2\theta} = \frac{\tan\alpha}{1 + \tan^2\beta + \tan^2\alpha} \tag{A103}$$

$$G_\alpha = \frac{\tan\alpha}{1 + \tan^2\beta + \tan^2\alpha} \tag{A.104}$$

Resulting in a coupled quadratic equation for tanα:

$$\tan\alpha = G_\alpha\left(1 + \tan^2\beta + \tan^2\alpha\right) \tag{A.105}$$

Following the same working for angle of sideslip determination results in a coupled quadratic equation for tanβ:

$$\tan\beta = G_\beta\left(1 + \tan^2\beta + \tan^2\alpha\right) \tag{A.106}$$

This is a coupled set of quadratic equations in tanα and tanβ can be decoupled by taking quotients, resulting in:

$$G_\alpha \tan\beta = G_\beta \tan\alpha \tag{A.107}$$

The decoupled equations result in closed form solutions that are weakly coupled:

$$\tan\alpha = \frac{2G_\alpha}{1+\sqrt{1-4\left(G_\alpha^2+G_\beta^2\right)}} \tag{A.108}$$

$$\tan\beta = \frac{2G_\beta}{1+\sqrt{1-4\left(G_\alpha^2+G_\beta^2\right)}} \tag{A.109}$$

Exact solution to the NCAR Model

The added complexity here is that the pressure difference $p_0 - p_s$ must also be calculated. This is accomplished with:

$$p(n) = p_s + \frac{q}{4}\left[9(N\cdot n)^2 - 5\right] \tag{A.110}$$

$$p_0 - p_s = \frac{q}{4}\left[9\left(N\cdot n_0\right)^2 - 5\right] \tag{A.111}$$

$$p_0 - p_s = \frac{q}{4}\left[9(A)^2 - 5\right] \tag{A.112}$$

$$p_0 - p_s = \frac{q}{4}\left[9\left(\frac{1}{D}\right)^2 - 5\right] \tag{A.113}$$

$$p_0 - p_s = \frac{q}{4}\left[\frac{9}{D^2} - 5\right] \tag{A.114}$$

$$p_0 - p_s = \frac{q}{4}\left[\frac{9}{D^2} - \left(5\frac{D^2}{D^2}\right)\right] \tag{A.115}$$

$$p_0 - p_s = \frac{q}{4}\left[\frac{9}{D^2} - \frac{5\left(1 + \tan^2\beta + \tan^2\alpha\right)}{D^2}\right] \tag{A.116}$$

$$p_0 - p_s = \frac{q}{4}\left[\frac{4 - 5\tan^2\beta - 5\tan^2\alpha}{D^2}\right] \tag{A.117}$$

$$p_0 - p_s = q\left[\frac{1 - \frac{5}{4}\tan^2\beta - \frac{5}{4}\tan^2\alpha}{D^2}\right] \tag{A.118}$$

$$p_0 - p_s = q\left[\frac{1 - \frac{5}{4}\left(\tan^2\beta + \tan^2\alpha\right)}{D^2}\right] \tag{A.119}$$

Substituting this into the NCAR method equation:

$$\frac{p_2 - p_4}{p_0 - p_s} = \frac{\delta_4 p - \delta_2 p}{p_0 - p_s} \tag{A.120}$$

$$\frac{p_2 - p_4}{p_0 - p_s} = \frac{\frac{\frac{9}{2}\tan\alpha\sin 2\theta}{D^2}}{\frac{q\left[1 - \frac{5}{4}\left(\tan^2\beta + \tan^2\alpha\right)\right]}{D^2}} \tag{A.121}$$

$$\frac{p_2 - p_4}{p_0 - p_s} = \frac{\frac{9}{2}\tan\alpha\sin 2\theta}{q\left[1 - \frac{5}{4}\left(\tan^2\beta + \tan^2\alpha\right)\right]} \tag{A.122}$$

In order to obtain equations directly relating flow angles to measured parameters, secondary equations are once again defined:

$$H_{\alpha} = \frac{2}{9\sin 2\theta}\left[\frac{p_2 - p_4}{p_0 - p_s}\right] \tag{A.123}$$

$$H_{\beta} = \frac{2}{9\sin 2\phi}\left[\frac{p_1 - p_3}{p_0 - p_s}\right] \tag{A.124}$$

Shown step by step:

$$\frac{p_2 - p_4}{p_0 - p_s} = \frac{\frac{9}{2}\tan\alpha \sin 2\theta}{q\left[1 - \frac{5}{4}\left(\tan^2\beta + \tan^2\alpha\right)\right]} \tag{A.125}$$

$$\left[\frac{p_2 - p_4}{p_0 - p_s}\right]\frac{2}{9\sin 2\theta} = \frac{\tan\alpha}{q\left[1 - \frac{5}{4}\left(\tan^2\beta + \tan^2\alpha\right)\right]} \tag{A.126}$$

$$H_{\alpha} = \frac{\tan\alpha}{q\left[1 - \frac{5}{4}\left(\tan^2\beta + \tan^2\alpha\right)\right]} \tag{A.127}$$

The equations for H_{β} follow the same method.

Exact solution to the Ekman Model

The Ekman method is essentially the same as the NCAR method, with the separate source of dynamic pressure replaced with the average pressure difference between the center port and the four outer reference pressure ports. The relationship between the reference pressure ports and static pressure measurement is illustrated by converting the potential flow equation from vector quantities to trigonometric form using the identity $N \cdot n = \cos\gamma$, where γ is the angle between the stagnation point of the incident flow and the pressure port. The resulting potential flow equation is then:

$$p(n) = p_s + q\left(1 - \frac{9}{4}\sin^2\gamma\right) \tag{A.128}$$

The derivation of equation 128 follows the form of:

$$p(n) = p_s + \frac{q}{4}\left[9(\cos\gamma)^2 - 5\right] \tag{A.129}$$

$$p(n) = p_s + \frac{q}{4}\left[9\cos^2\gamma - 5\right] \tag{A.130}$$

Then, following the trigonometric identity $\cos^2\gamma = 1 - \sin^2\gamma$:

$$p(n) = p_s + \frac{q}{4}\left[9\left(1-\sin^2\gamma\right)-5\right] \tag{A.131}$$

$$p(n) = p_s + \frac{q}{4}\left[9-9\sin^2\gamma-5\right] \tag{A.132}$$

$$p(n) = p_s + \frac{q}{4}\left[4-9\sin^2\gamma\right] \tag{A.133}$$

$$p(n) = p_s + \frac{4q}{4} - \frac{9q\sin^2\gamma}{4} \tag{A.134}$$

$$p(n) = p_s + q\left(1-\frac{9}{4}\sin^2\gamma\right) \tag{A.135}$$

From equation 135 it can be seen that, if the reference pressure ports are placed at a 41.81° angle from the center of the probe head, the pressure reported by the heads will be equal to the static pressure.

The Ekman method uses pressure differentials $\delta p_x, \delta p_y, \delta p_z$ to obtain the flow angle values. The method is essentially the same as the NCAR method but with a slightly different mathematical approach. First, Ekman derives pressure difference equations for angle of attack and angle of sideslip:

$$\delta p_z = 9q\frac{\sin\theta\cos\theta}{D^2}\tan\alpha \tag{A.136}$$

$$\delta p_y = 9q\frac{\sin\phi\cos\phi}{D^2}\tan\beta \tag{A.137}$$

Equation 136 is derived from the potential flow equation in the following manner:

$$\delta p_z = \delta_4 p - \delta_2 p = \frac{9}{2} q\, AB \sin 2\theta \tag{A.138}$$

$$\delta p_z = \frac{9}{2} q \frac{\tan\alpha}{D^2} \sin 2\theta \tag{A.139}$$

$$\delta p_z = \frac{9}{2} q \frac{2\sin\theta\cos\theta}{D^2} \tan\alpha \tag{A.140}$$

$$\delta p_z = 9 q \frac{\sin\theta\cos\theta}{D^2} \tan\alpha \tag{A.141}$$

Equation 137 is derived in exactly the same way, with angle of sideslip substituted for angle of attack.

For the reference pressure ports, Ekman derives an equation that is equal to equation 128, but expressed in terms of flow angles instead of using the intermediate term γ. Using the Ekman method equation 129 is used to describe the potential flow, instead of equation 128, and, with the flow angles inserted, the reference pressure equation becomes:

$$p_r = p_s + \frac{q}{4}\left[9 \frac{\cos^2\phi_r + 0.5\left(\tan^2\alpha + \tan^2\beta\right)\sin^2\phi_r}{D^2} - 5 \right] \tag{A.142}$$

The estimation of dynamic pressure required is therefore:

$$\delta p_x = p_0 - p_r = \frac{9q}{8D^2} \sin^2 \phi_r \left(3 - D^2\right) \tag{A.143}$$

The remaining steps are as described in the theory section.

APPENDIX B: DETAIL OF BENCH TEST RESULTS

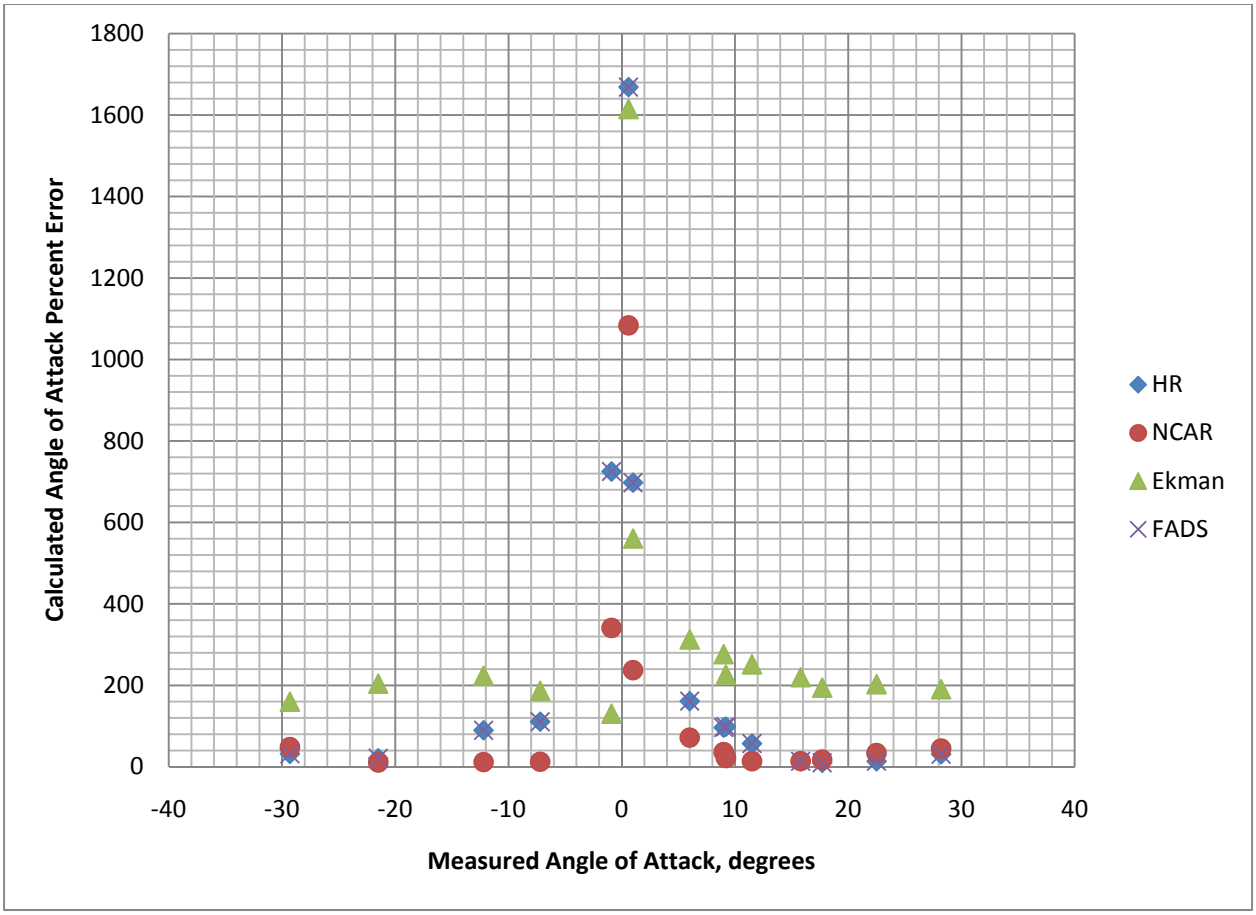

Figure B.1: Calculated angle of attack percent error vs. measured angle of attack, 45° head.

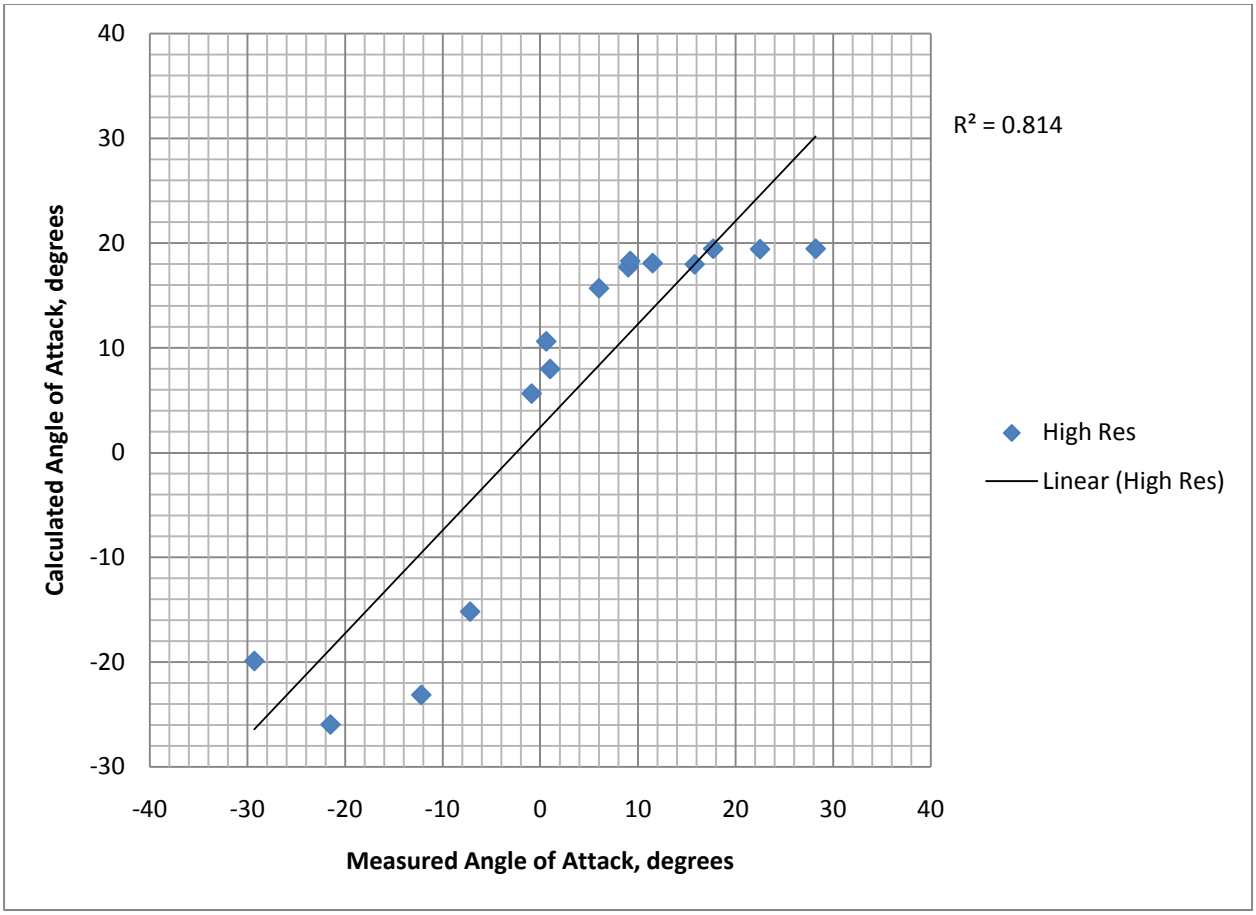

Figure B.2: Calculated angle of attack vs. measured angle of attack, 45° probe head, High Resolution method

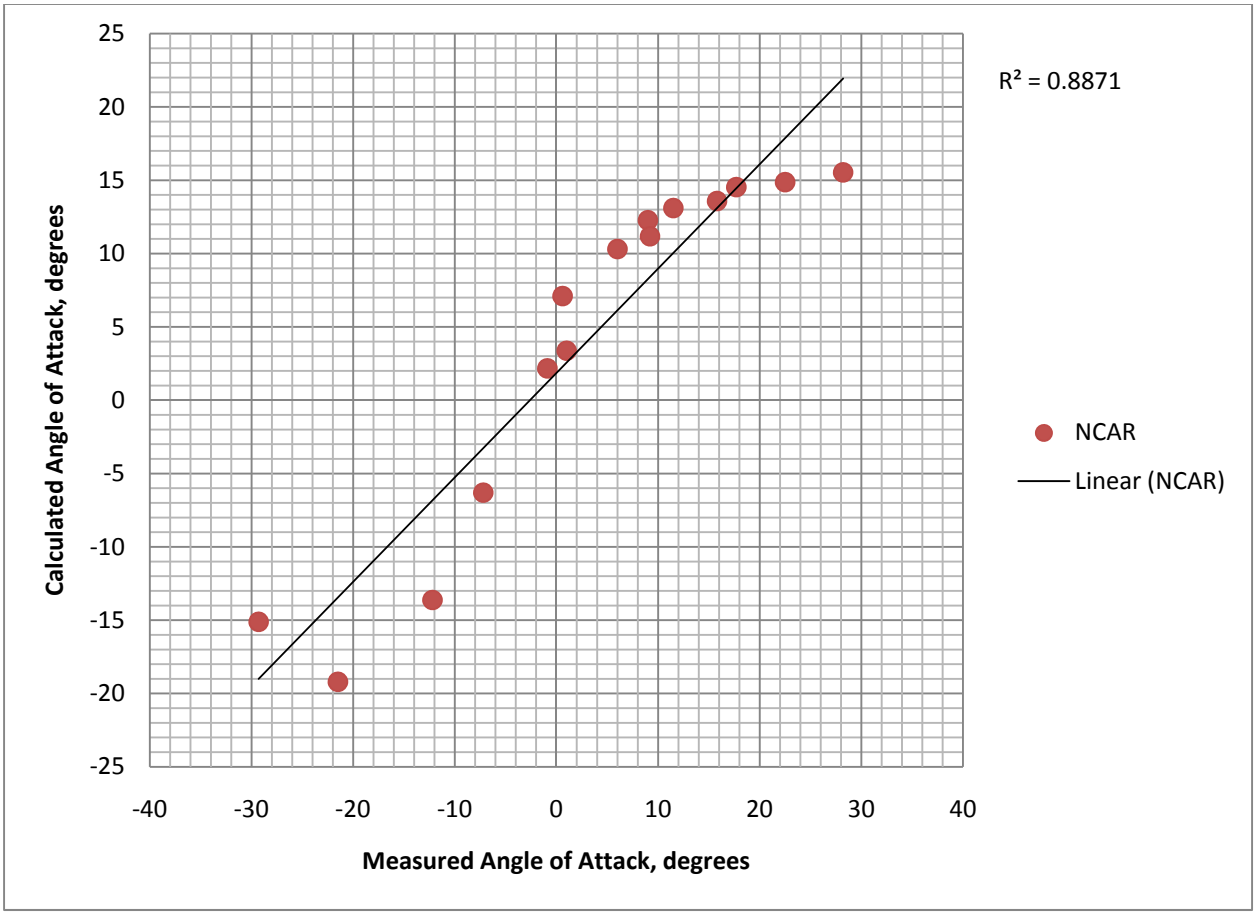

Figure B.3: Calculated angle of attack vs. measured angle of attack, 45° probe head, NCAR method.

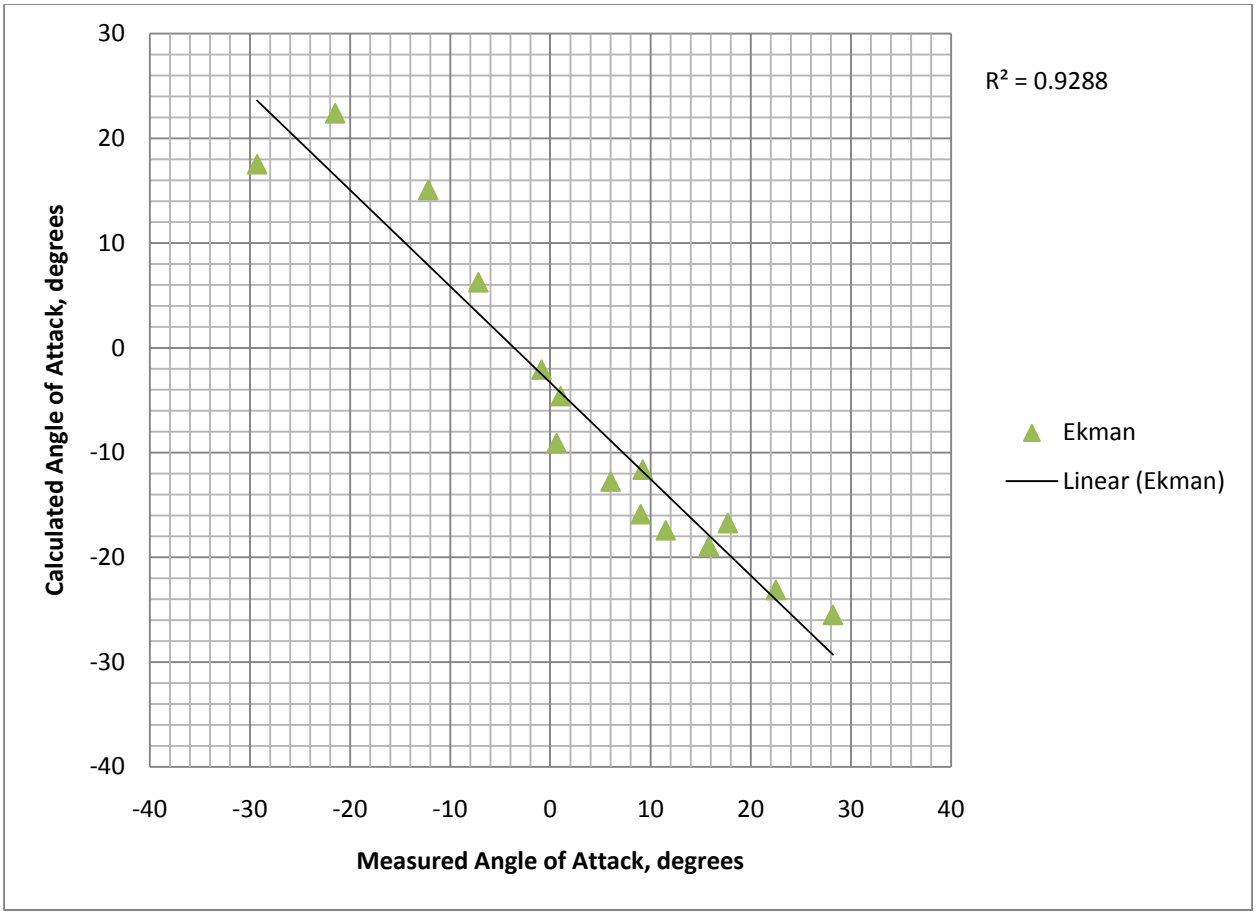

Figure B.4: Calculated angle of attack vs. measured angle of attack, 45° probe head, Ekman method.

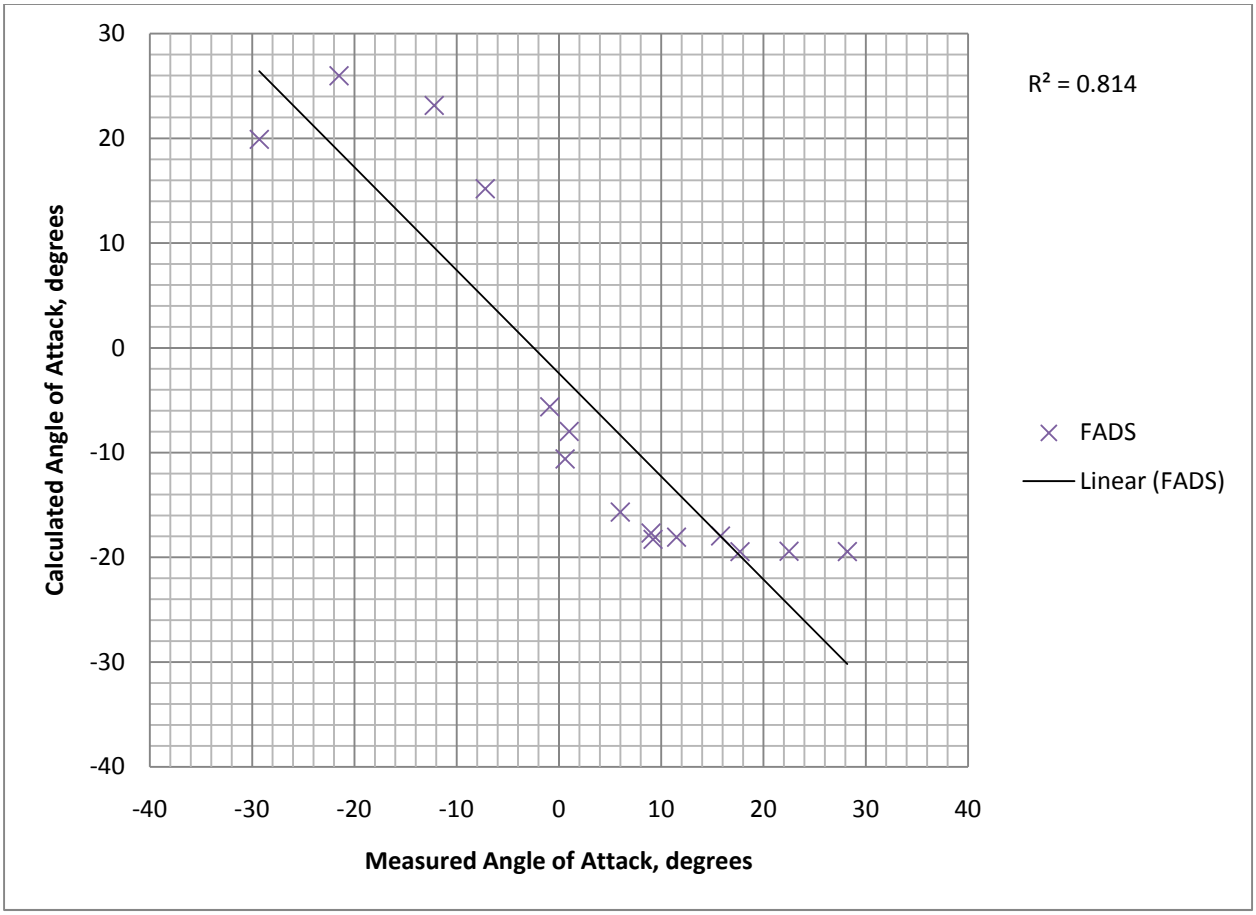

Figure B.5: Calculated angle of attack vs. measured angle of attack, 45° probe head, FADS method.

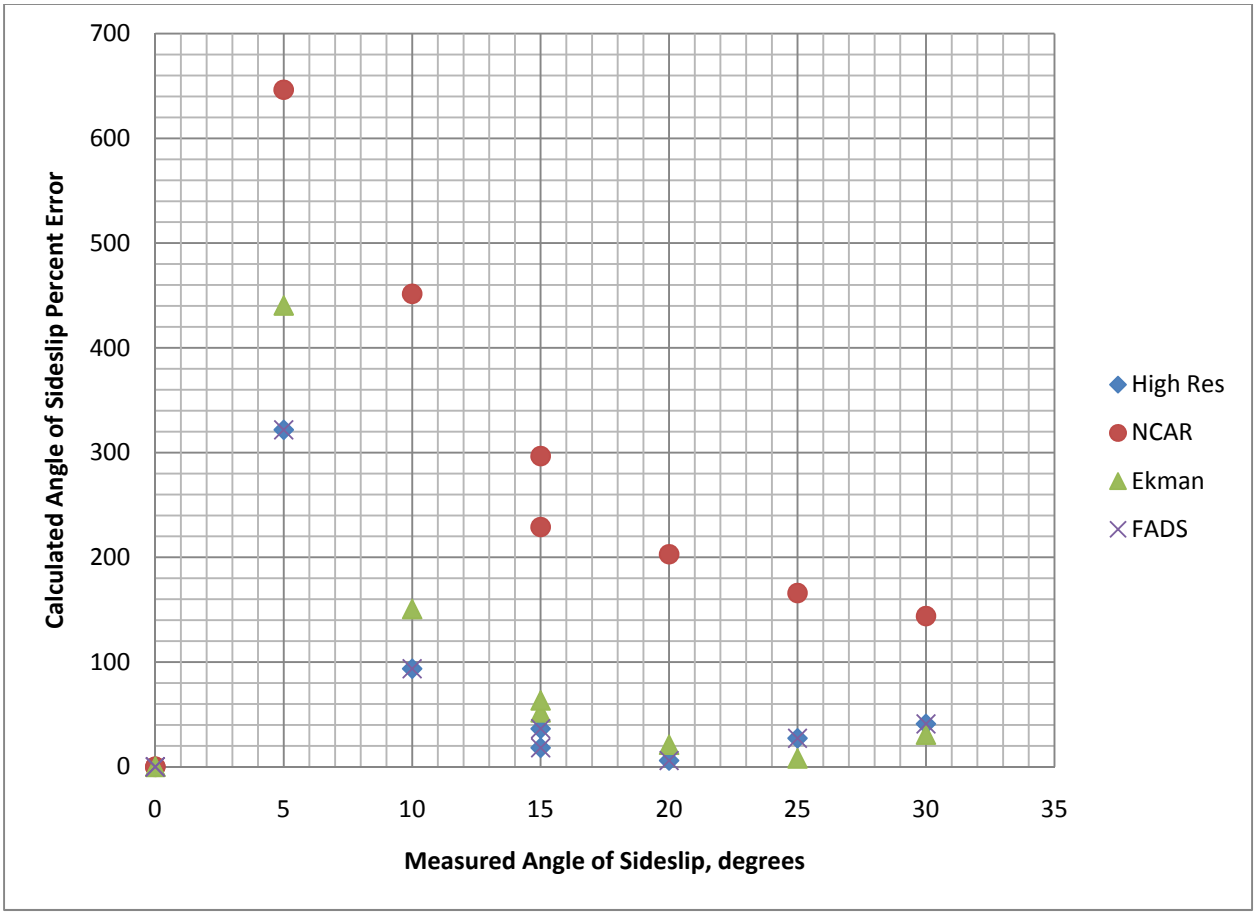

Figure B.6: Percent error in calculated angle of attack measurement, positive values, 45° head.

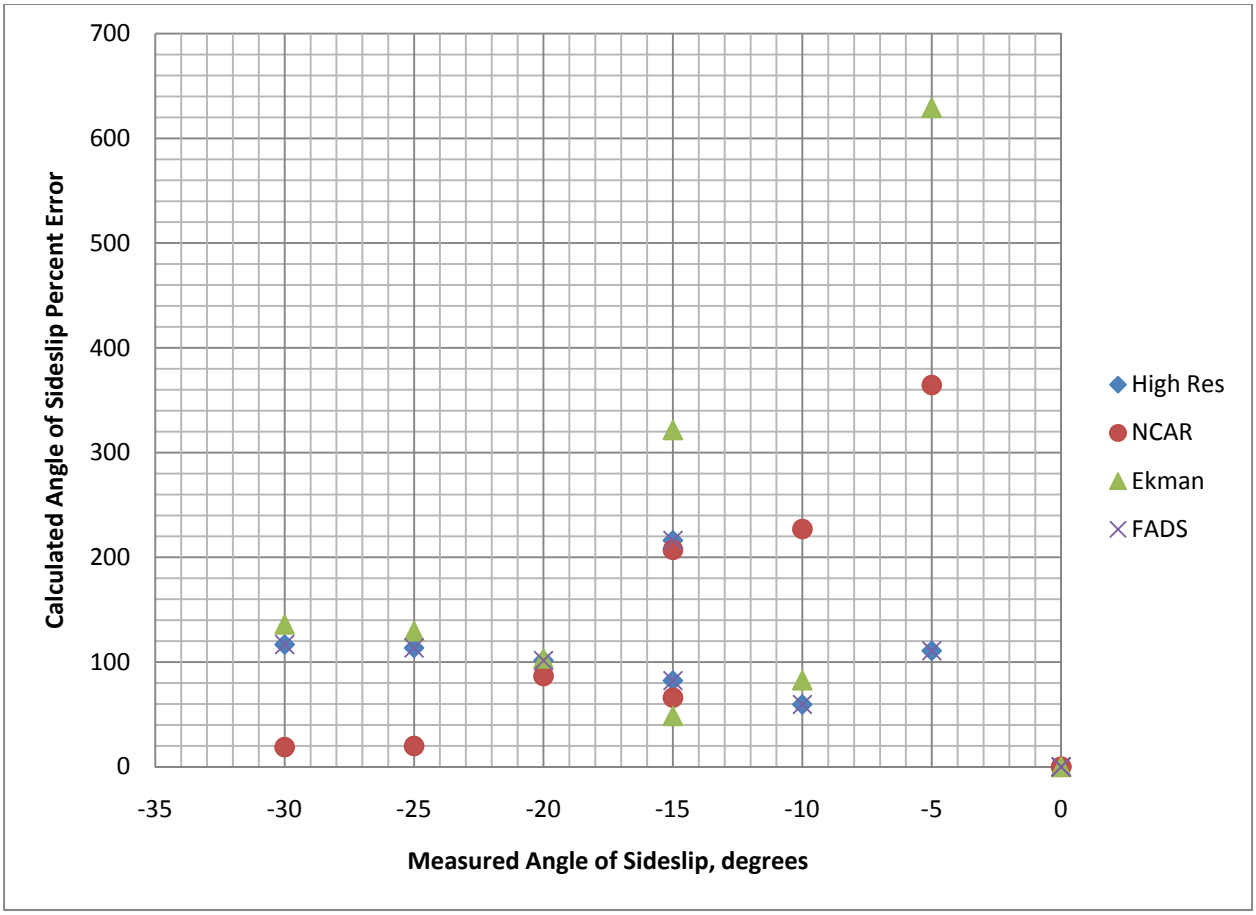

Figure B.7: Percent error in calculated angle of attack measurement, negative values, 45° head.

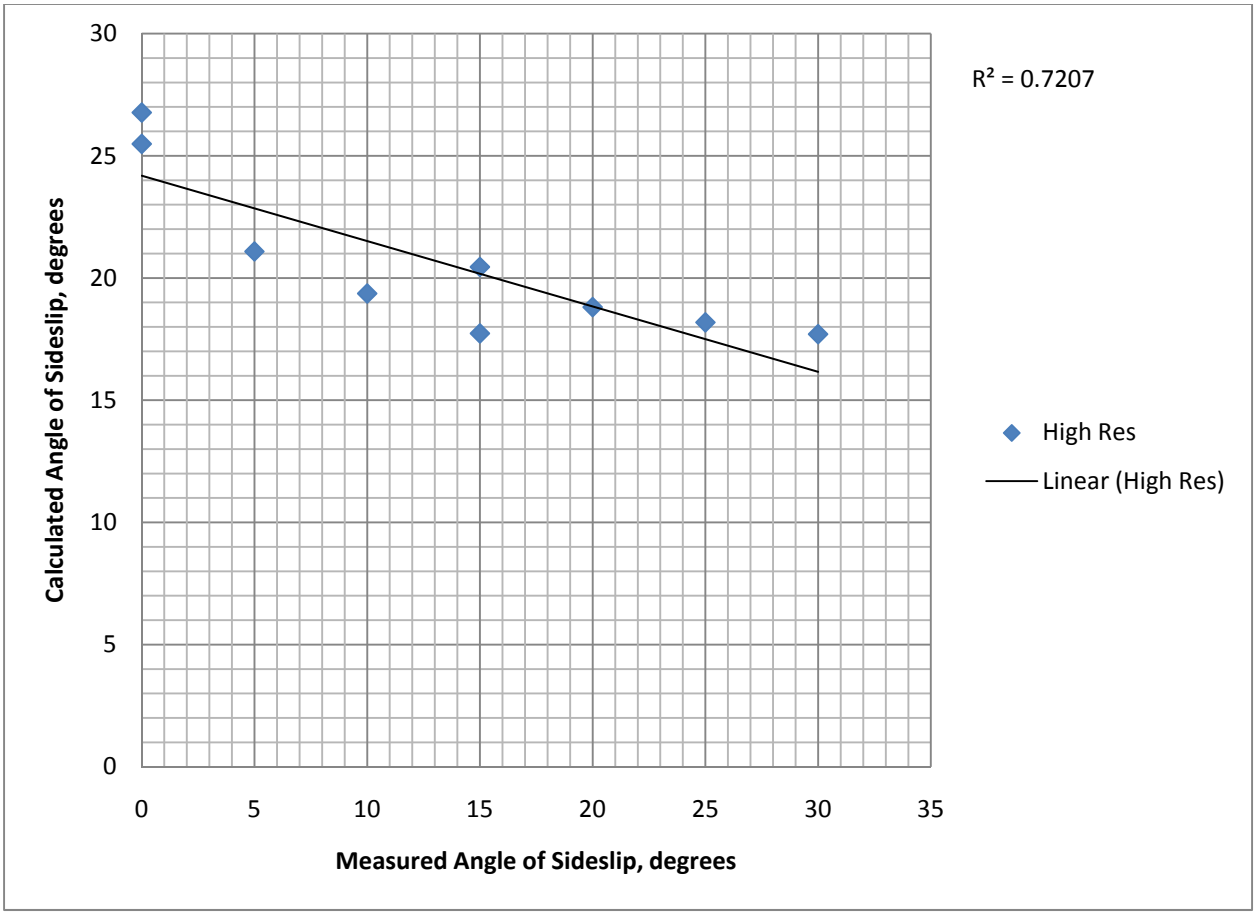

Figure B.8: Calculated angle of sideslip vs. measured angle of sideslip, positive values, 45° probe head, High Resolution method.

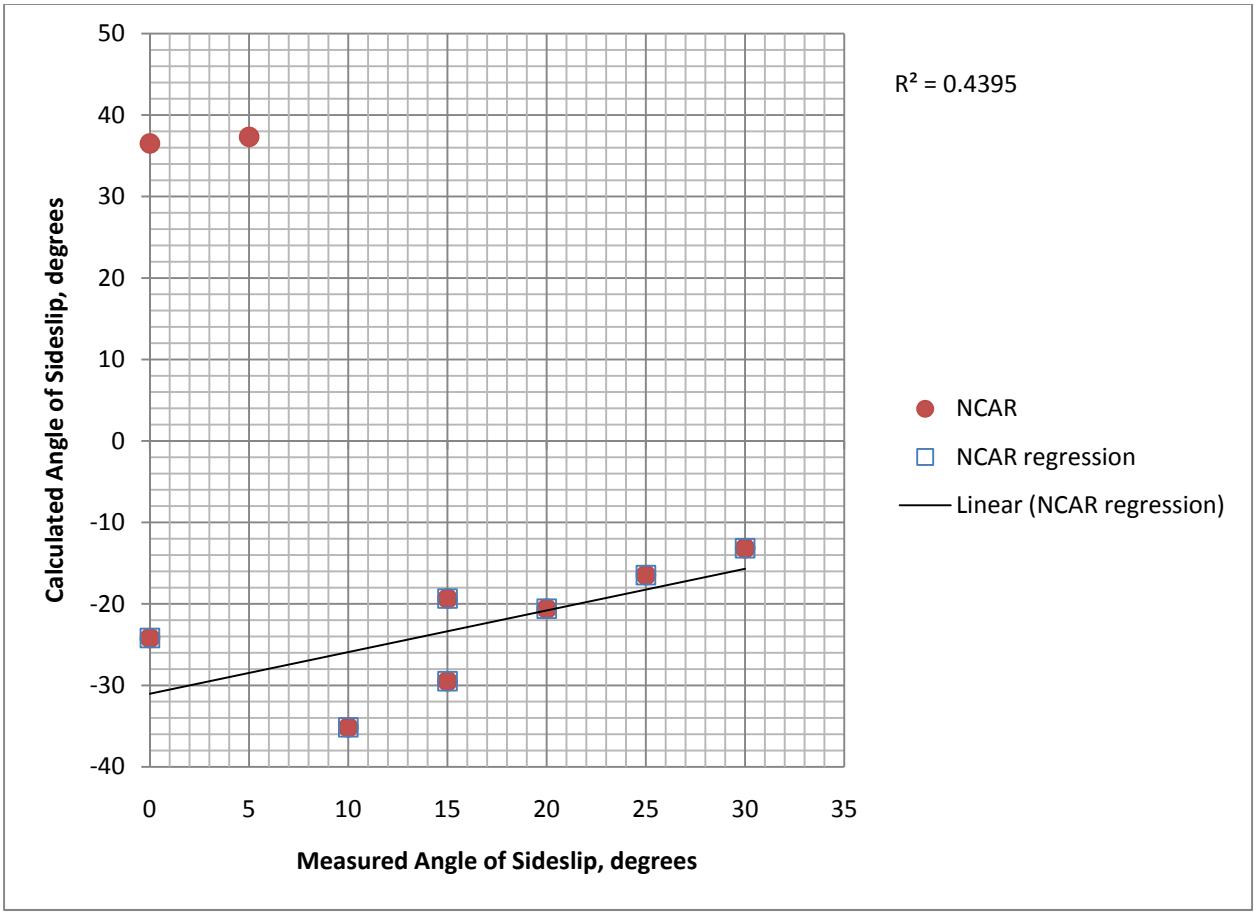

Figure B.9: Calculated angle of sideslip vs. measured angle of sideslip, positive values, 45° probe head, NCAR method.

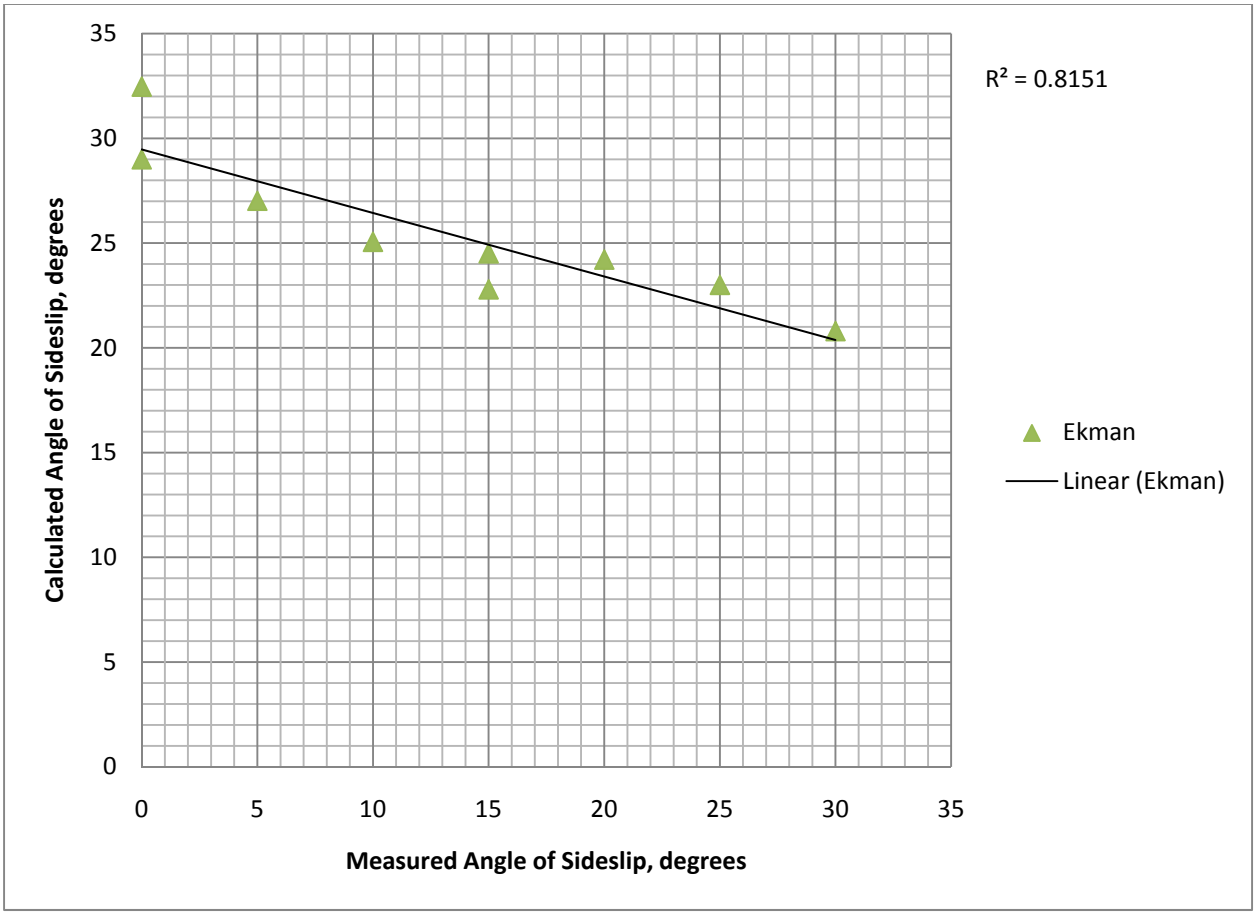

Figure B.10: Calculated angle of sideslip vs. measured angle of sideslip, positive values, 45° probe head, Ekman method.

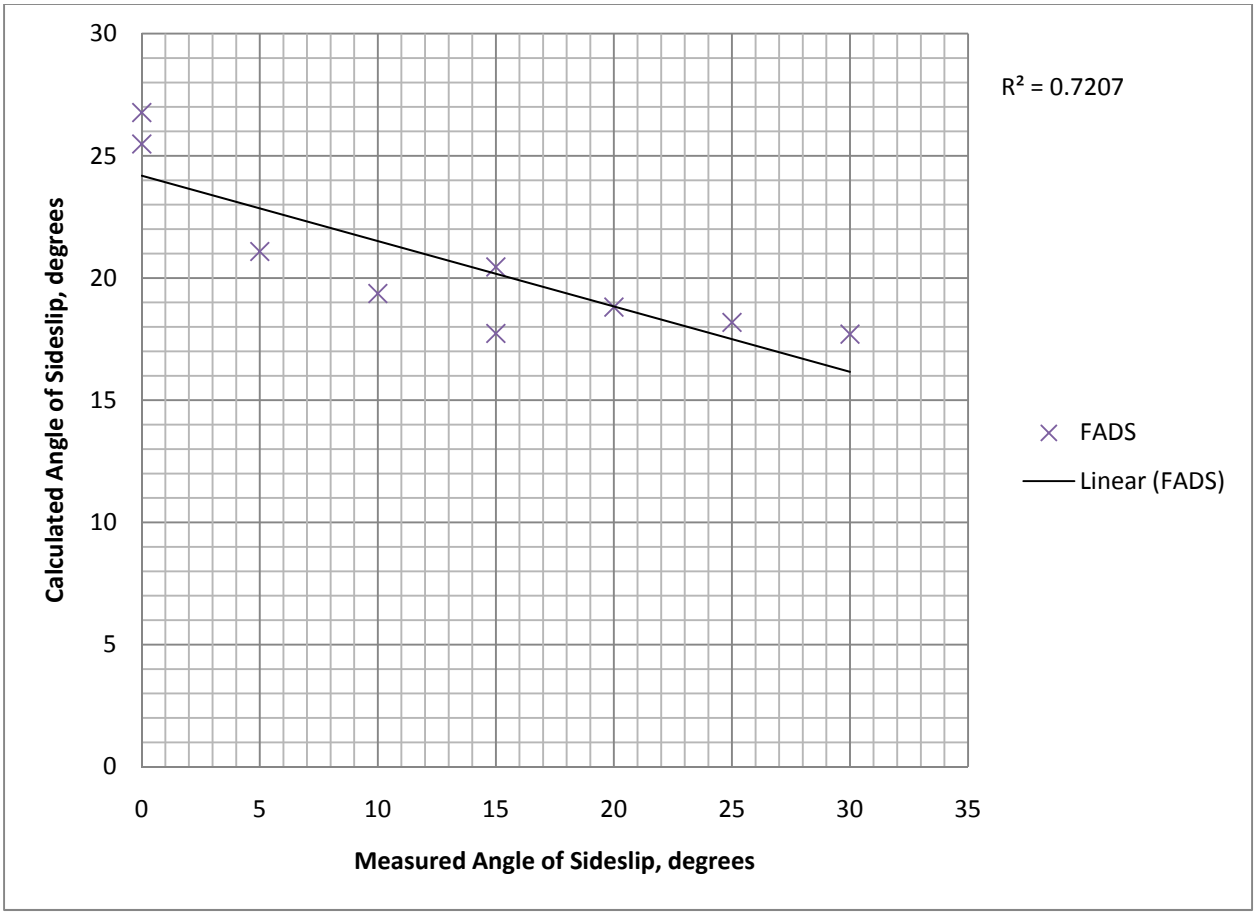

Figure B.11: Calculated angle of sideslip vs. measured angle of sideslip, positive values, 45° probe head, FADS method.

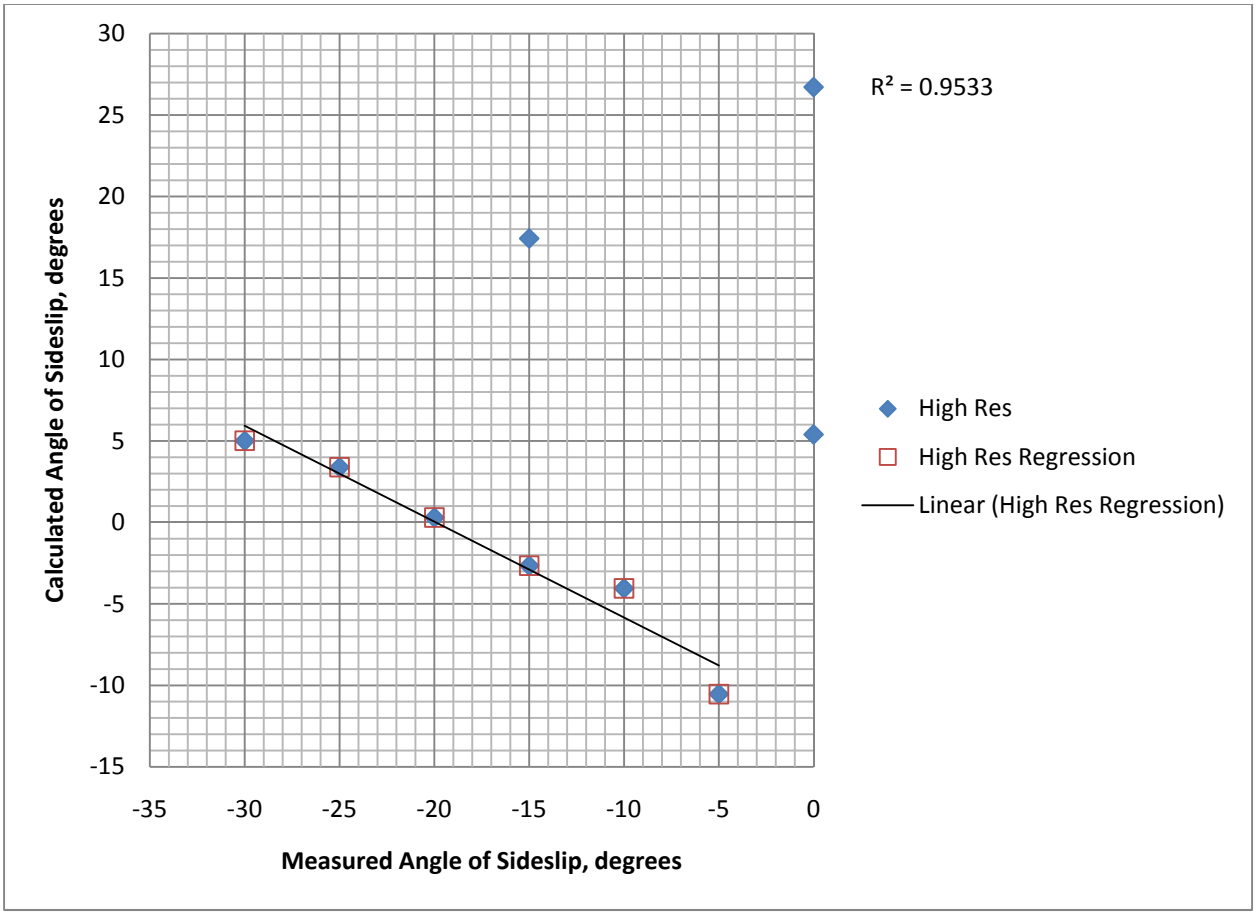

Figure B.12: Calculated angle of sideslip vs. measured angle of sideslip, negative values, 45° probe head, High Resolution method.

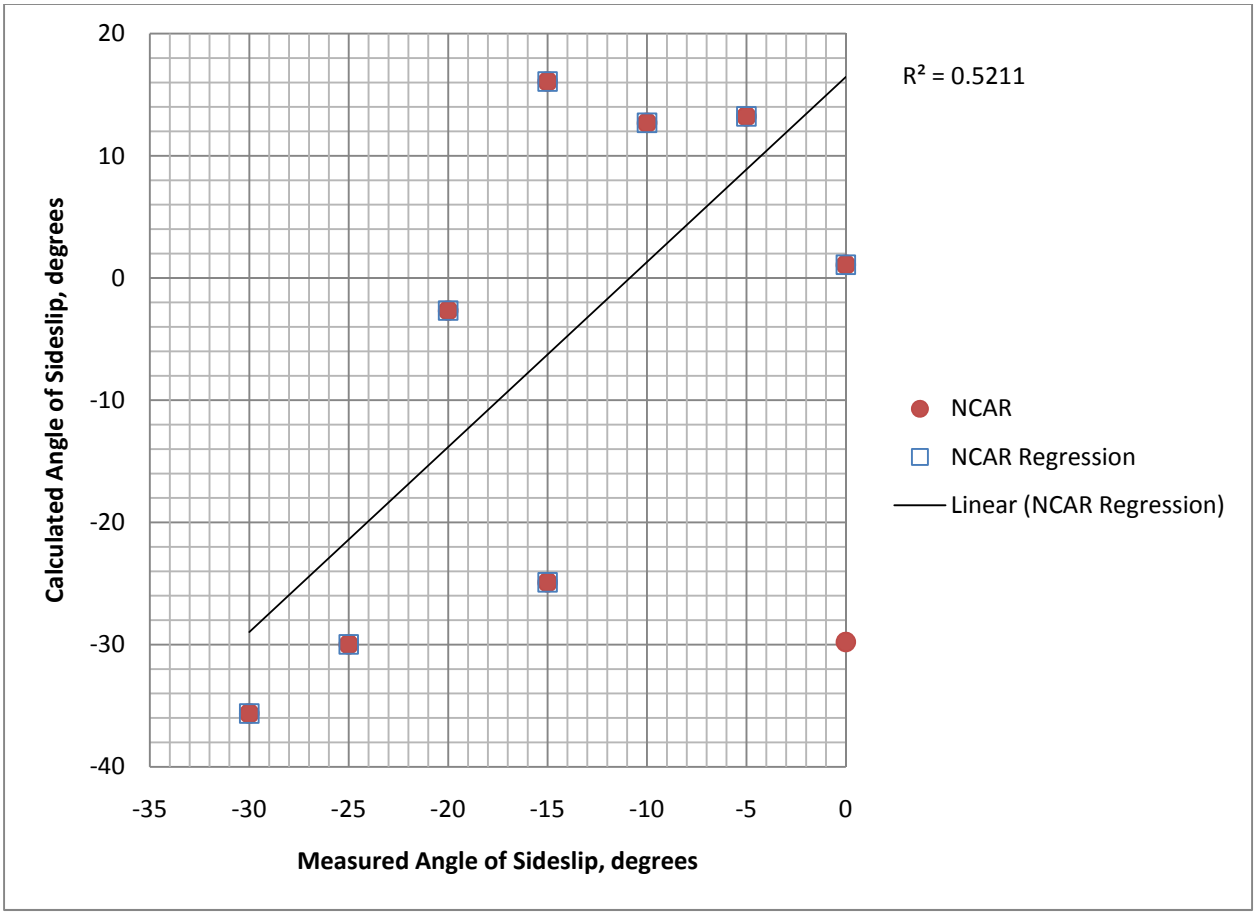

Figure B.13: Calculated angle of sideslip vs. measured angle of sideslip, negative values, 45° probe head, NCAR method.

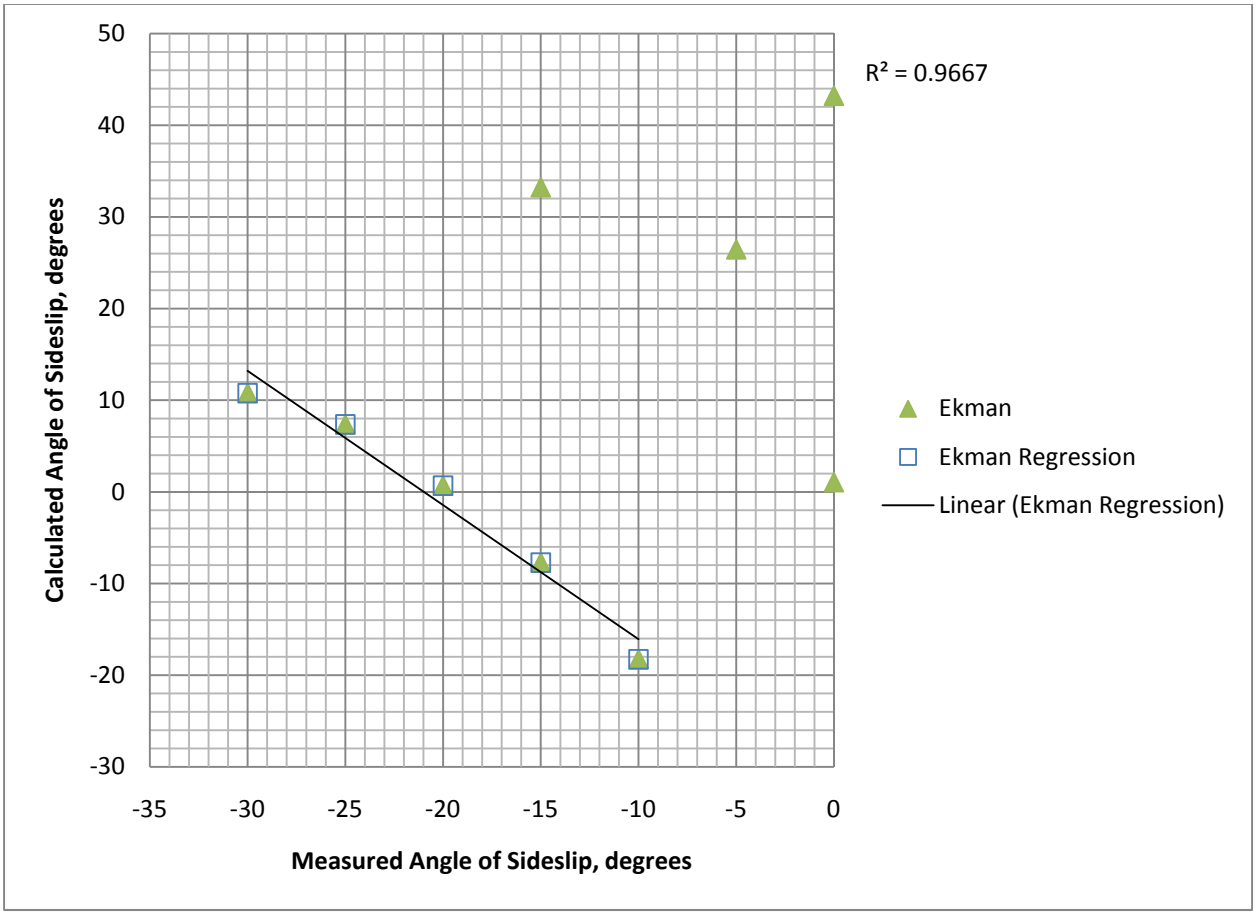

Figure B.14: Calculated angle of sideslip vs. measured angle of sideslip, negative values, 45° probe head, Ekman method.

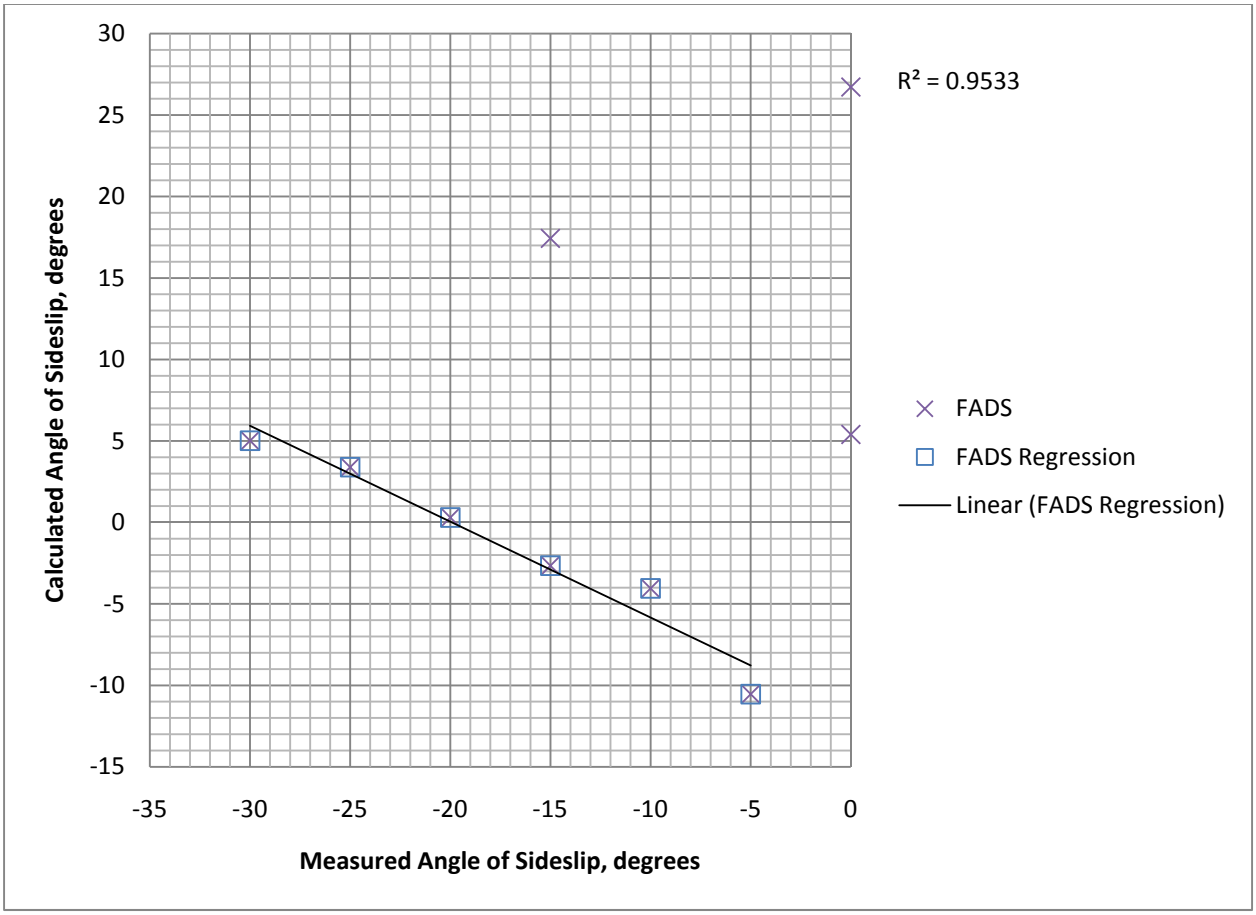

Figure B.15: Calculated angle of sideslip vs. measured angle of sideslip, negative values, 45° probe head, FADS method.

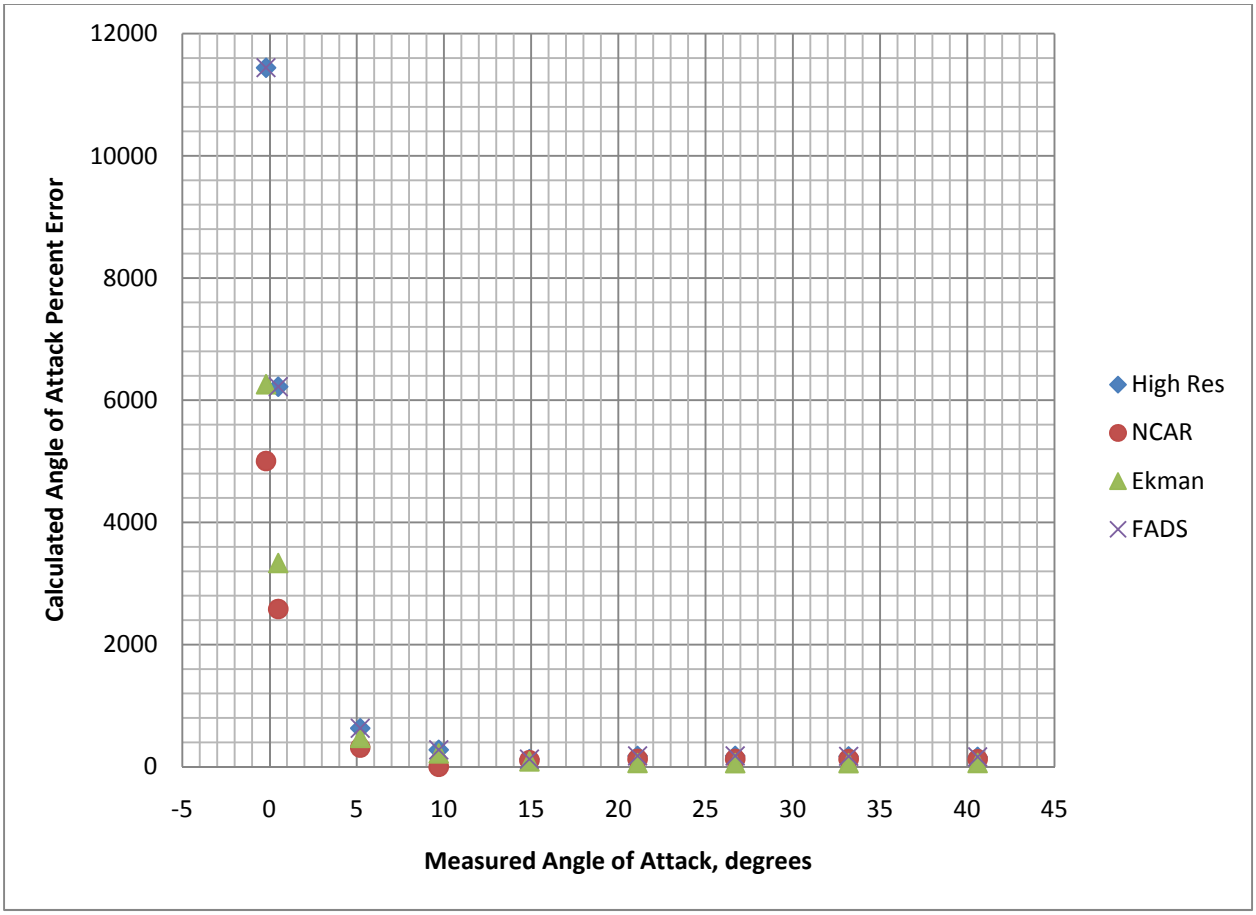

Figure B.16: Calculated angle of attack percent error vs. positive measured angle of attack, 41.8° head.

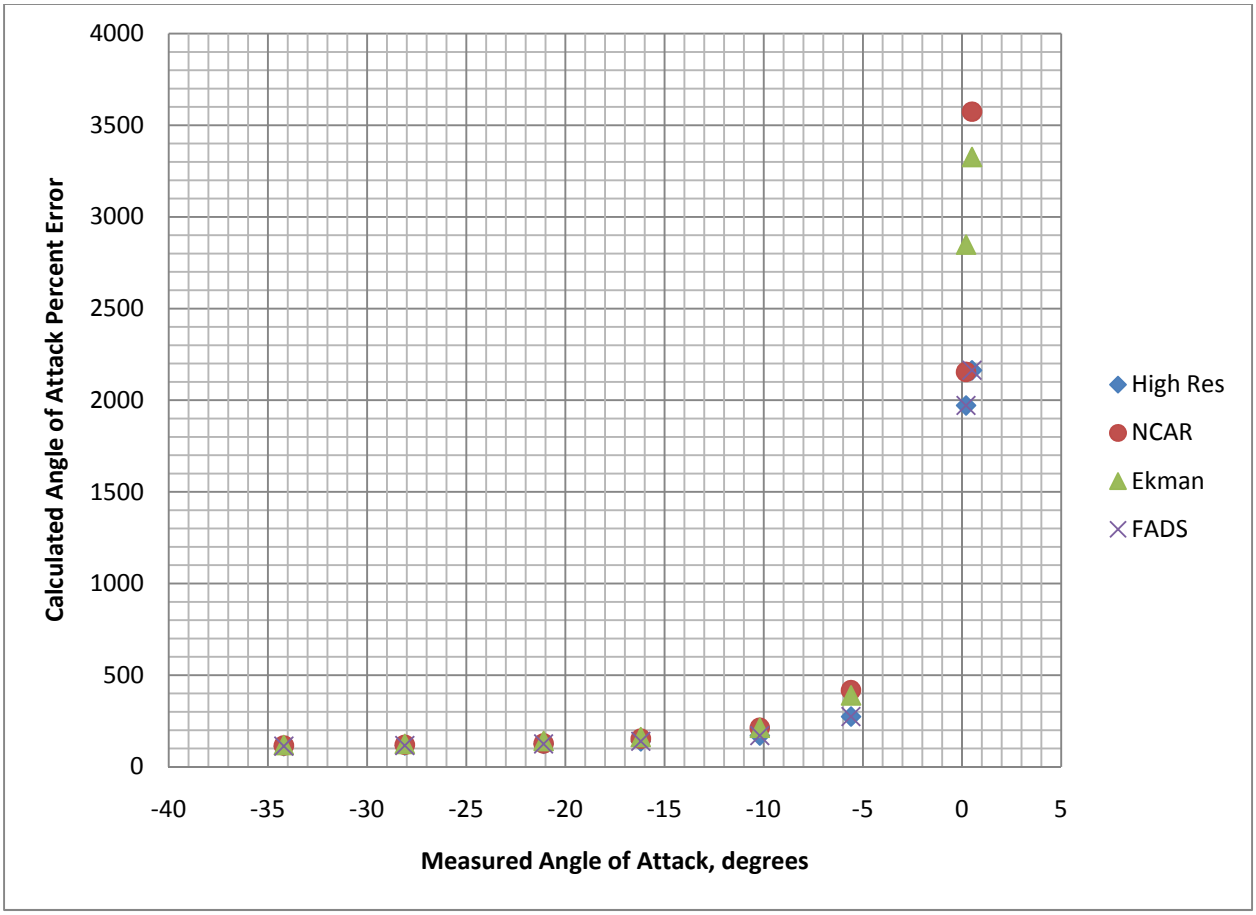

Figure B.17: Calculated angle of attack percent error vs. negative measured angle of attack, 41.8° head.

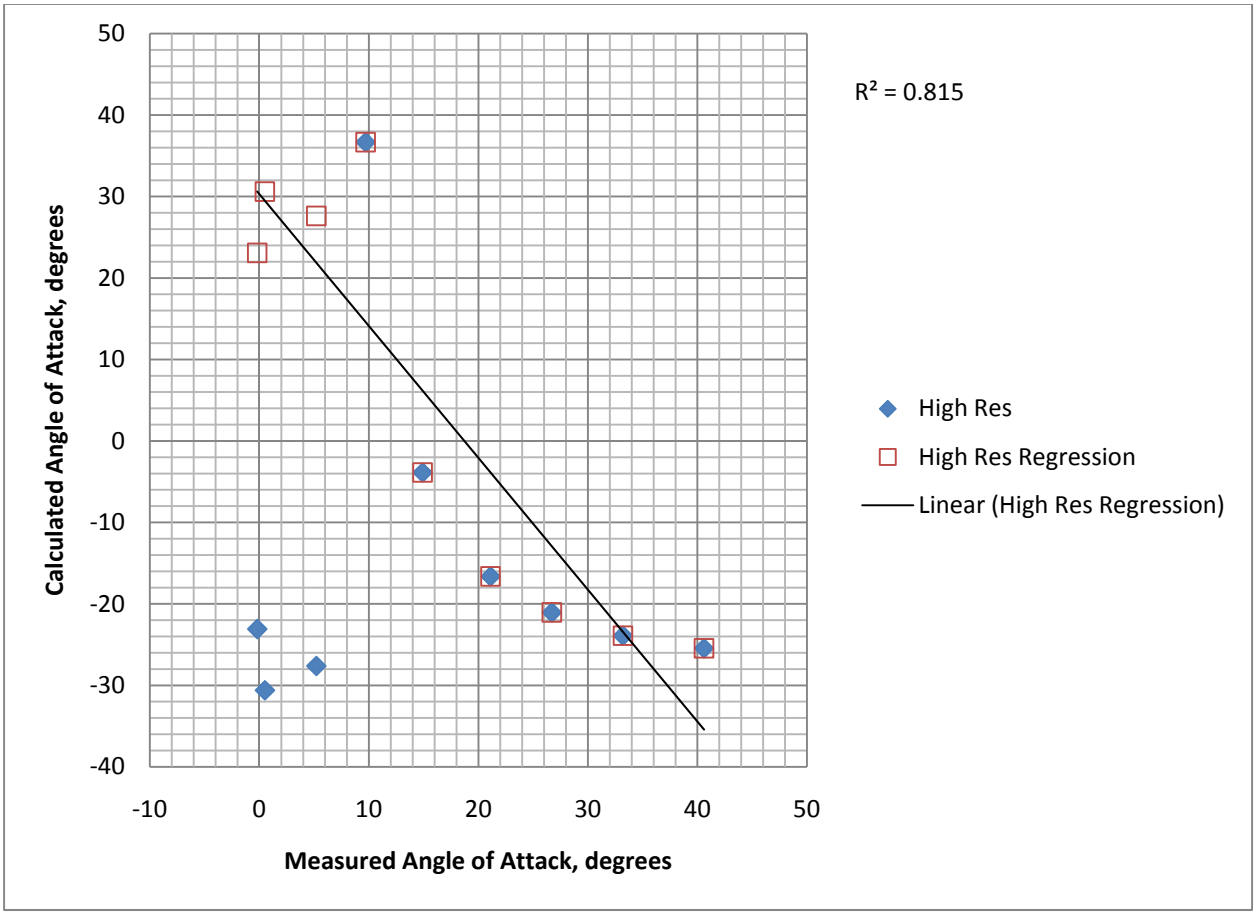

Figure B.18: Calculated angle of attack vs. positive measured angle of attack, 41.8° head, High Resolution method.

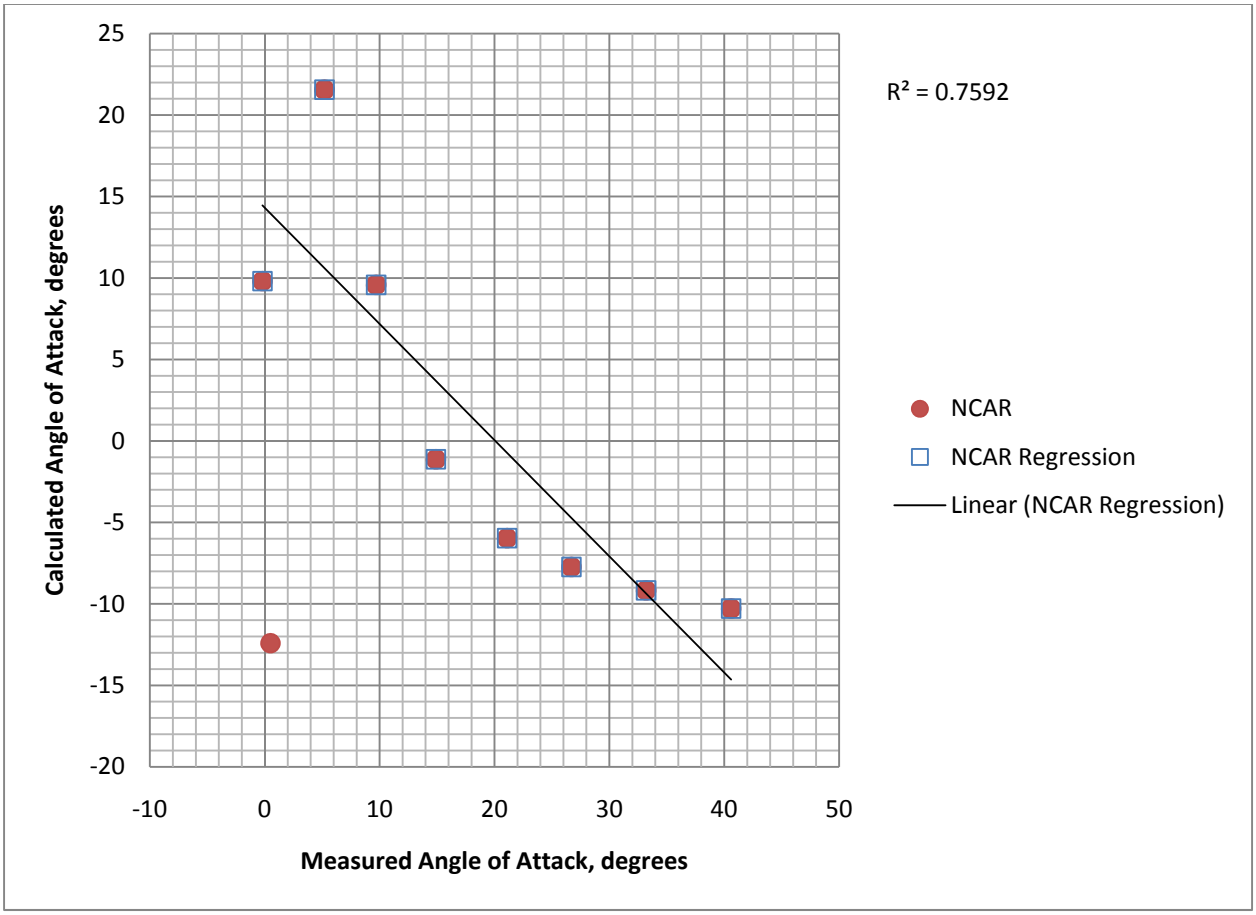

Figure B.19: Calculated angle of attack vs. positive measured angle of attack, 41.8° head, NCAR method.

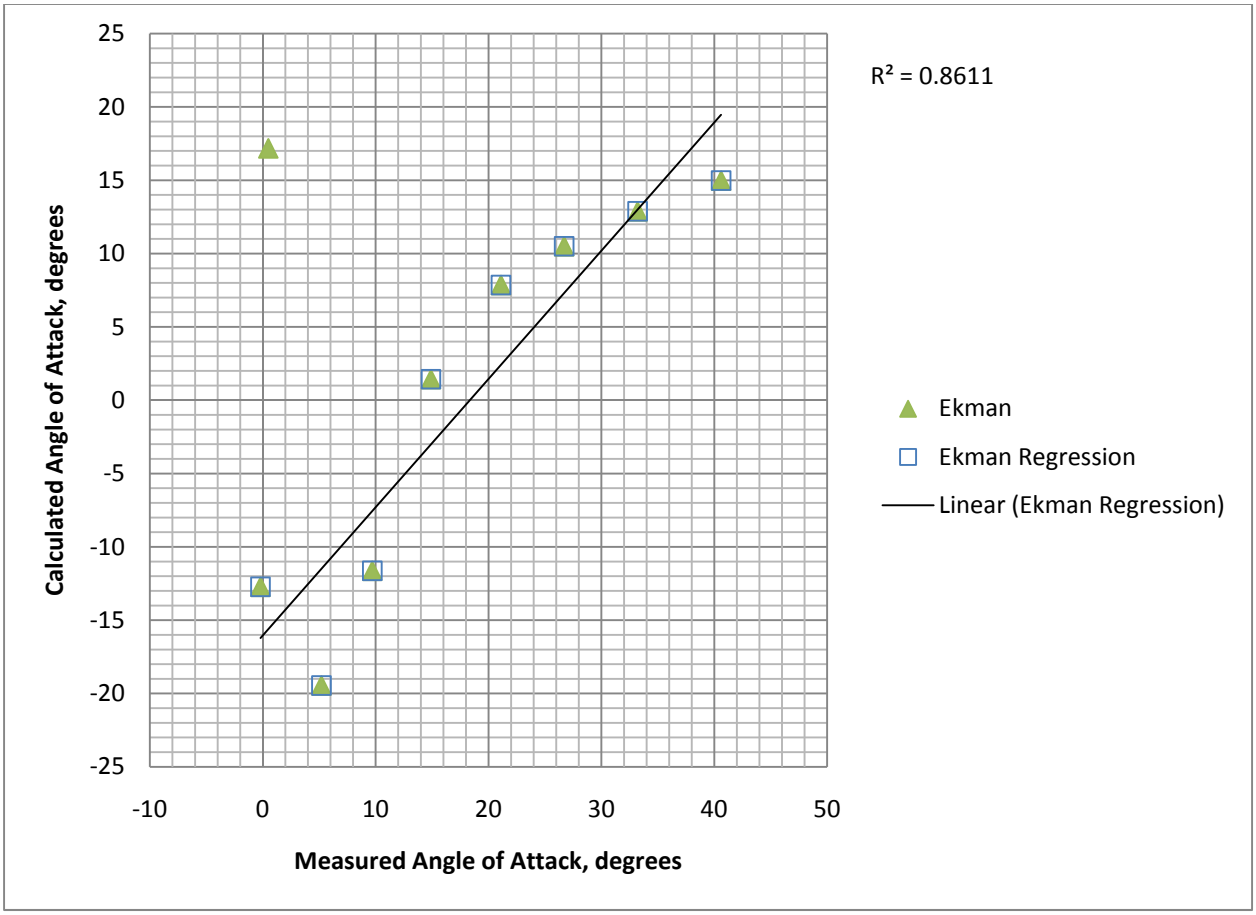

Figure B.20: Calculated angle of attack vs. positive measured angle of attack, 41.8° head, Ekman method.

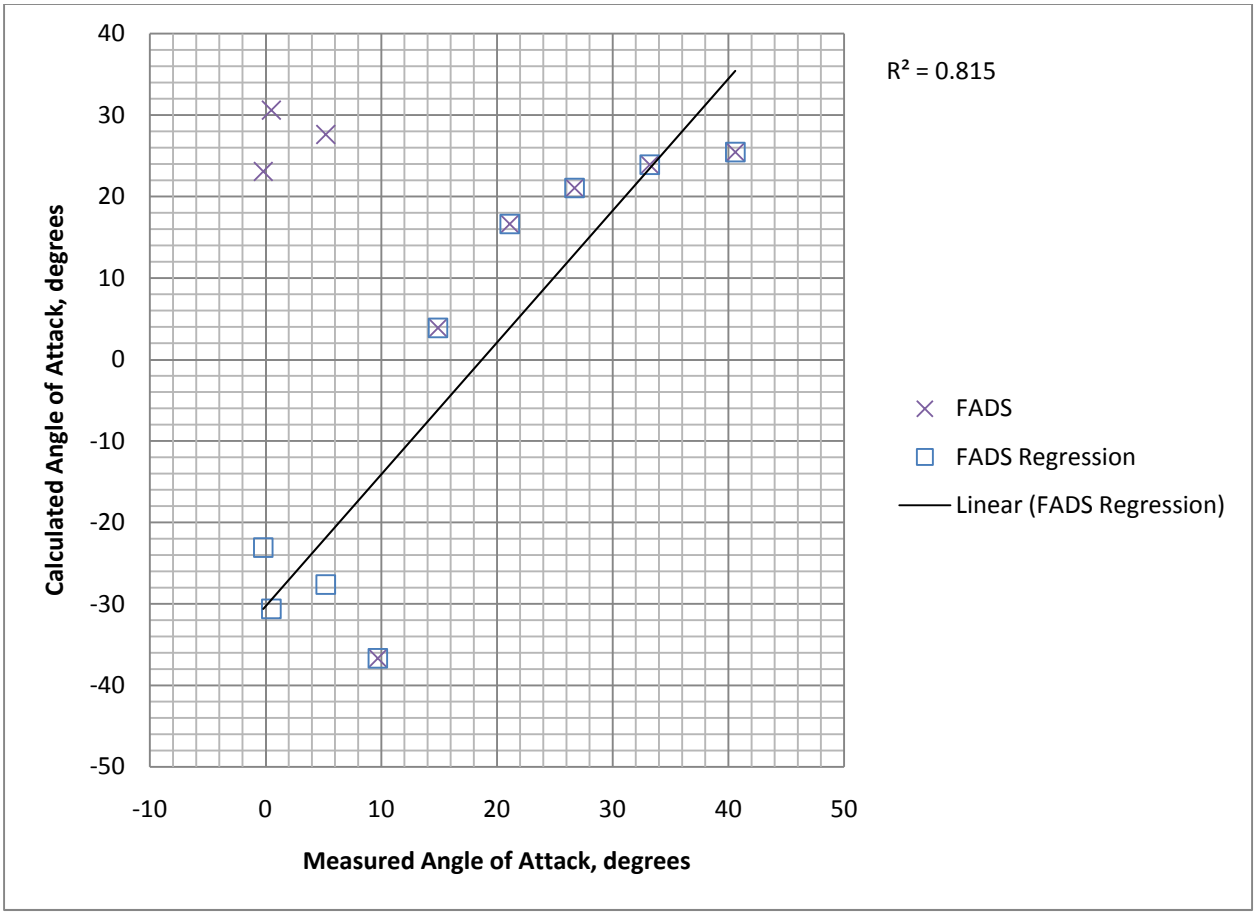

Figure B.21: Calculated angle of attack vs. positive measured angle of attack, 41.8° head, FADS method.

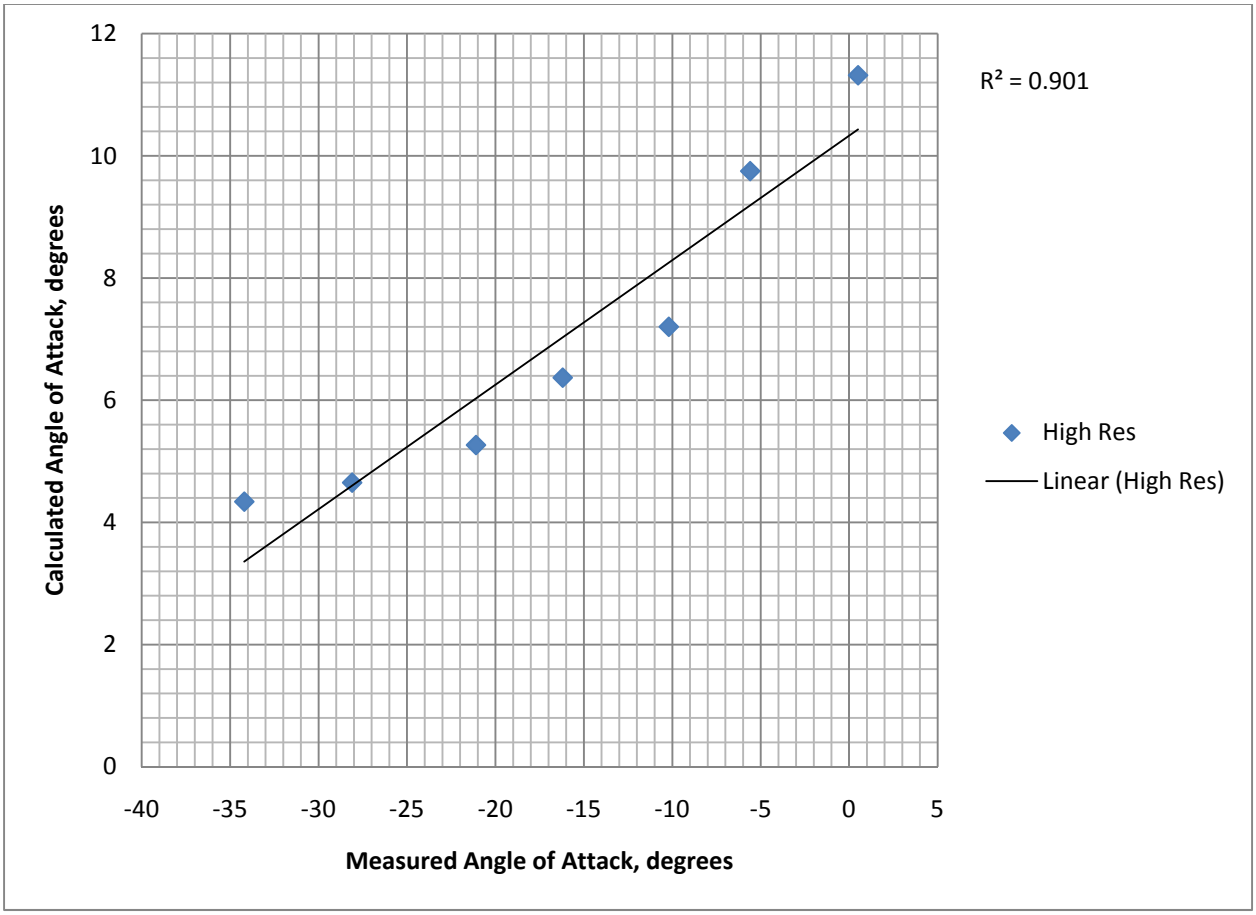

Figure B.22: Calculated angle of attack vs. negative measured angle of attack, 41.8° probe head, High Resolution method.

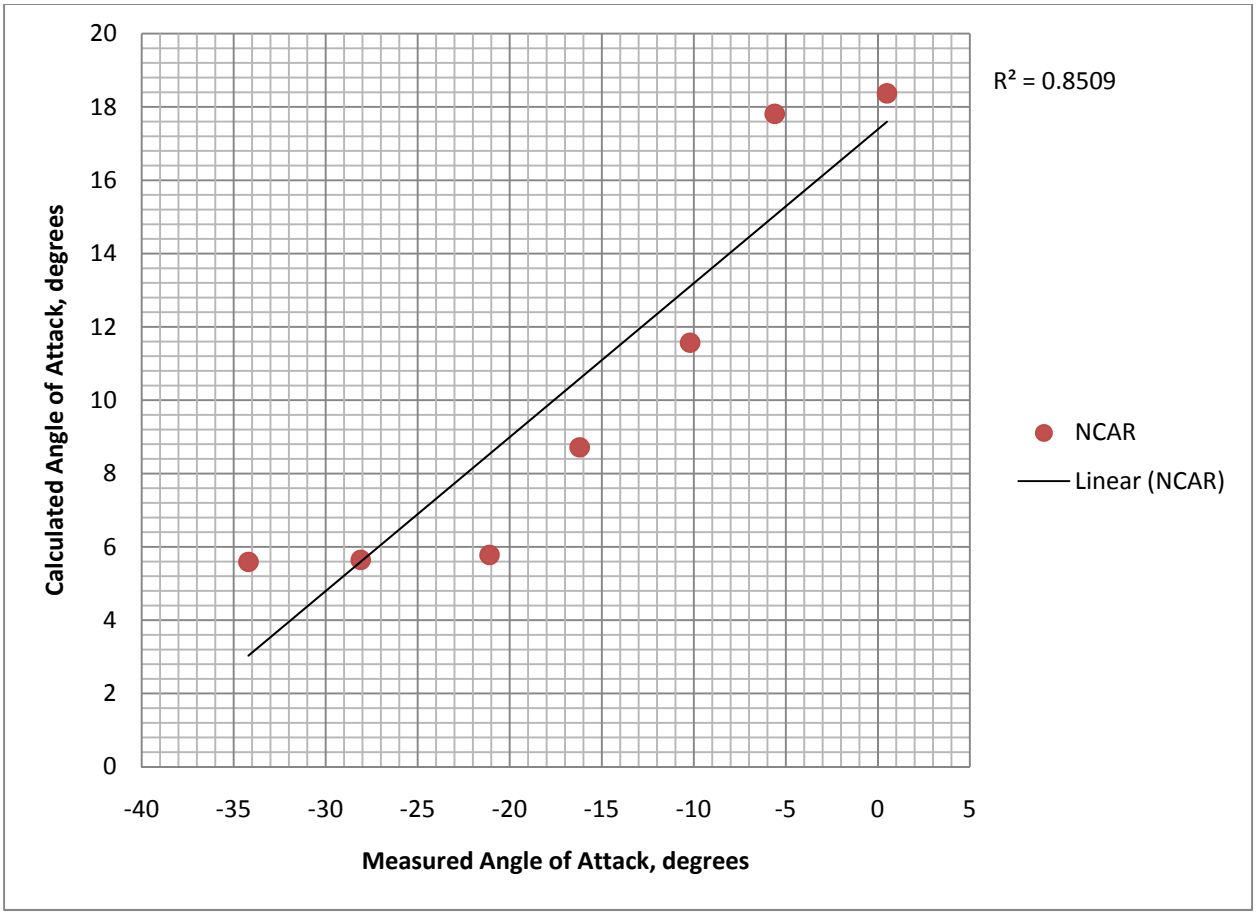

Figure B.23: Calculated angle of attack vs. negative measured angle of attack, 41.8° probe head, NCAR method.

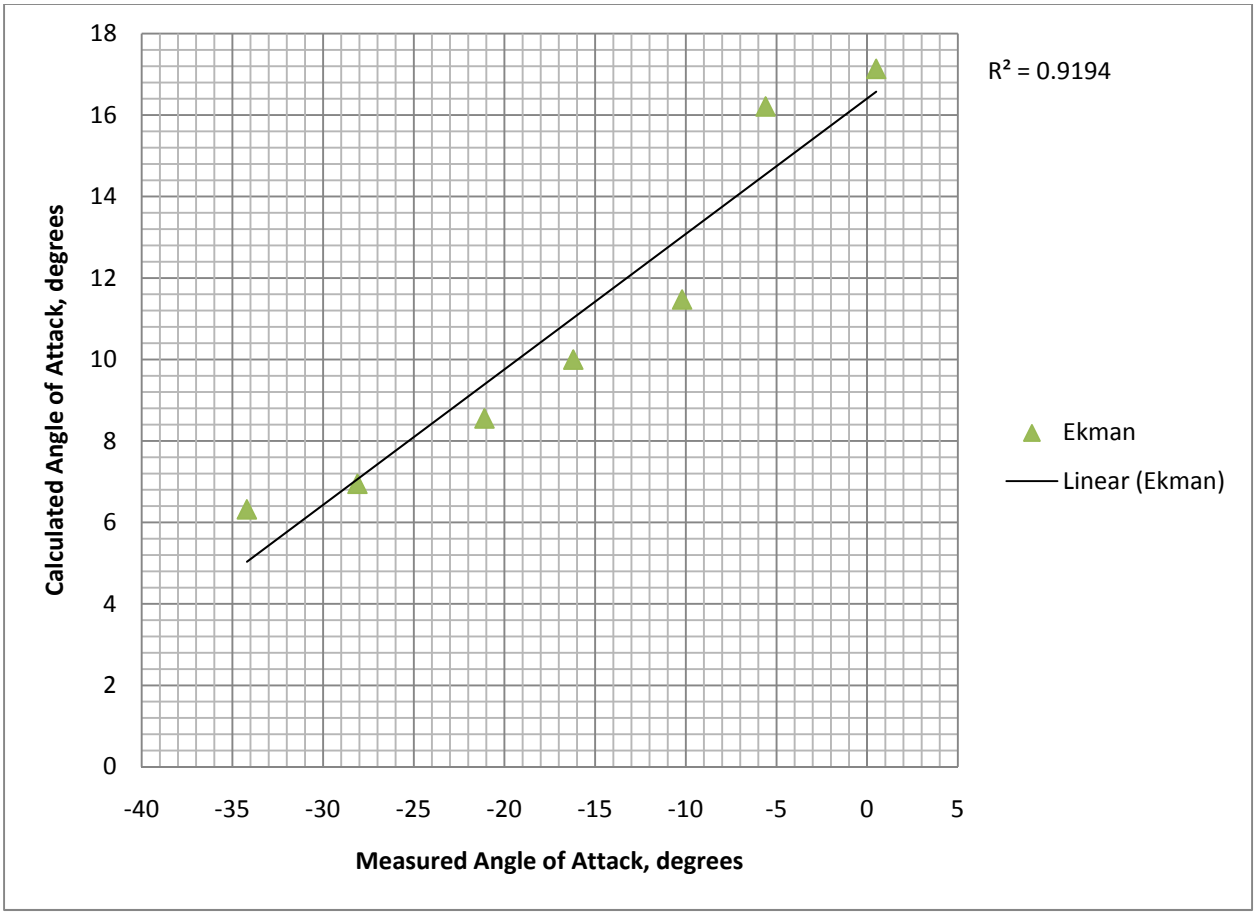

Figure B.24: Calculated angle of attack vs. negative measured angle of attack, 41.8° probe head, Ekman method.

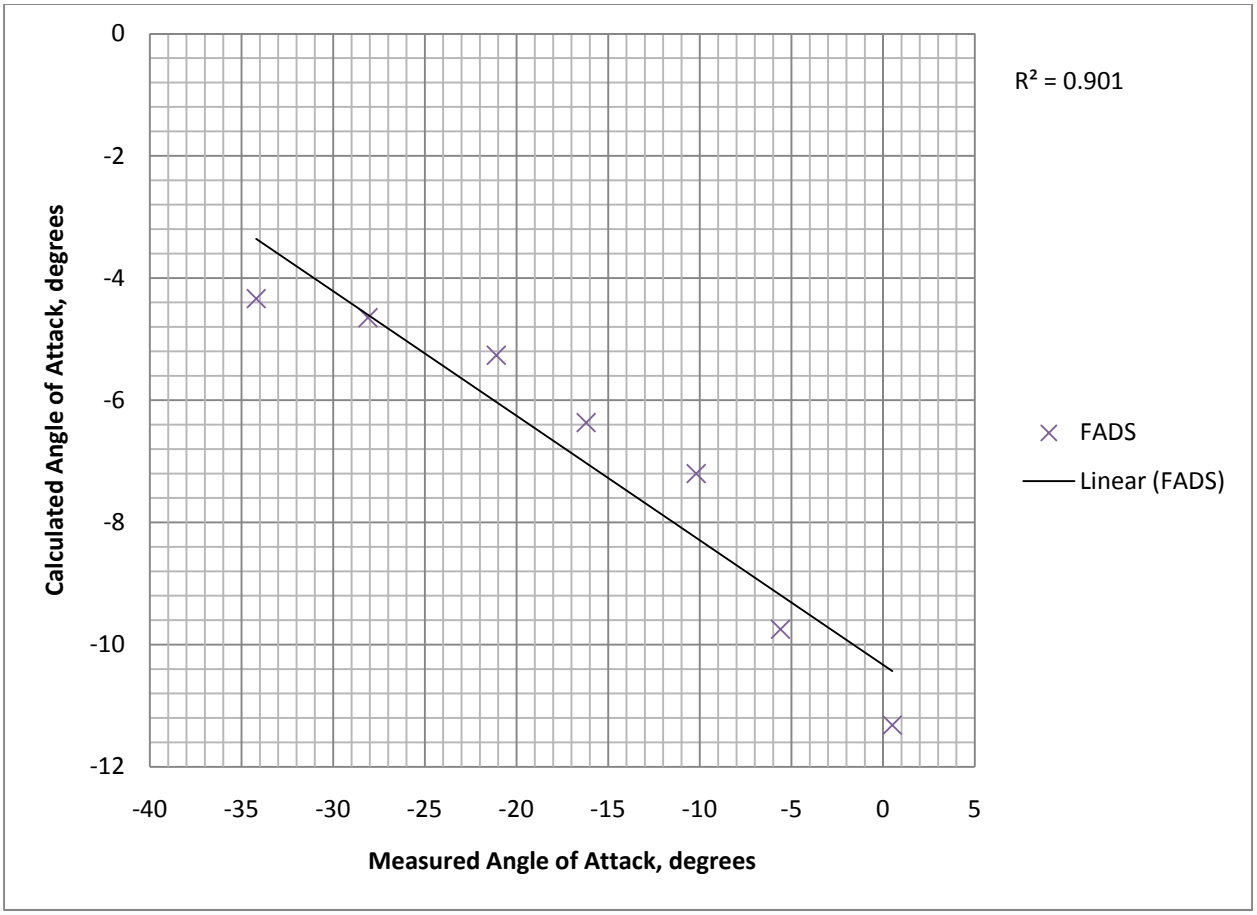

Figure B.25: Calculated angle of attack vs. negative measured angle of attack values, 41.8° probe head, FADS method.

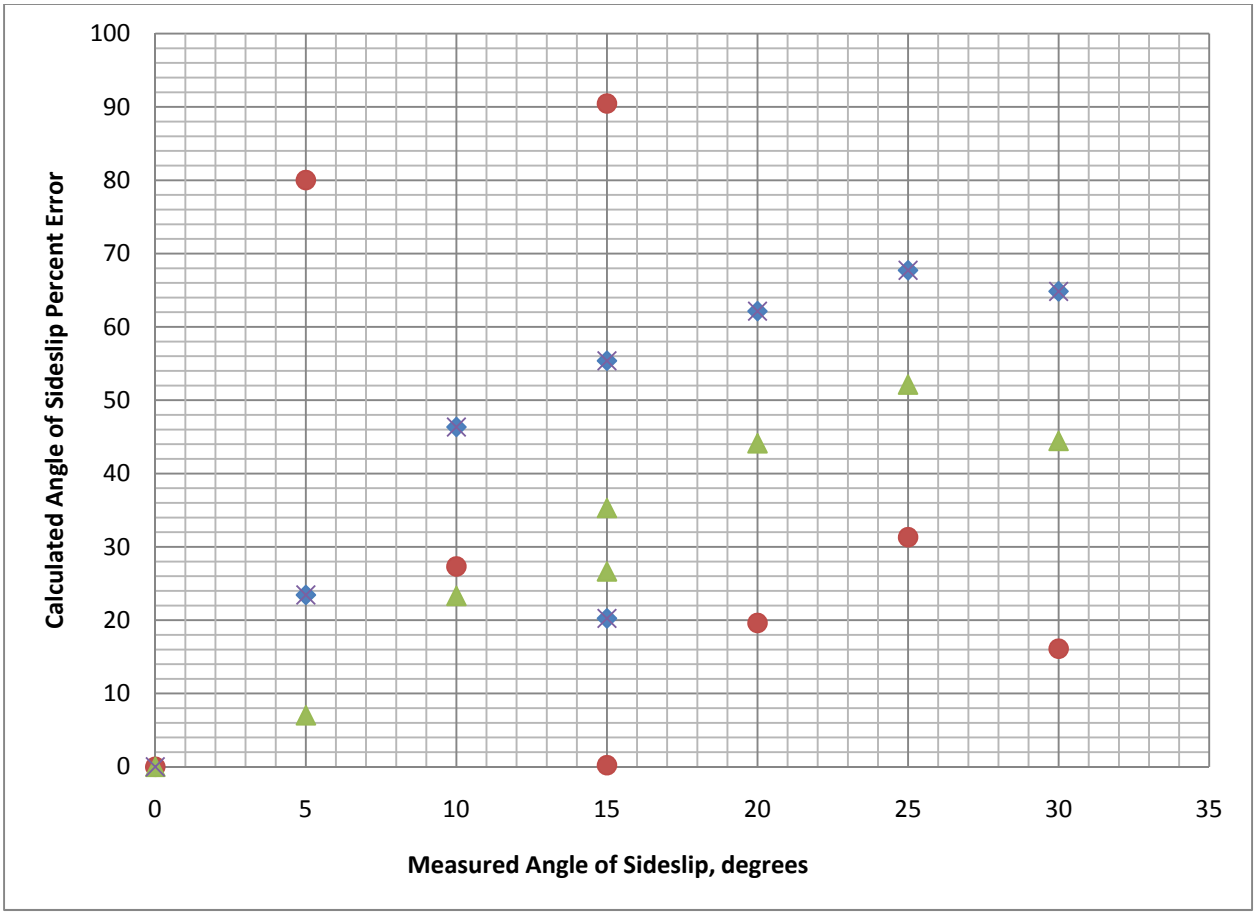

Figure B.26: Calculated angle of sideslip percent error vs. positive measured angle of sideslip values, 41.8° head.

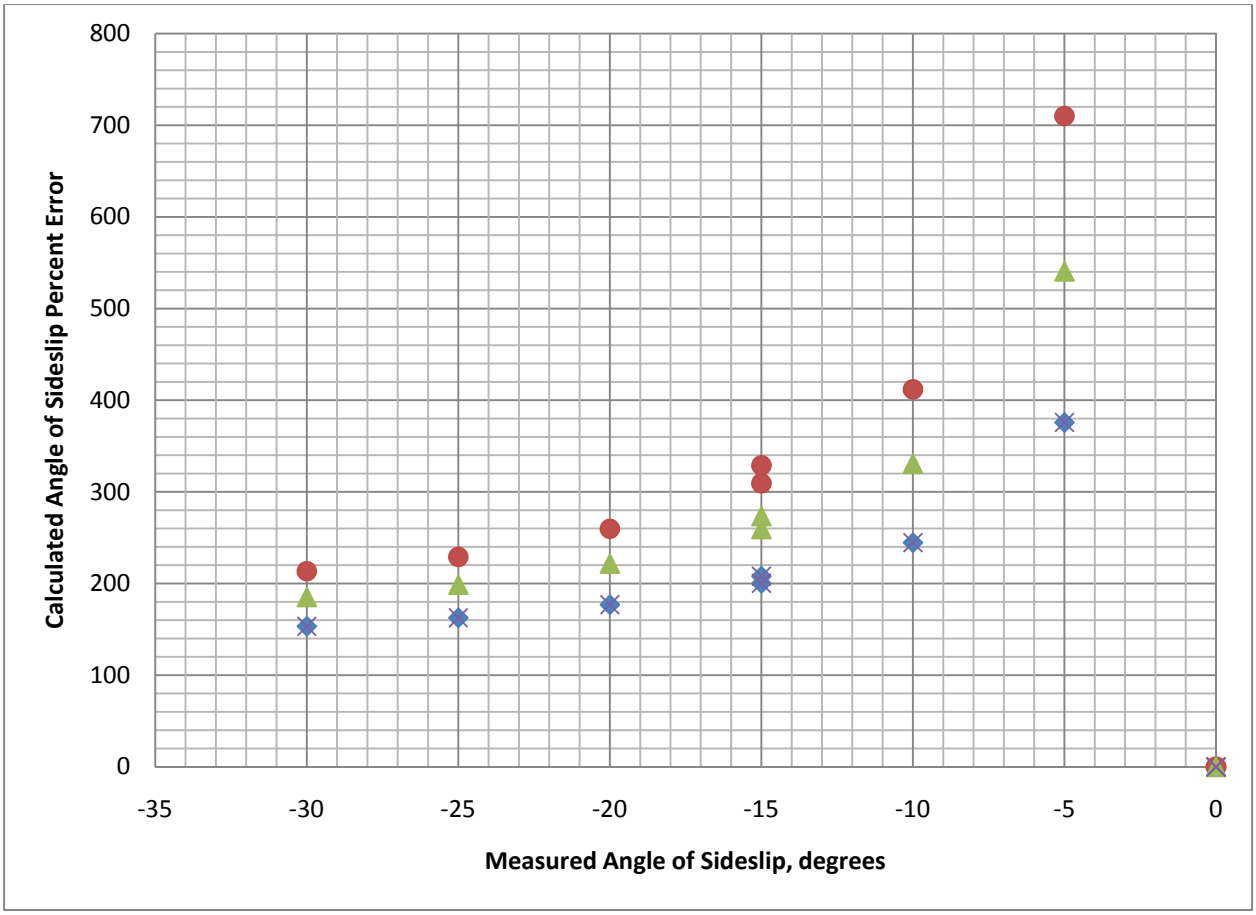

Figure B.27: Calculated angle of sideslip percent error vs. negative measured angle of sideslip values, 41.8° head.

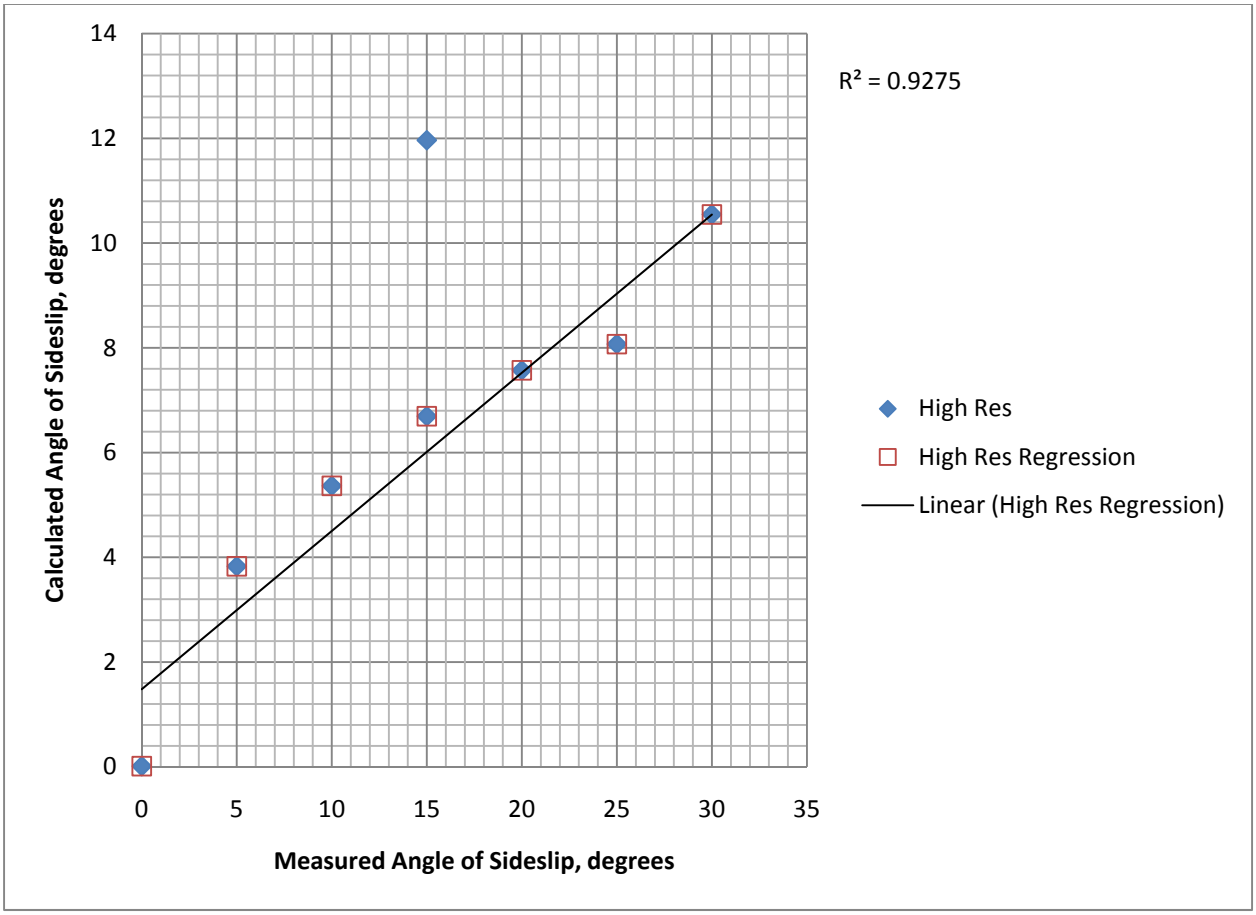

Figure B.28: Calculated angle of sideslip vs. positive measured angle of sideslip values, 41.8° probe head, High Resolution method.

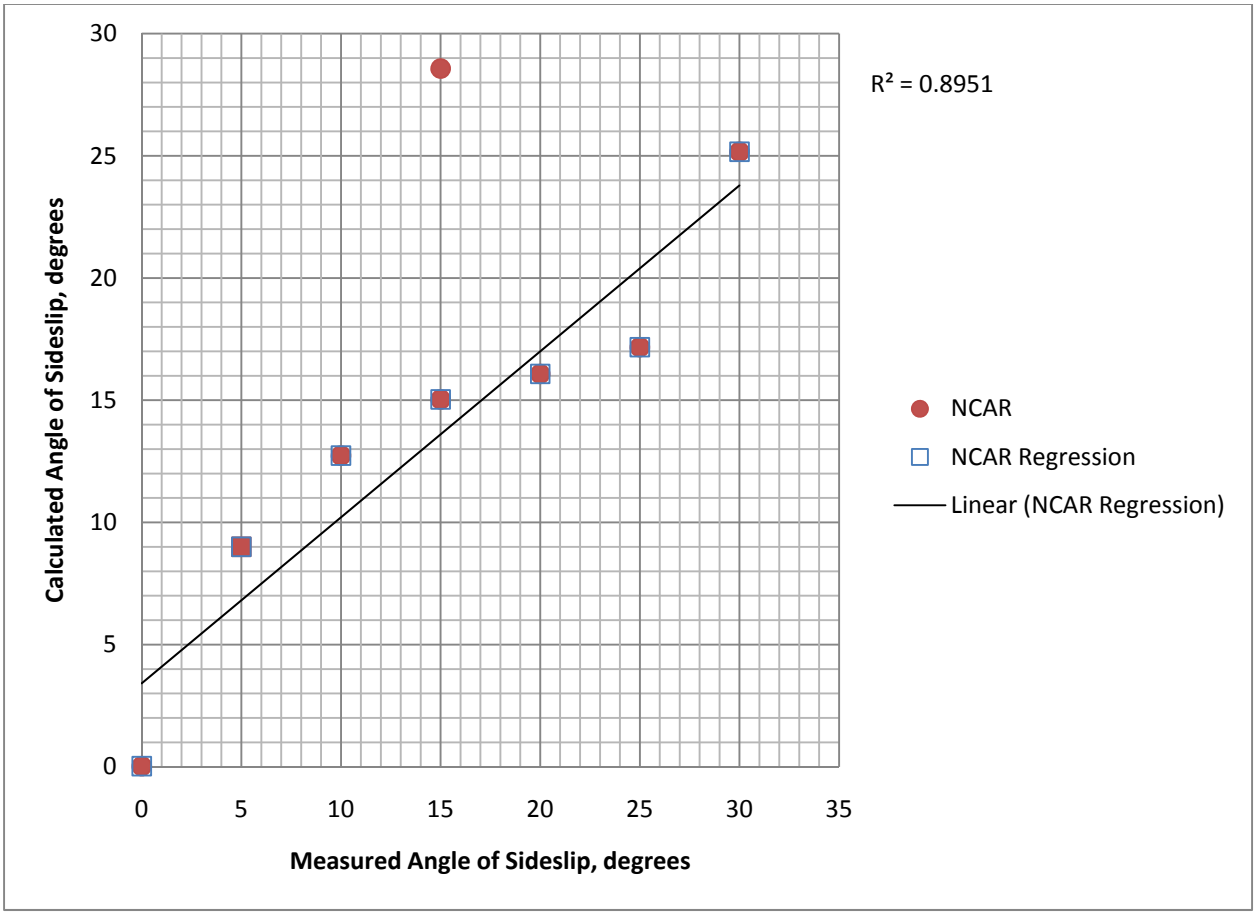

Figure B.29: Calculated angle of sideslip vs. positive measured angle of sideslip values, 41.8° probe head, NCAR method.

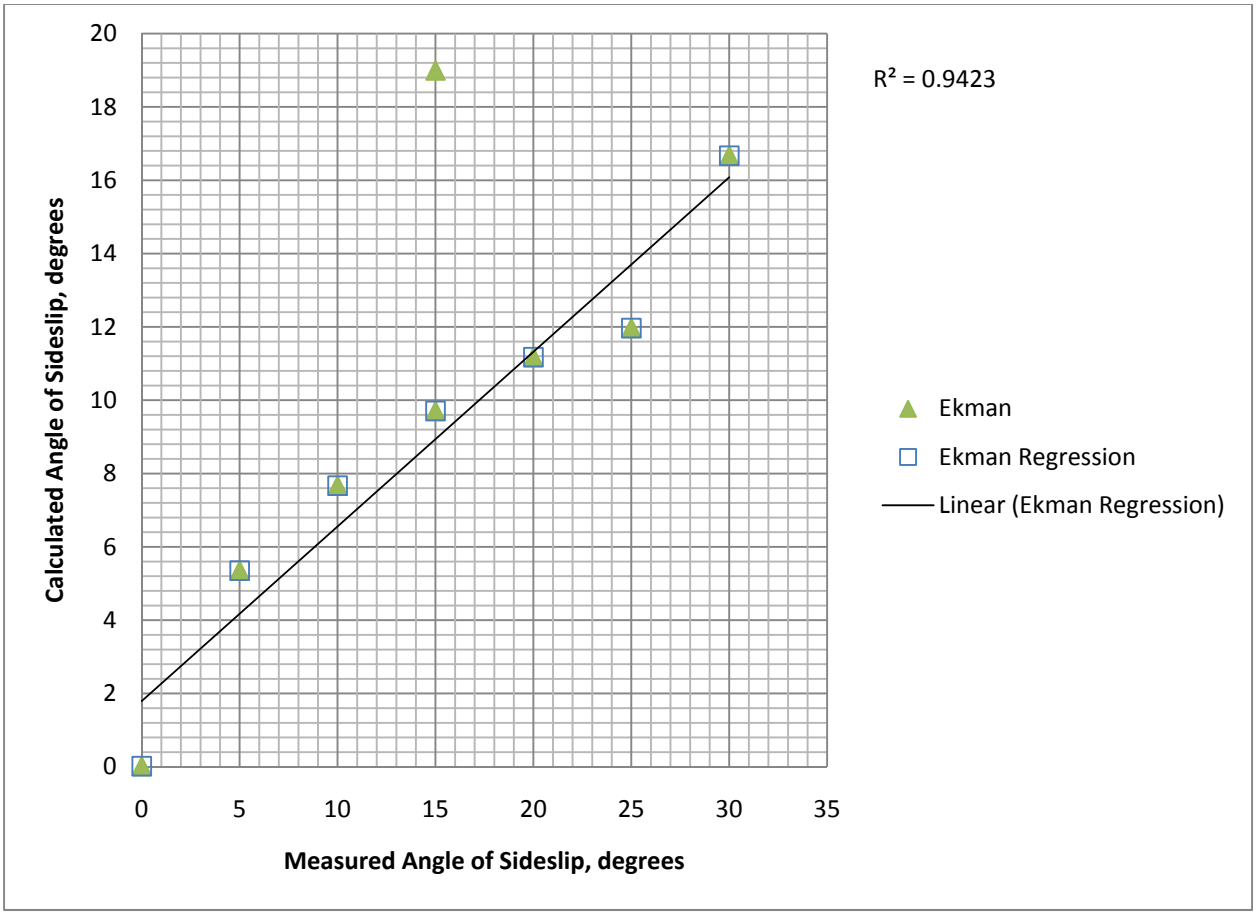

Figure B.30: Calculated angle of sideslip vs. positive measured angle of sideslip values, 41.8° probe head, Ekman method.

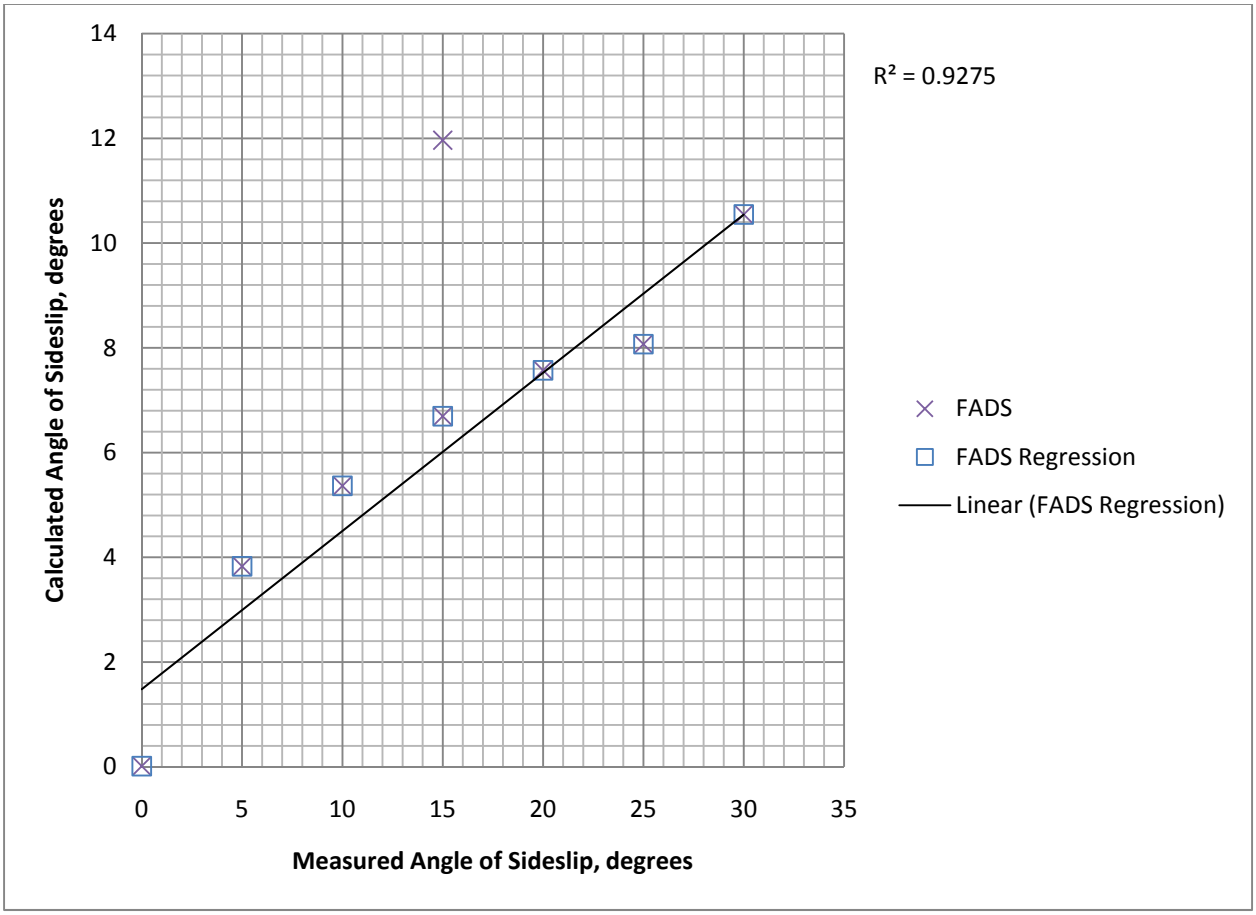

Figure B.31: Calculated angle of sideslip vs. positive measured angle of sideslip values, 41.8° probe head, FADS method.

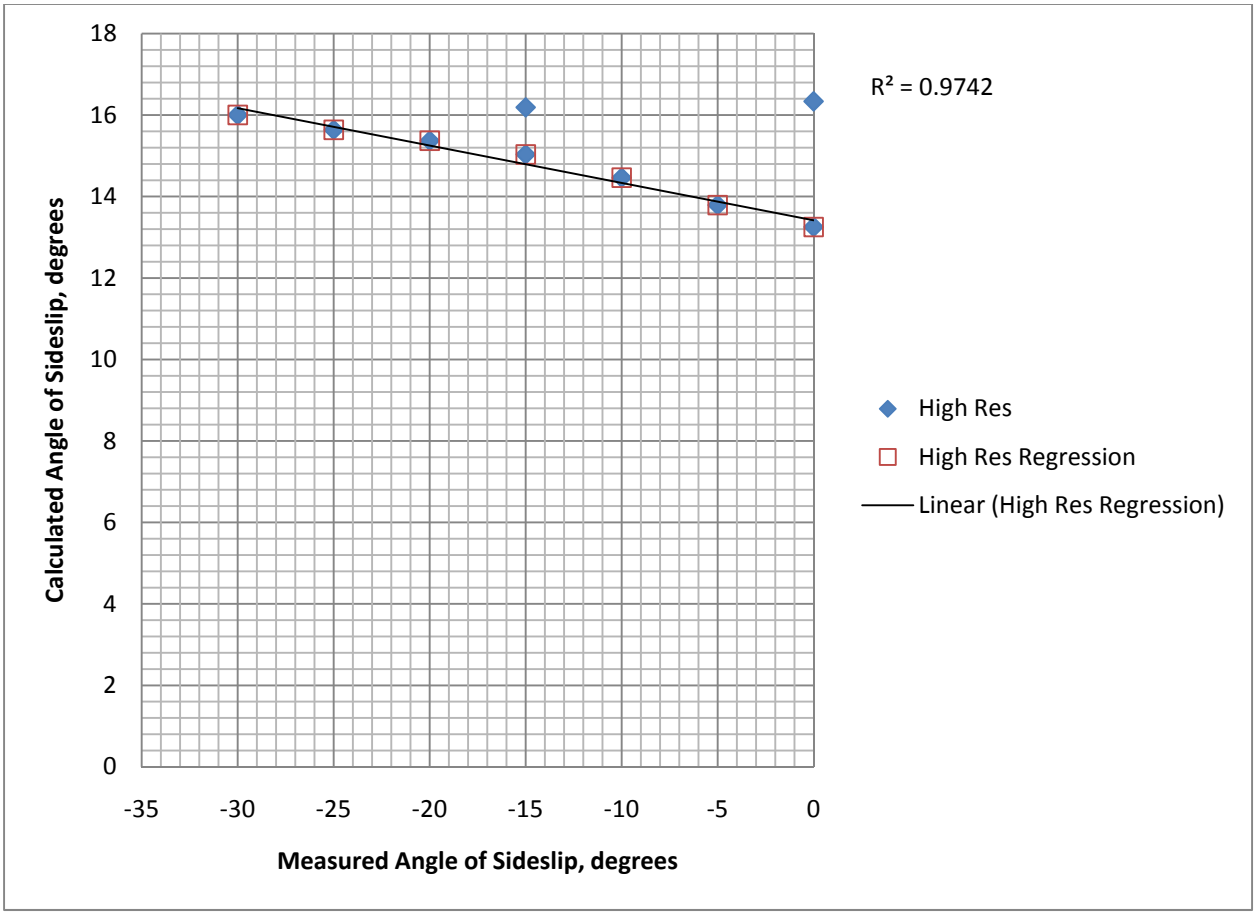

Figure B.32: Calculated angle of sideslip vs. negative measured angle of sideslip values, 41.8° probe head, High Resolution method.

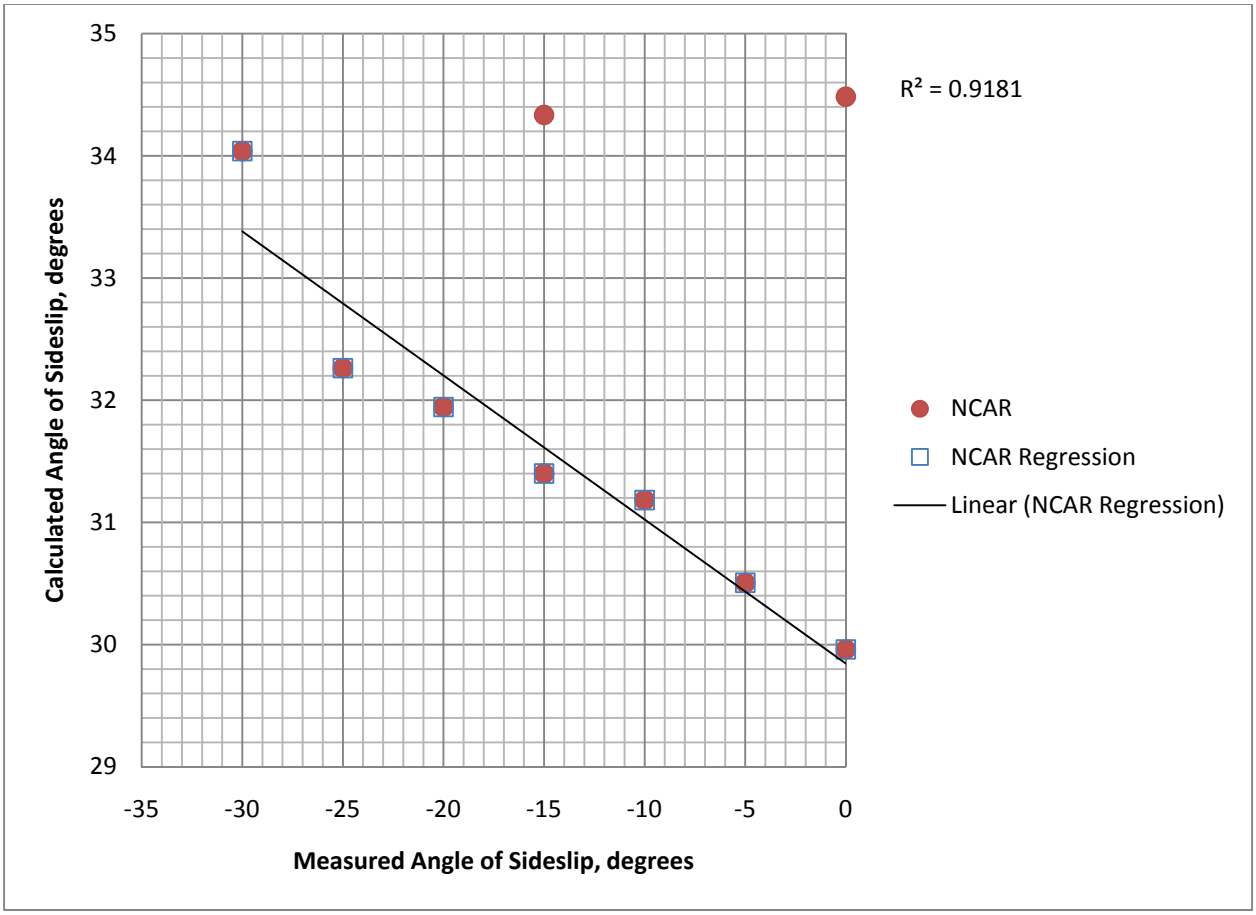

Figure B.33: Calculated angle of sideslip vs. negative measured angle of sideslip values, 41.8° probe head, NCAR method.

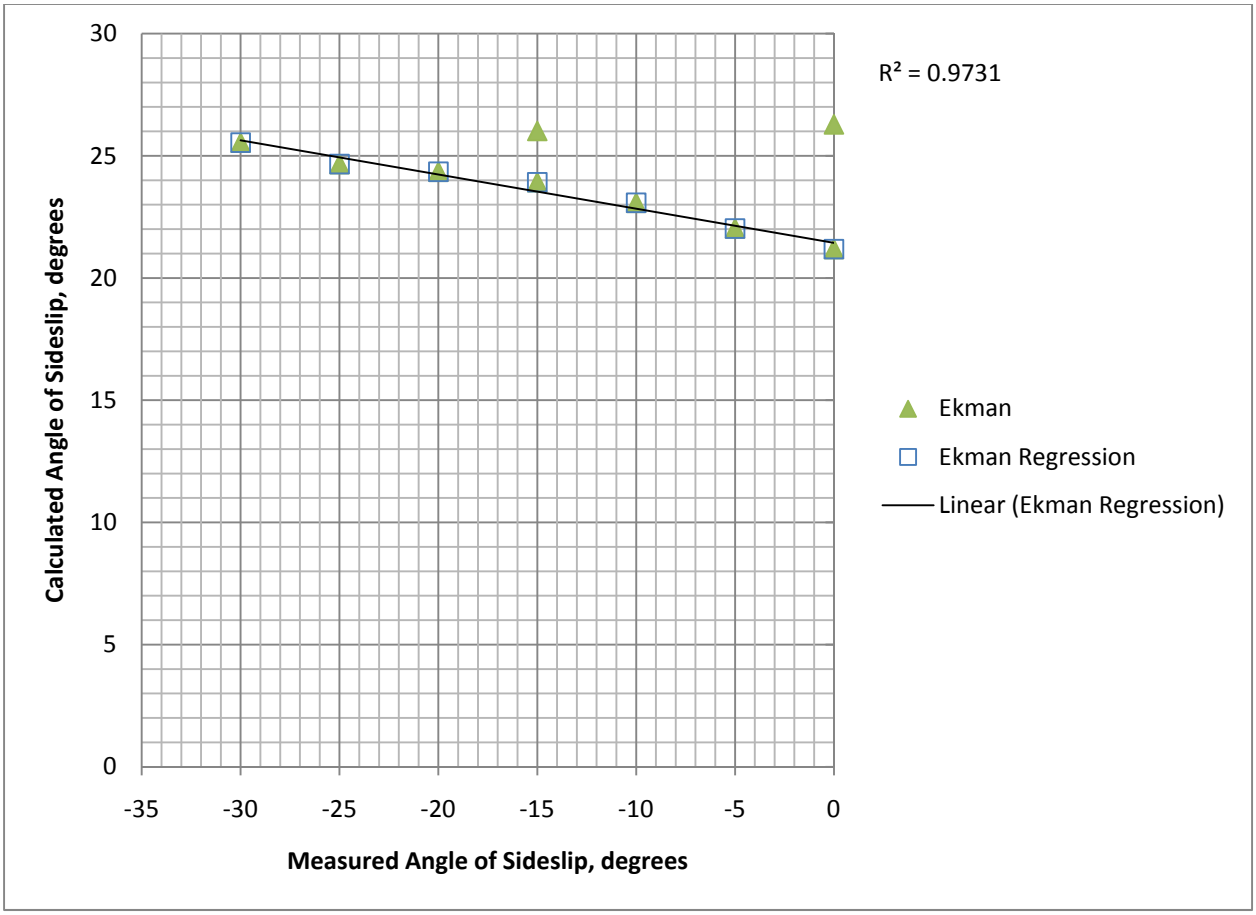

Figure B.34: Calculated angle of sideslip vs. negative measured angle of sideslip values, 41.8° probe head, Ekman method.

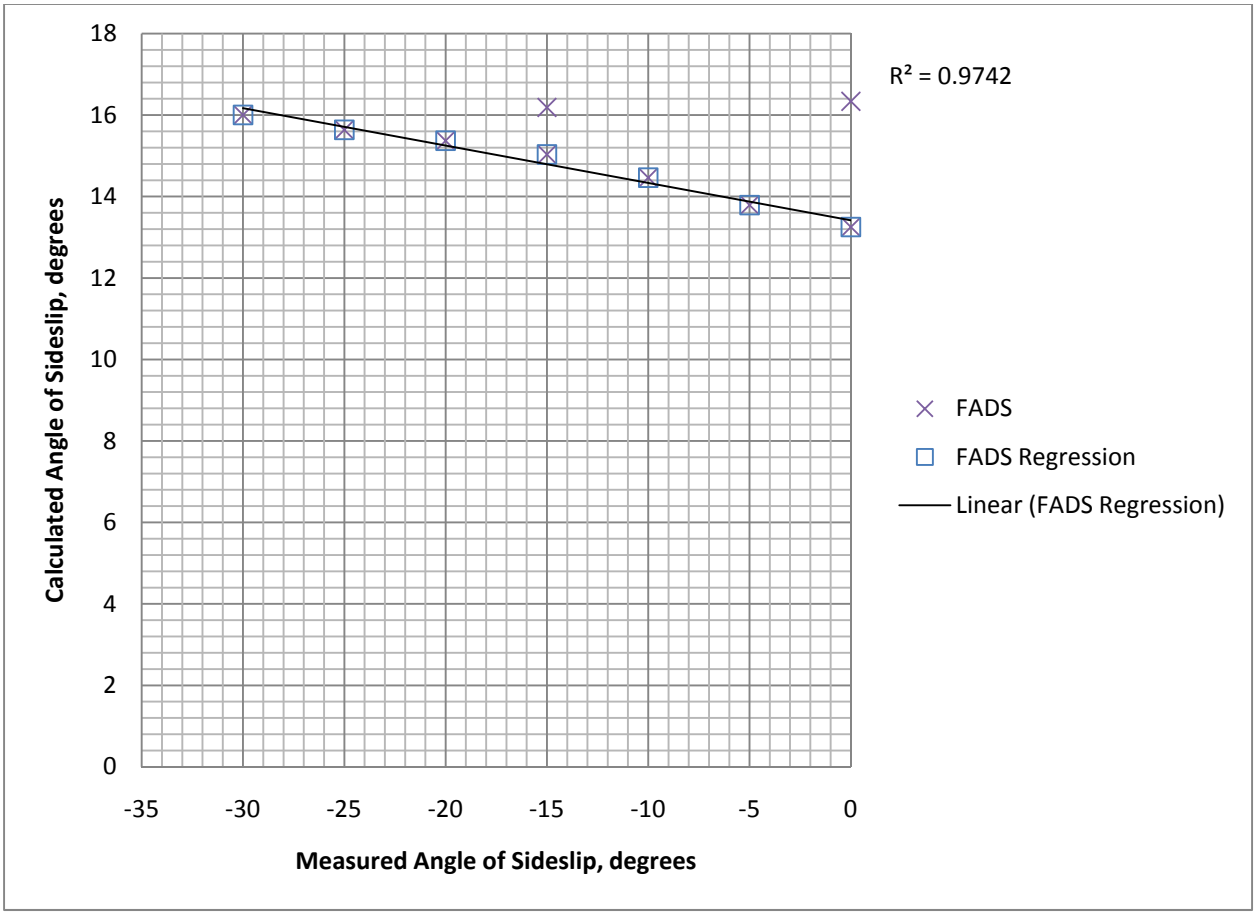

Figure B.35: Calculated angle of sideslip vs. negative measured angle of sideslip values, 41.8° probe head, FADS method.

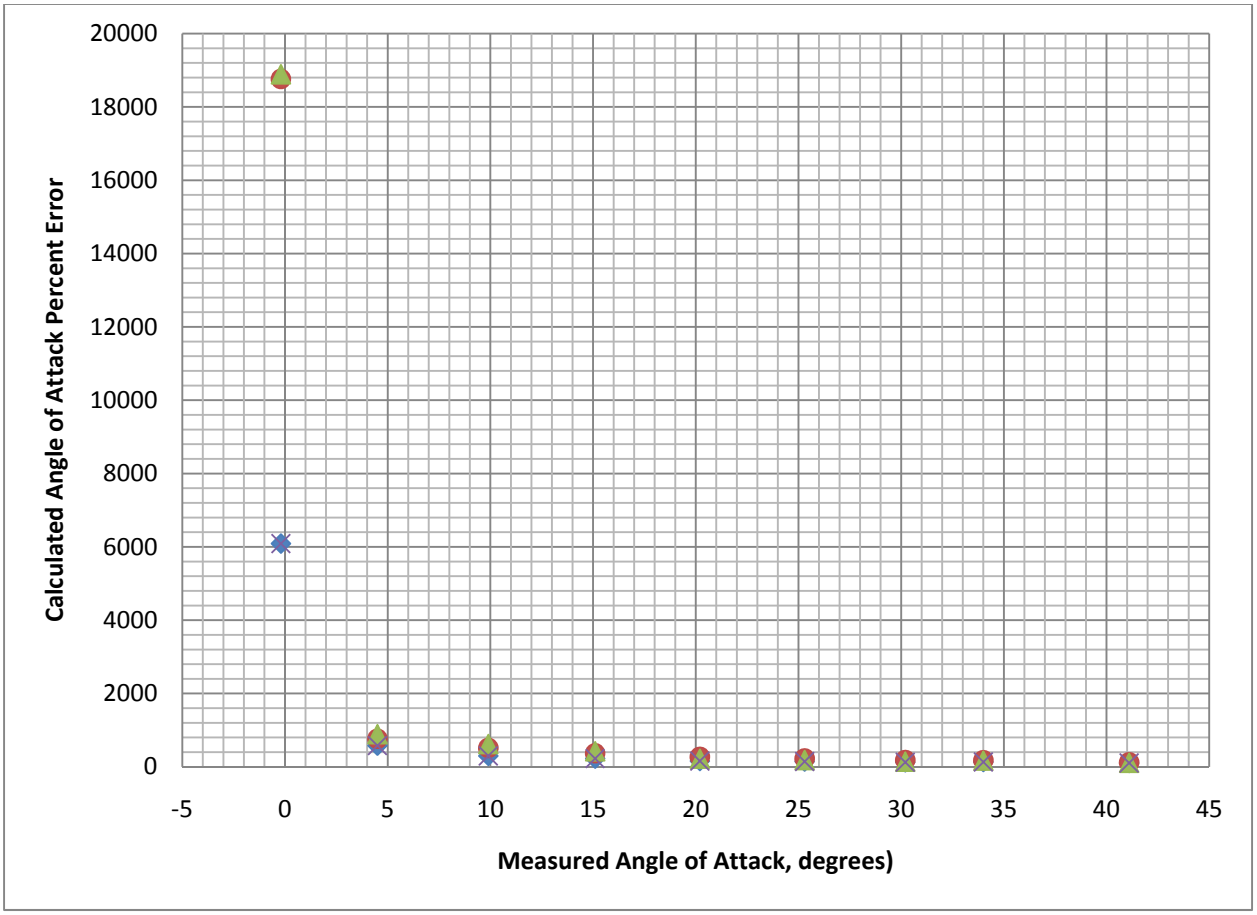

Figure B.36: Calculated angle of attack percent error vs. positive measured angle of attack values, FADS head.

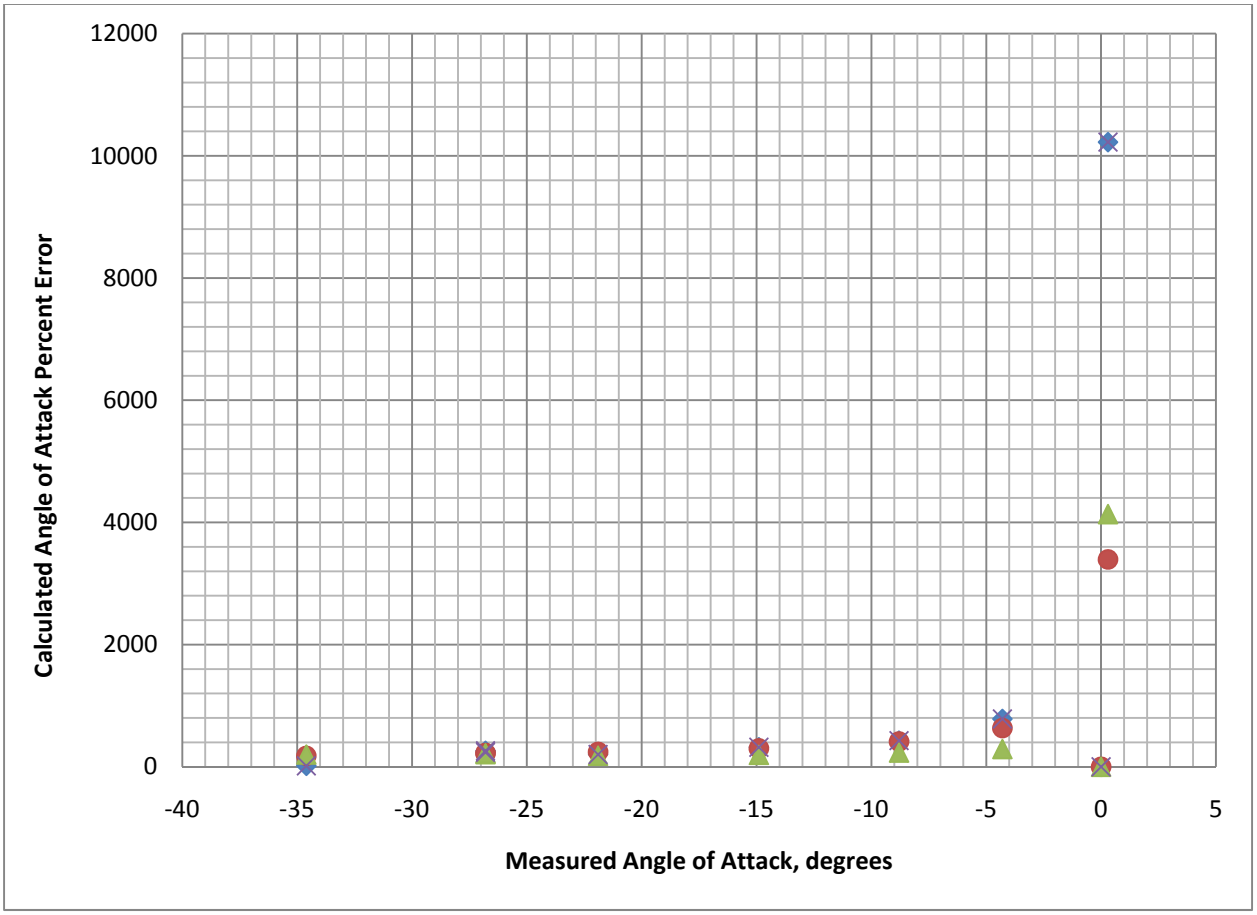

Figure B.37: Calculated angle of attack percent error vs. negative measured angle of attack values, FADS head.

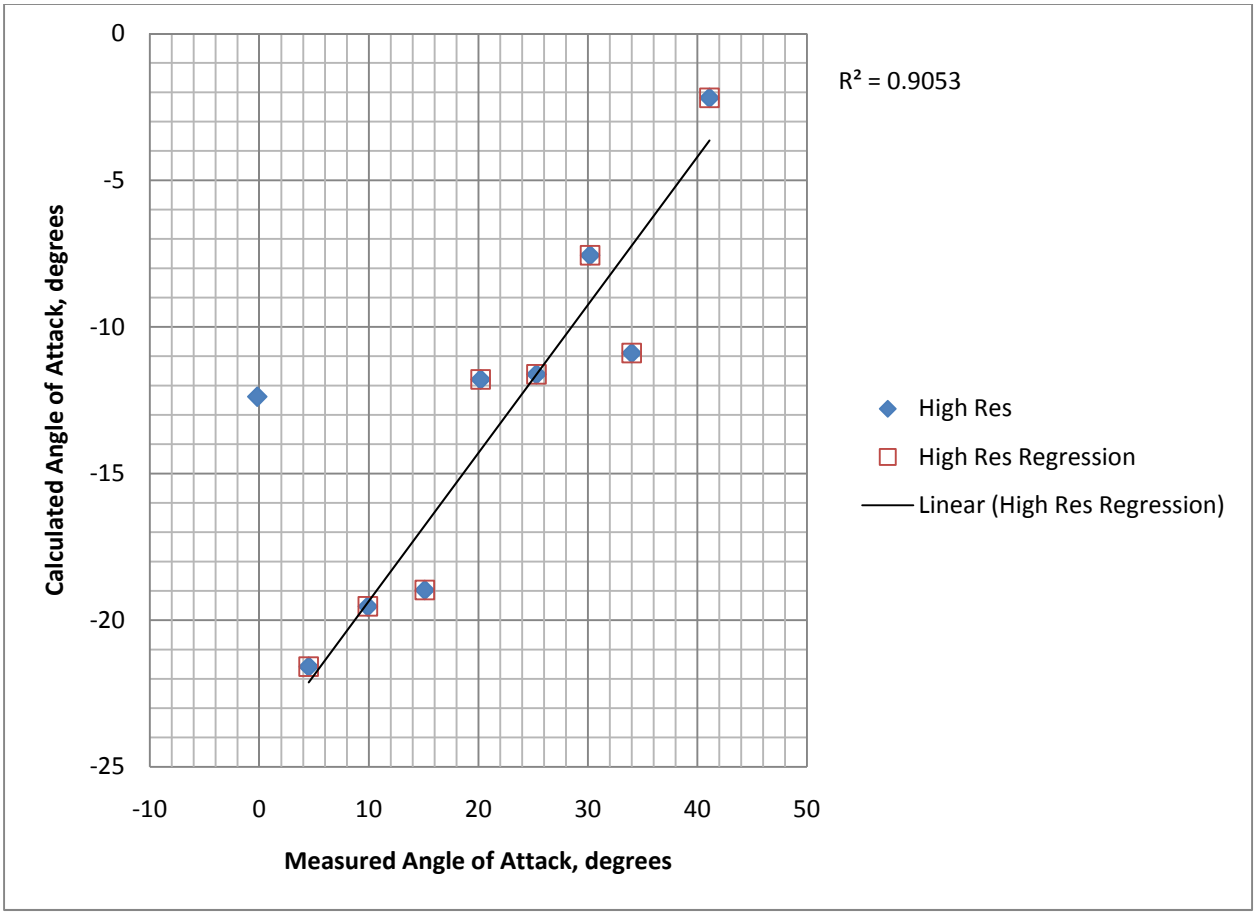

Figure B.38: Calculated angle of attack vs. positive measured angle of attack values, FADS probe head, High Resolution method.

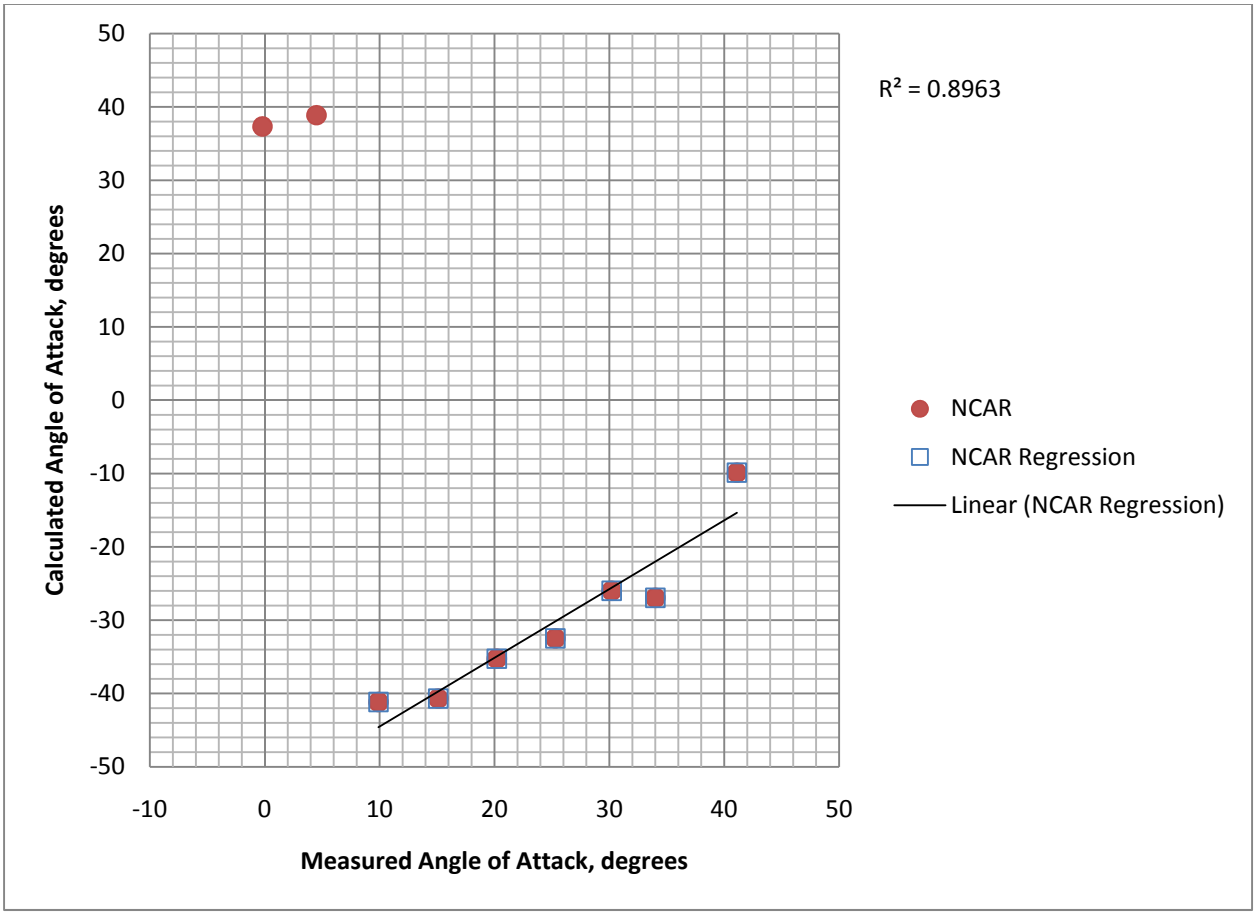

Figure B.39: Calculated angle of attack vs. positive measured angle of attack values, FADS probe head, NCAR method.

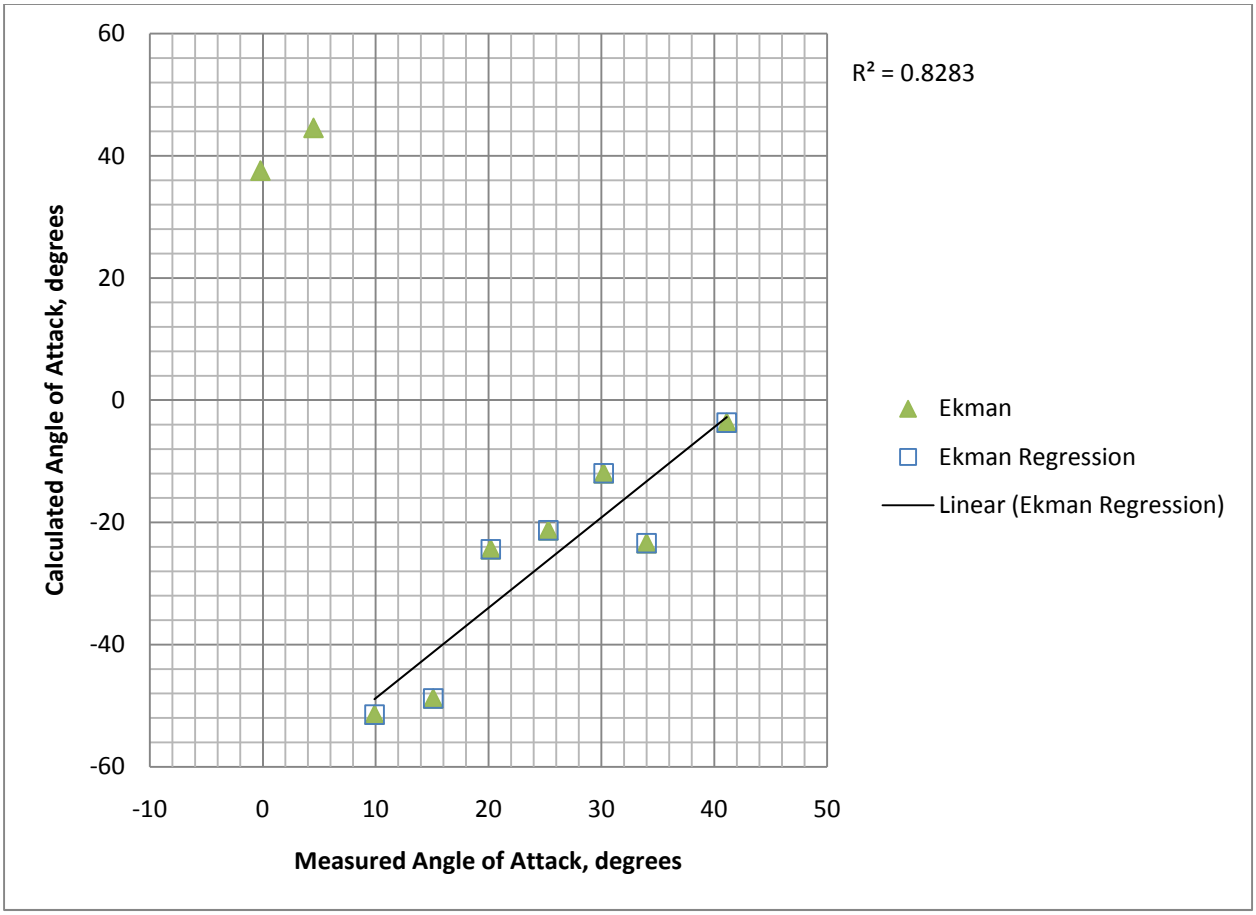

Figure B.40: Calculated angle of attack vs. positive measured angle of attack values, FADS probe head, Ekman method.

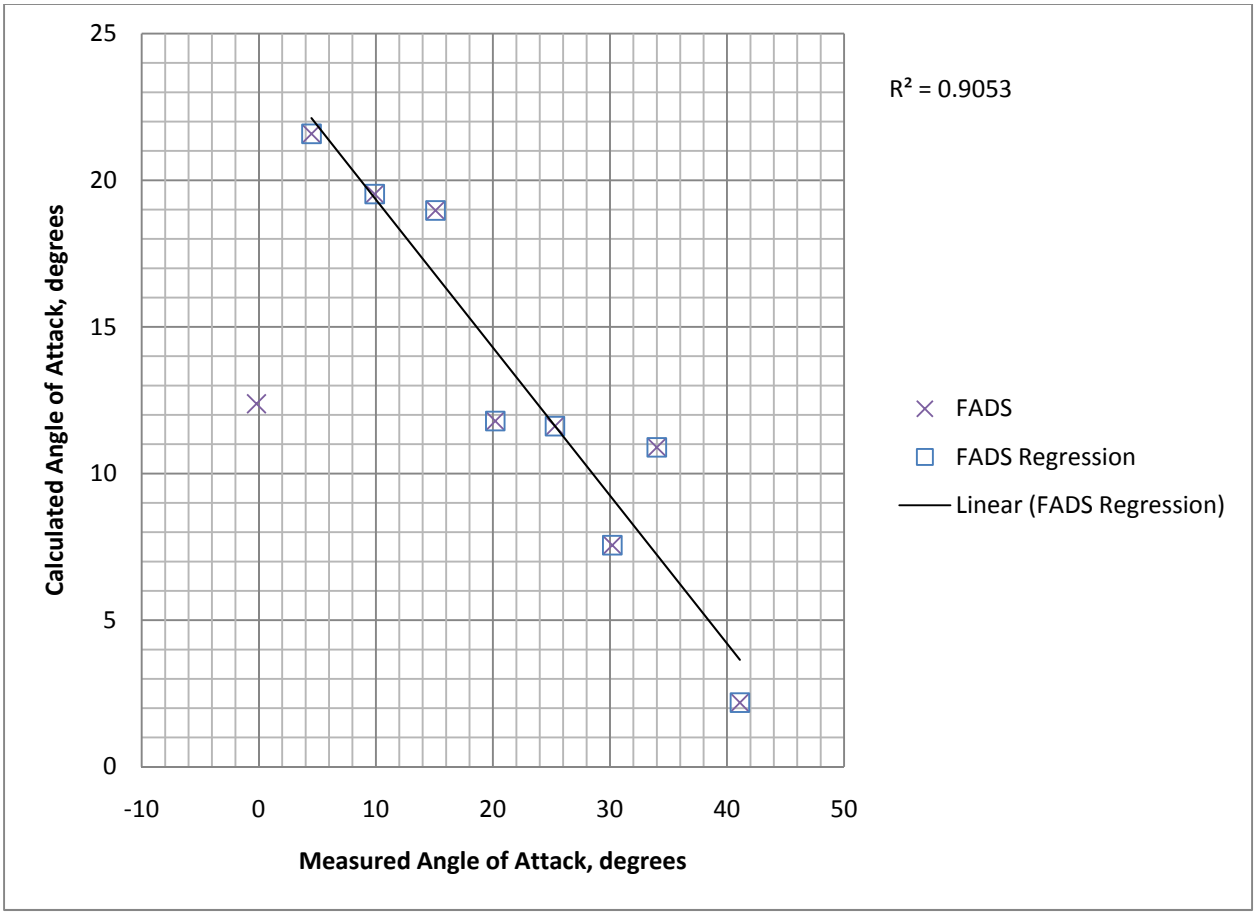

Figure B.41: Calculated angle of attack vs. positive measured angle of attack values, FADS probe head, FADS method.

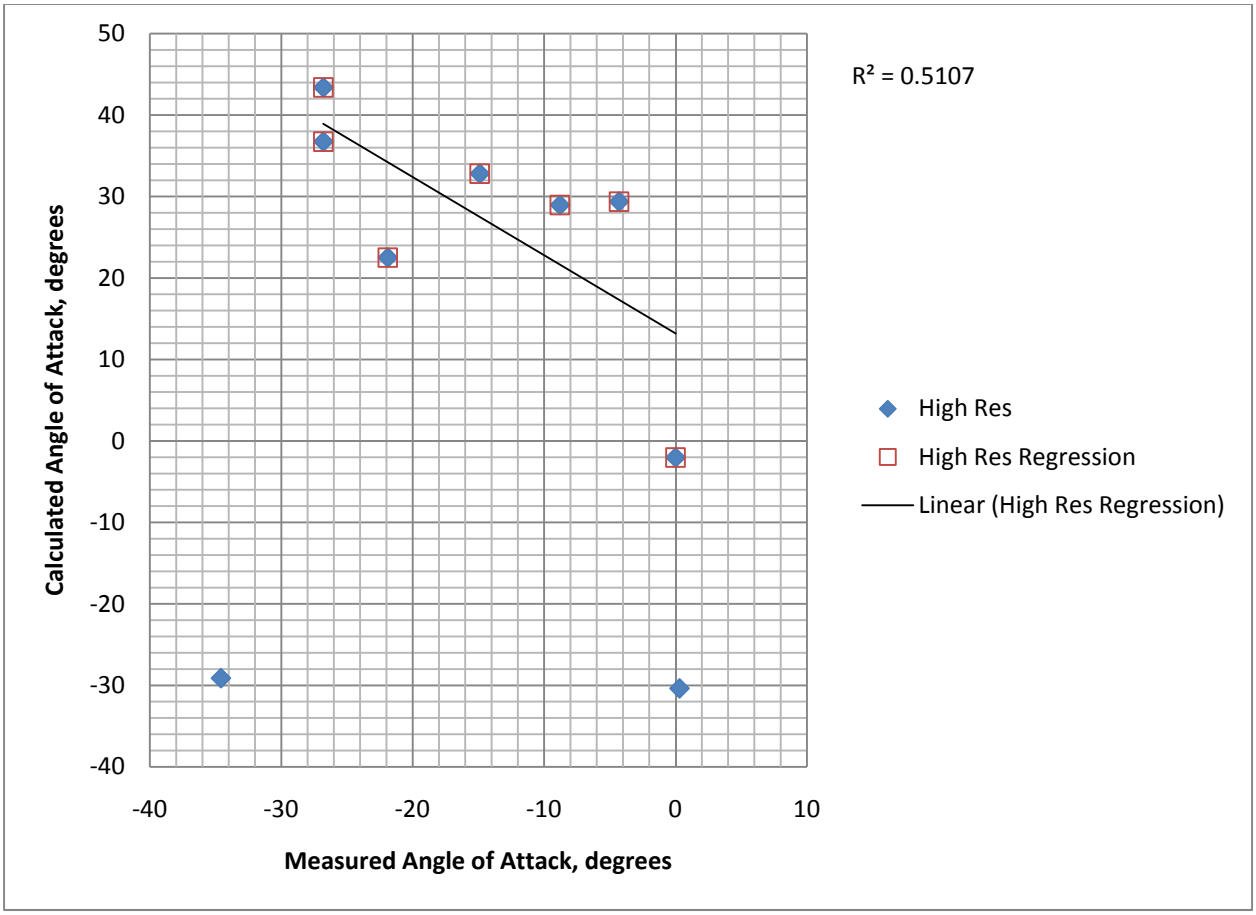

Figure B.42: Calculated angle of attack vs. negative measured angle of attack values, FADS probe head, High Resolution method.

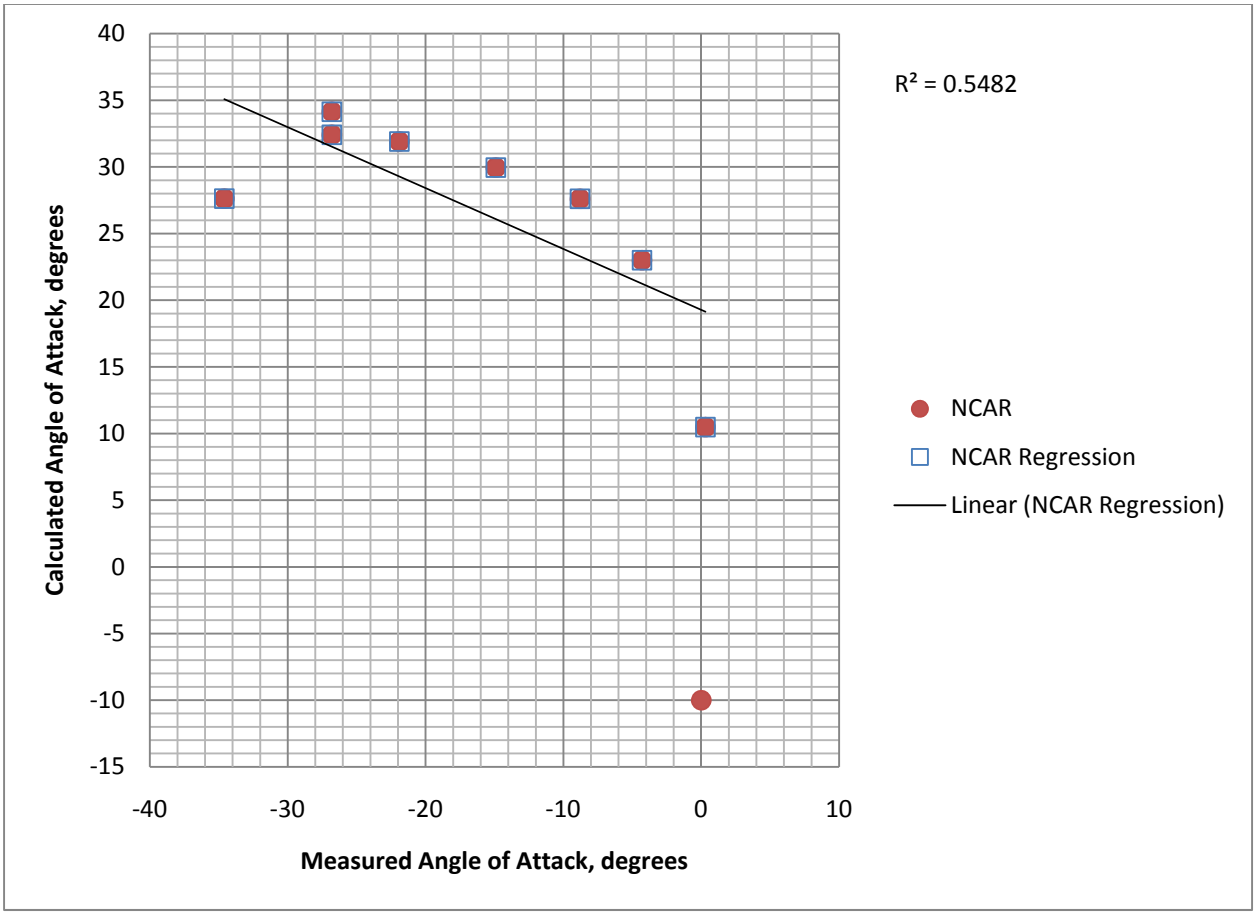

Figure B.43: Calculated angle of attack vs. negative measured angle of attack values, FADS probe head, NCAR method.

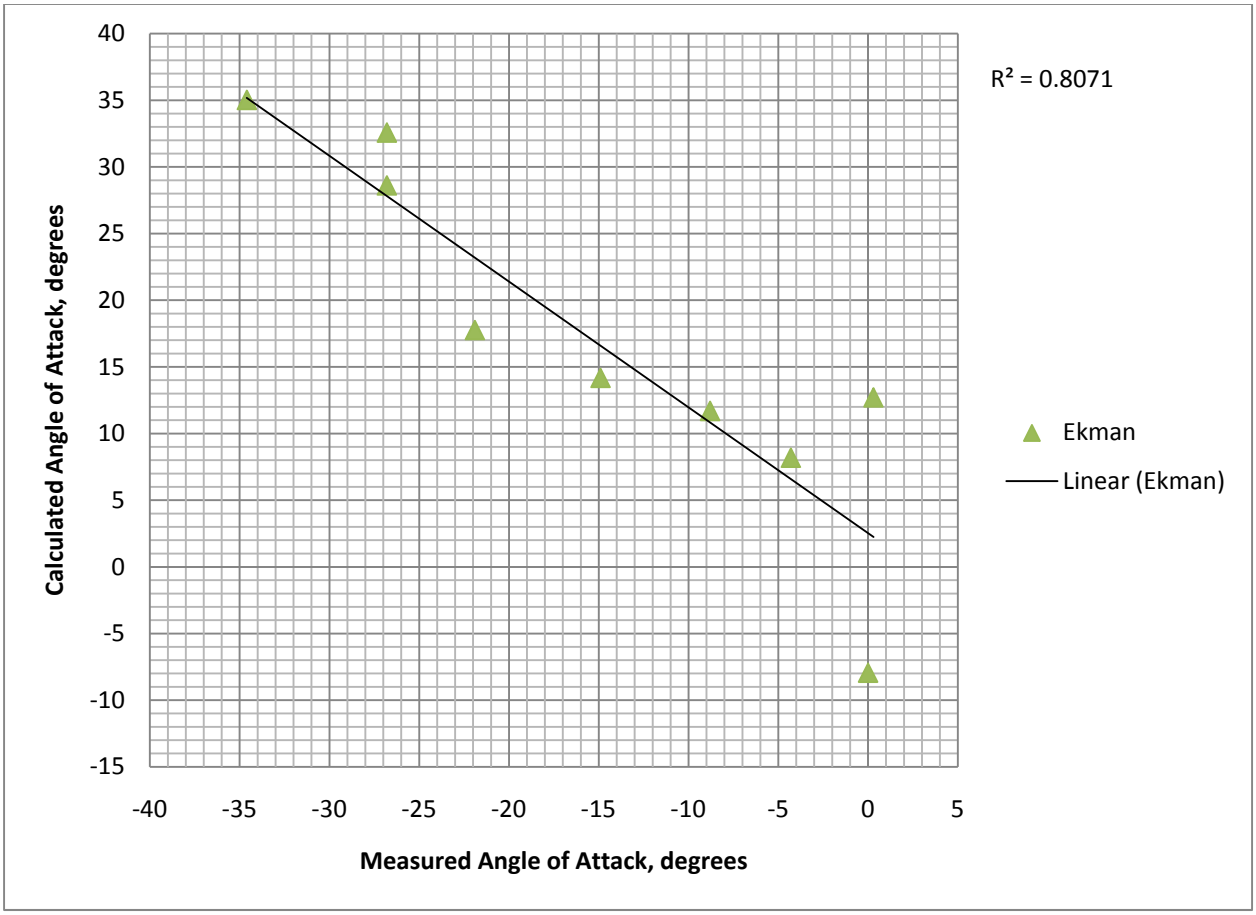

Figure B.44: Calculated angle of attack vs. negative measured angle of attack values, FADS probe head, Ekman method.

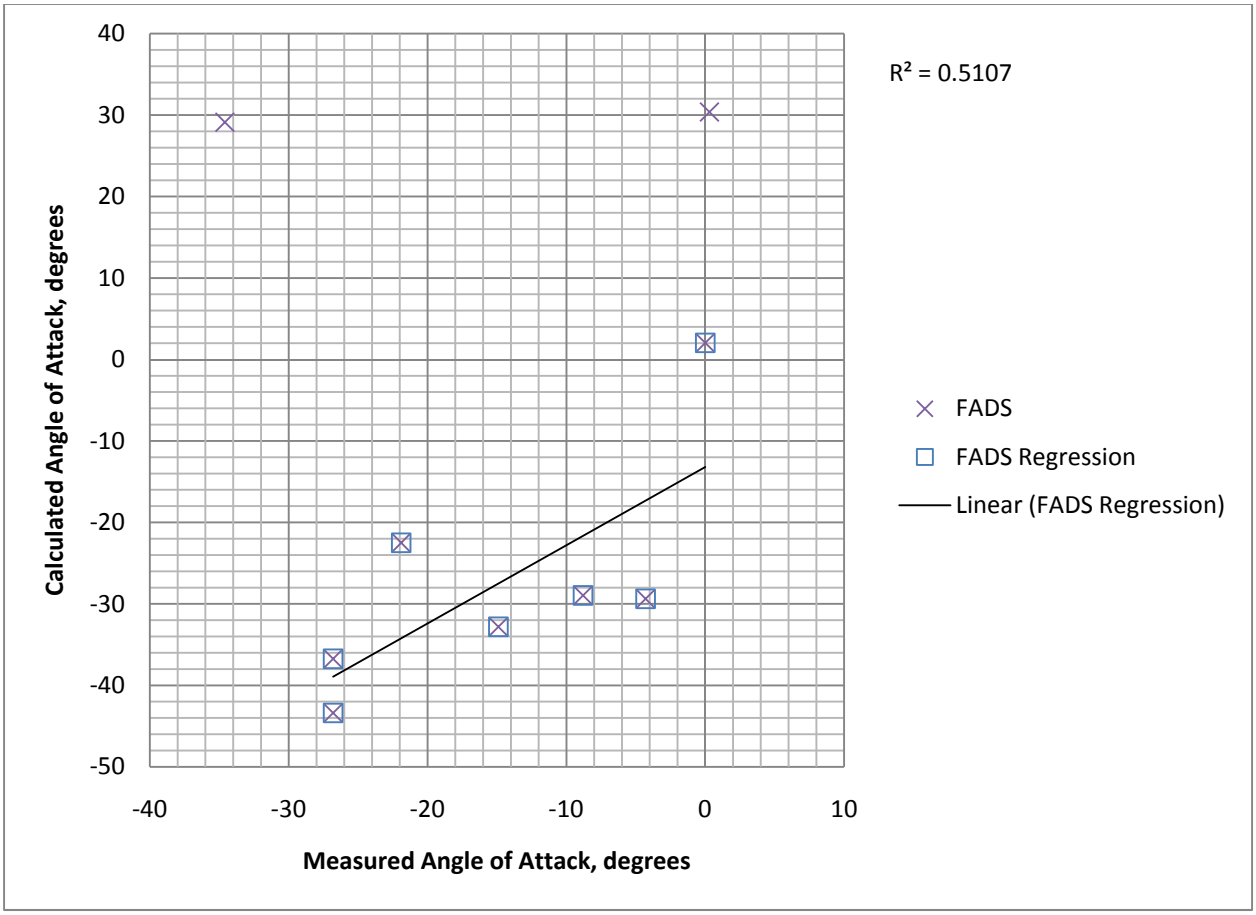

Figure B.45: Calculated angle of attack vs. negative measured angle of attack values, FADS probe head, FADS method.

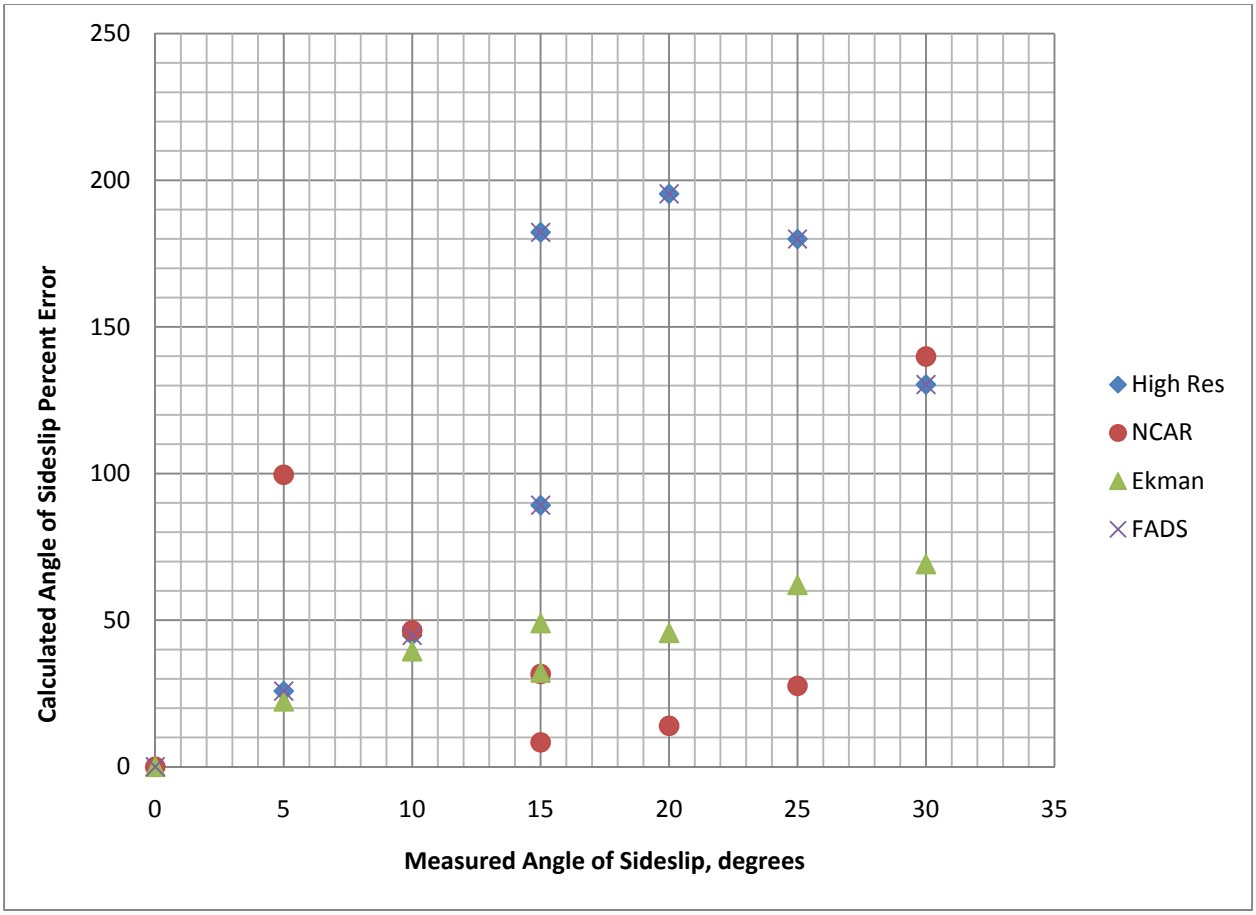

Figure B.46: Calculated angle of sideslip percent error vs. positive measured angle of sideslip values, FADS head.

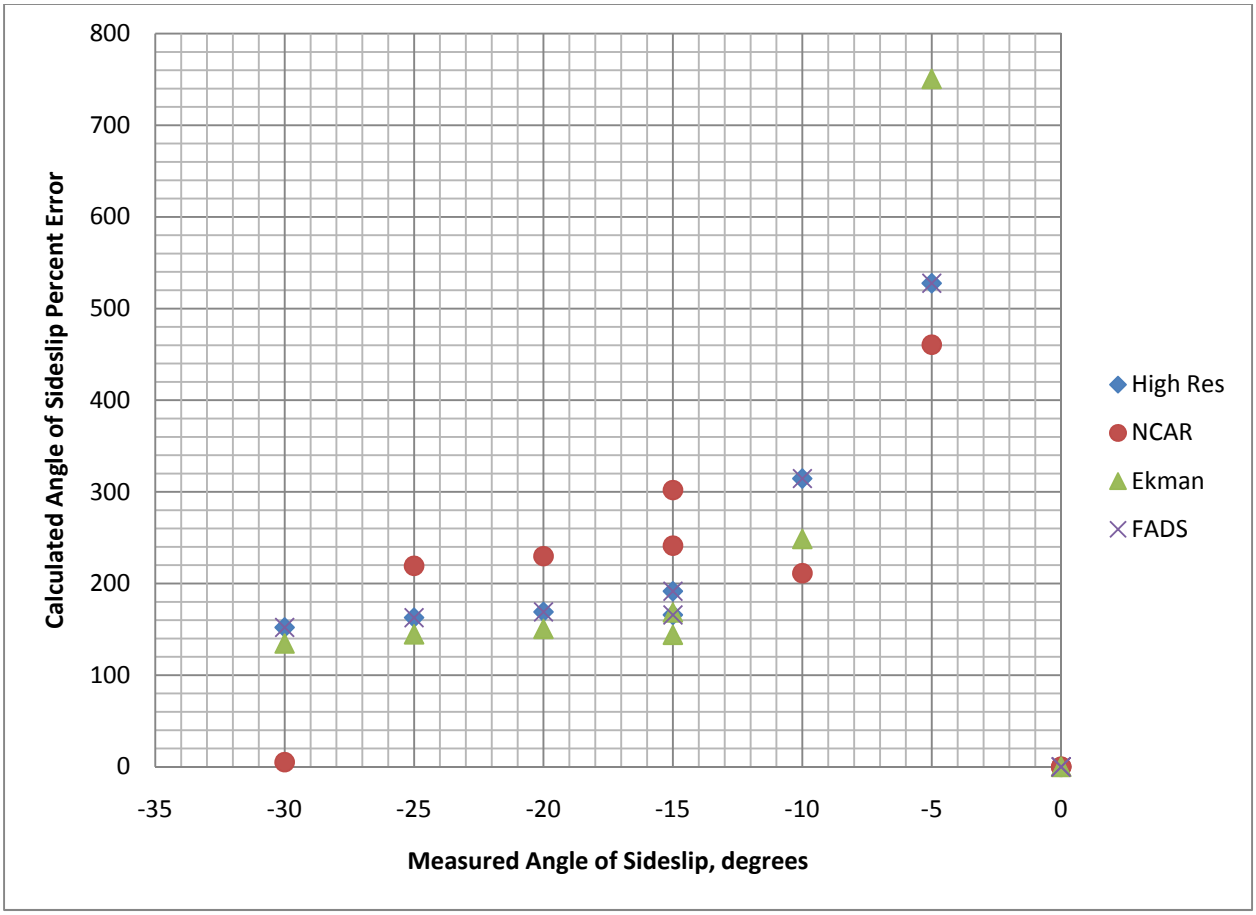

Figure B.47: Calculated angle of sideslip percent error vs. negative measured angle of sideslip values, FADS head.

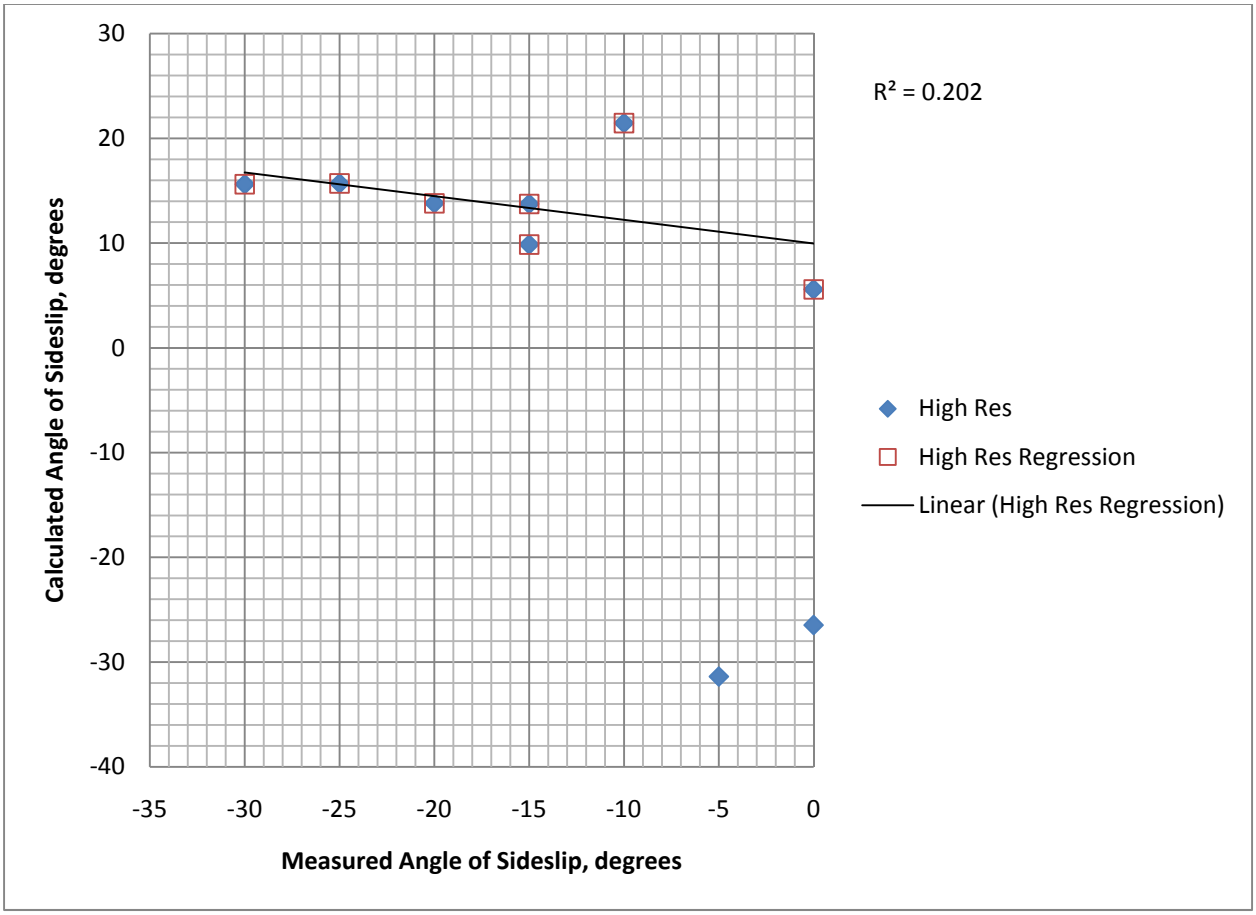

Figure B.48: Calculated angle of sideslip vs. negative measured angle of sideslip values, FADS probe head, High Resolution method.

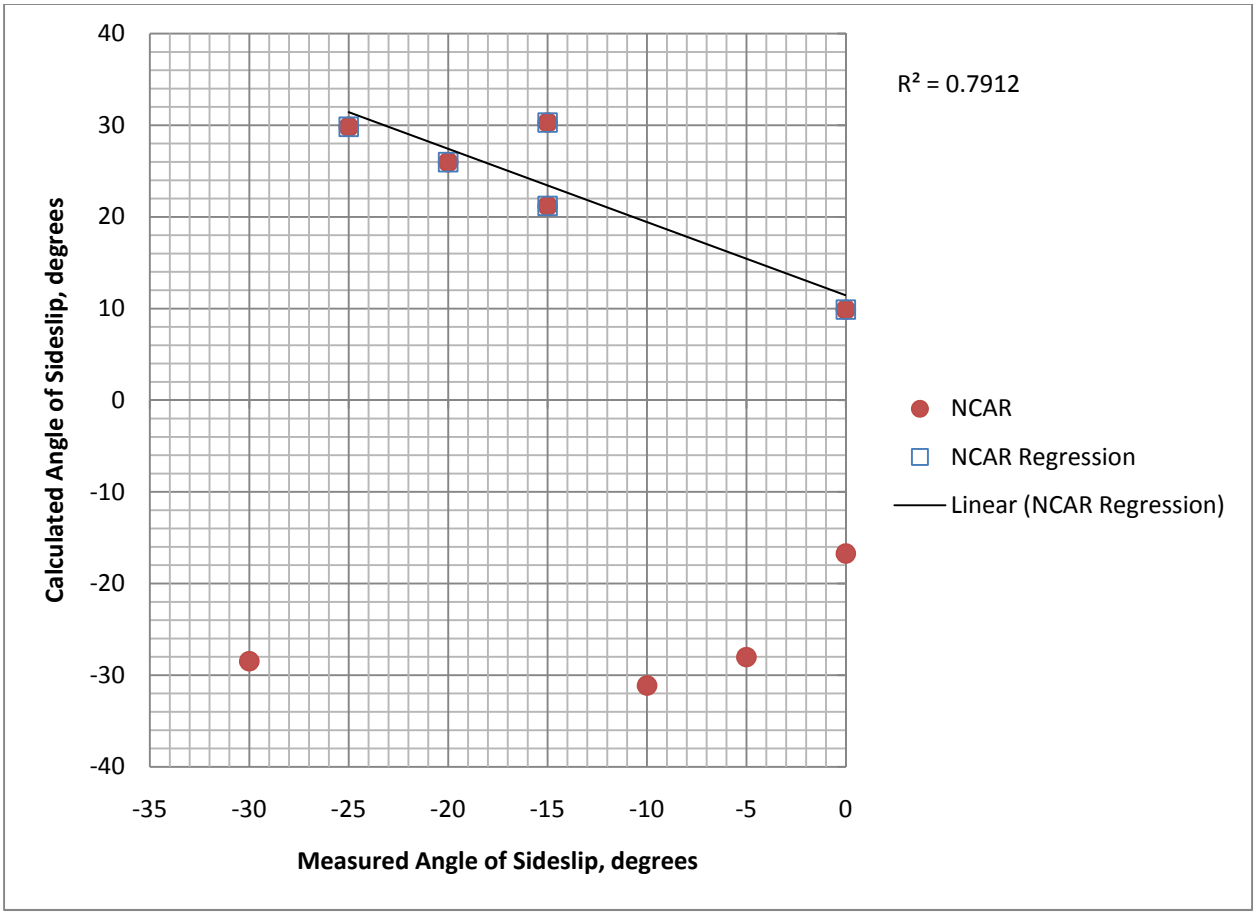

Figure B.49: Calculated angle of sideslip vs. negative measured angle of sideslip values, FADS probe head, NCAR method.

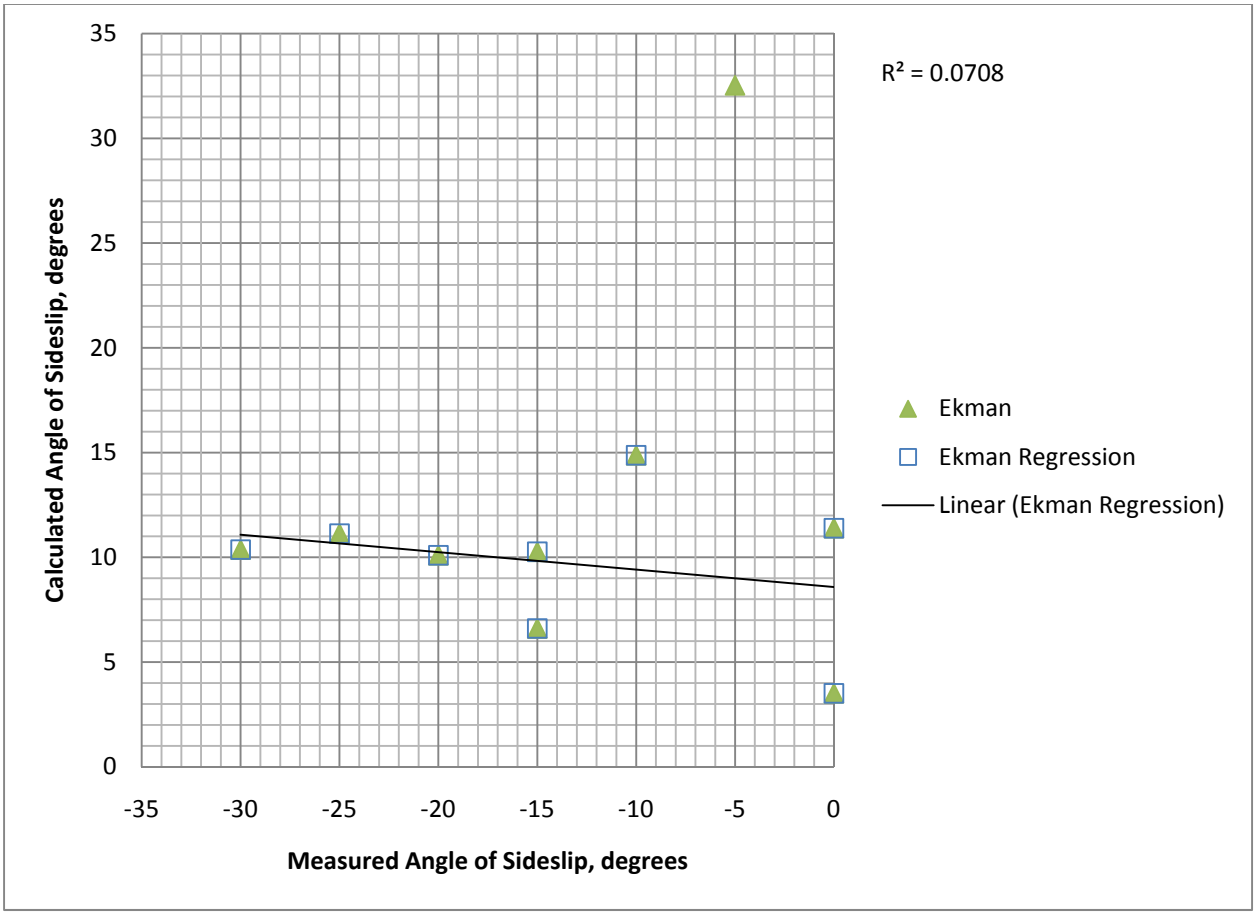

Figure B.50: Calculated angle of sideslip vs. negative measured angle of sideslip values, FADS probe head, Ekman method.

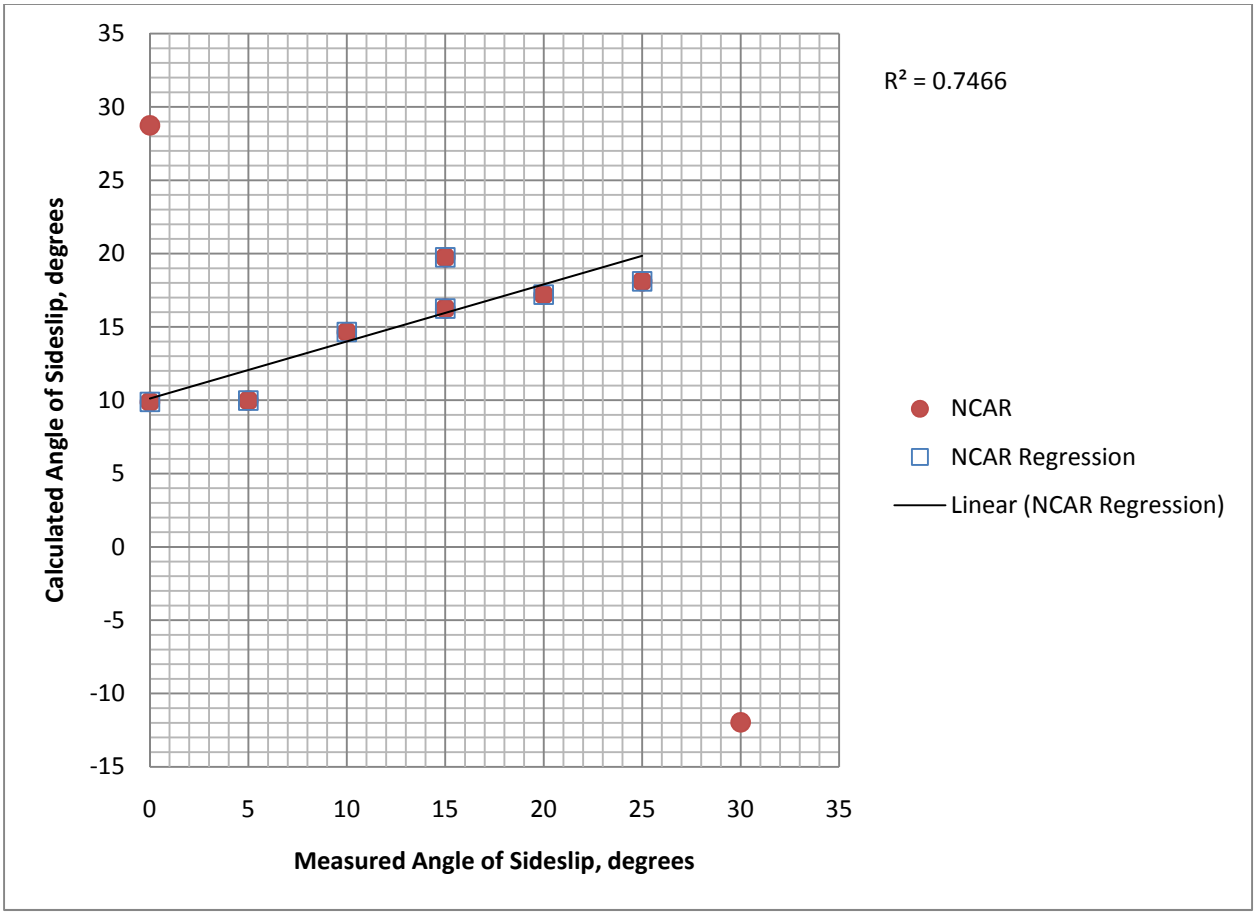

Figure B.51: Calculated angle of sideslip vs. positive measured angle of sideslip values, FADS probe head, NCAR method.

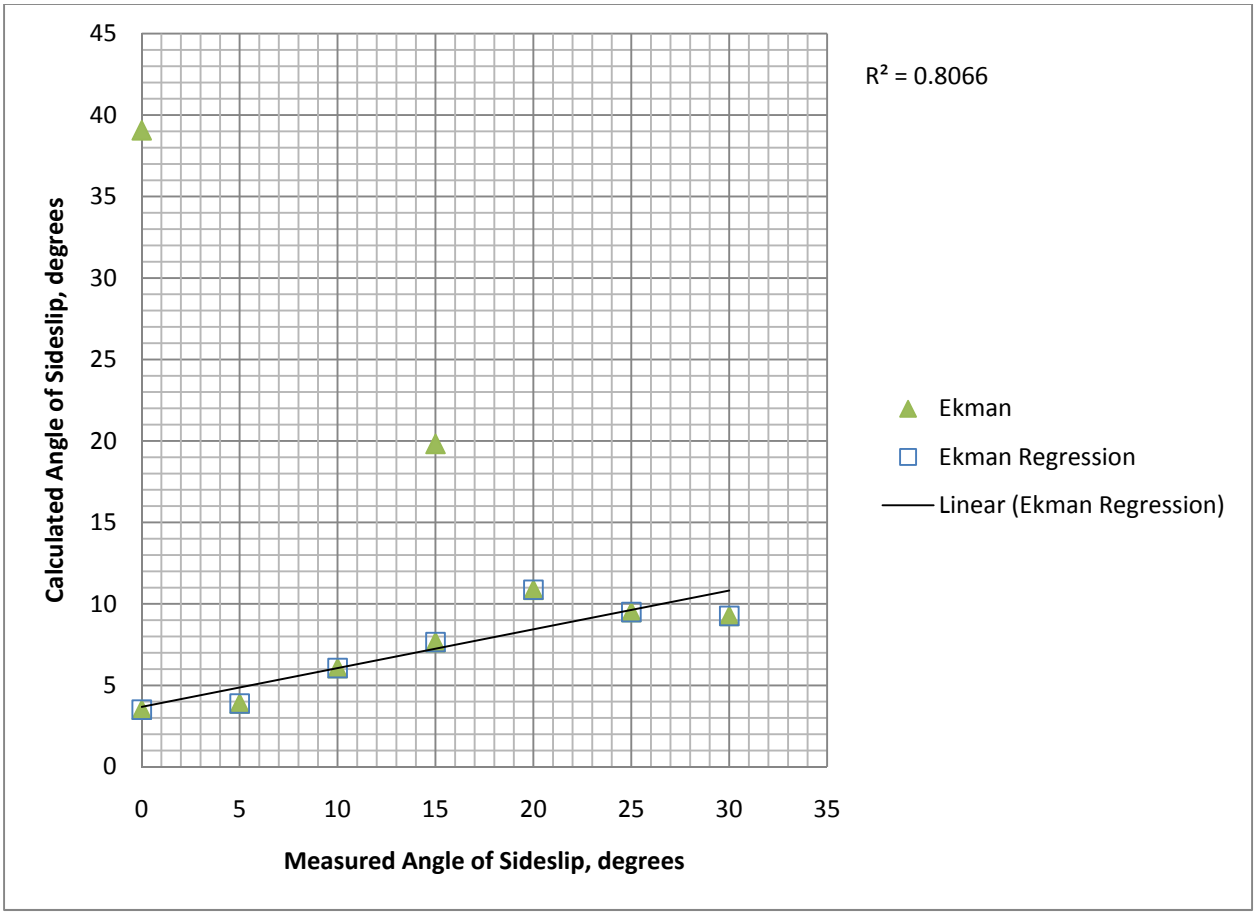

Figure B.52: Calculated angle of sideslip vs. positive measured angle of sideslip values, FADS probe head, Ekman method.

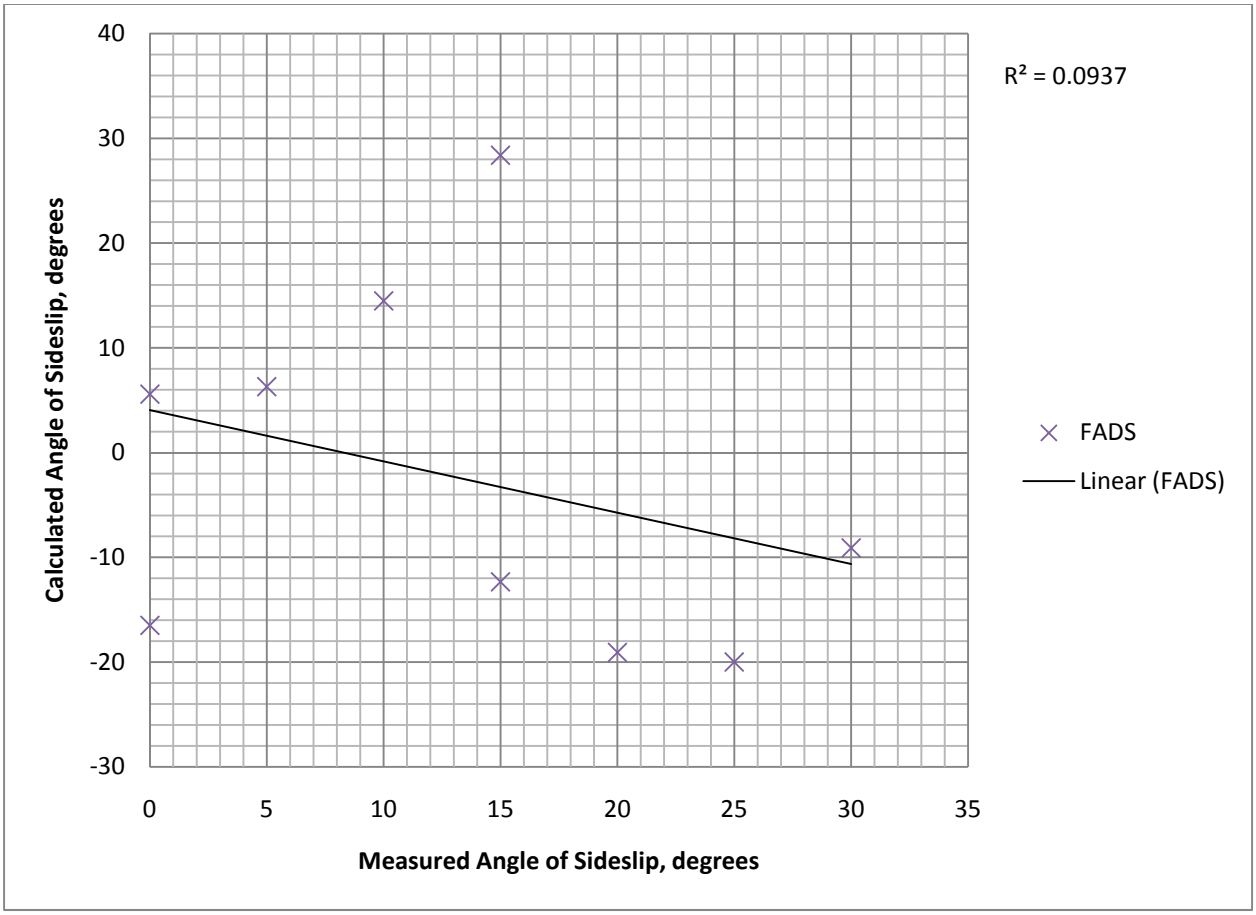

Figure B.53: Calculated angle of sideslip vs. positive measured angle of sideslip values, FADS probe head, FADS method.

VITA

Charles Lams was born in Nashville, Tennessee to parents from England. He has lived for a considerable time in both Tennessee and England and has experienced the education systems of both countries. He attended high school at Montgomery Bell Academy in Nashville and completed his 'A-Level' studies in Biology, Chemistry and Mathematics at Dulwich College in London, England. After obtaining a Bachelor of Science degree in Marine Biology and Oceanography from the University of North Wales at Bangor, also in the United Kingdom, he attended the University of Tennessee Space Institute at Tullahoma, Tennessee where he has just completed the requirements for his Master of Science degree in Aviation Systems. Charles is married with three children.